# Measuring horizontal groundwater flow with distributed temperature sensing along cables installed with direct-push equipment

des Tombe, B.F.

**DOI**
10.4233/uuid:92565bdb-cf5a-4110-abf3-1b4298720466

**Publication date**
2021

**Document Version**
Final published version

**Citation (APA)**
des Tombe, B. F. (2021). *Measuring horizontal groundwater flow with distributed temperature sensing along cables installed with direct-push equipment*. [Dissertation (TU Delft), Delft University of Technology]. https://doi.org/10.4233/uuid:92565bdb-cf5a-4110-abf3-1b4298720466

**Important note**
To cite this publication, please use the final published version (if applicable).
Please check the document version above.

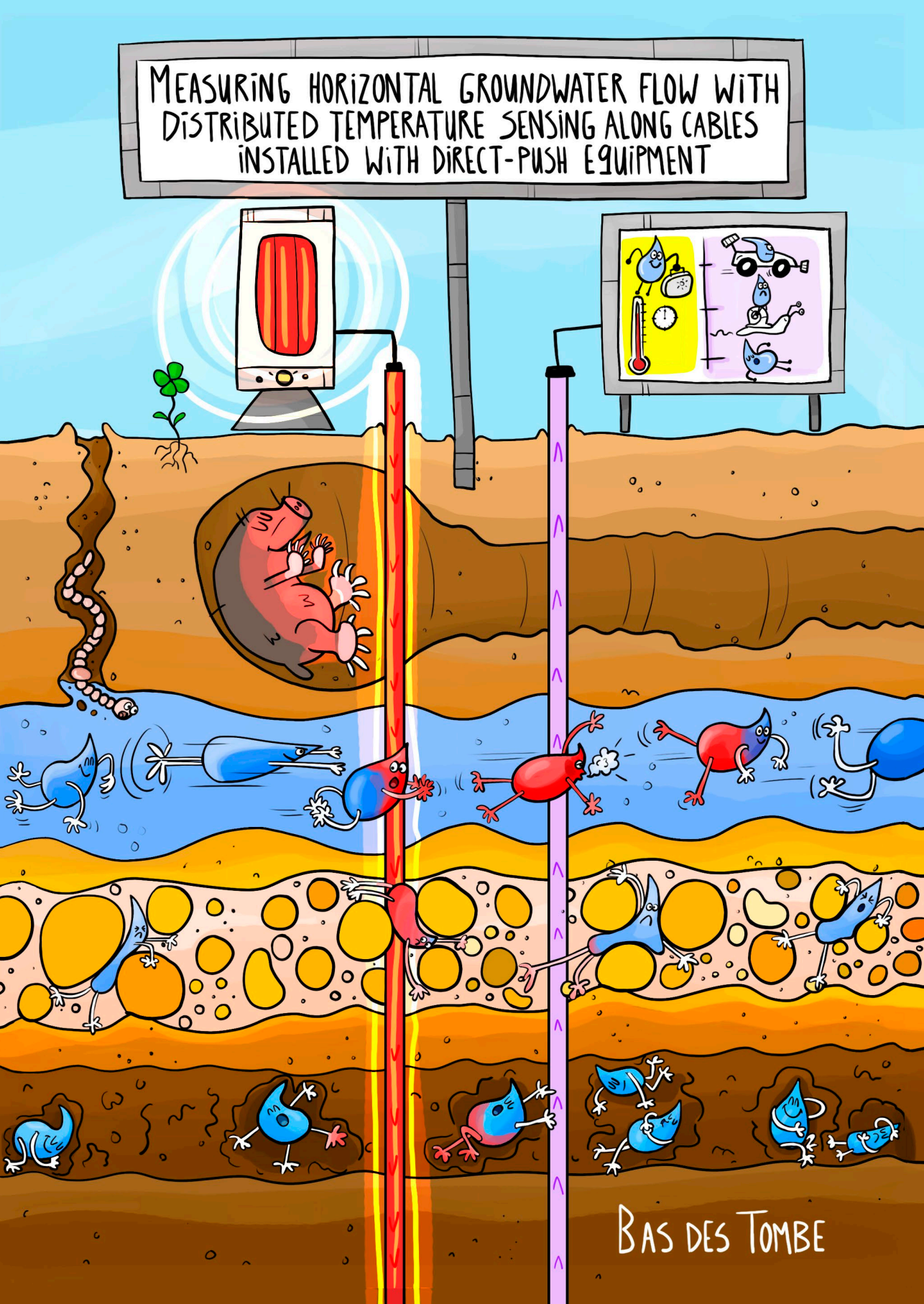
MEASURING HORIZONTAL GROUNDWATER FLOW WITH DISTRIBUTED TEMPERATURE SENSING ALONG CABLES INSTALLED WITH DIRECT-PUSH EQUIPMENT
BAS DES TOMBE

# Measuring horizontal groundwater flow with distributed temperature sensing along cables installed with direct-push equipment

## Dissertation

for the purpose of obtaining the degree of doctor
at Delft University of Technology
by the authority of the Rector Magnificus Prof. dr. ir. T.H.J.J. van der Hagen;
Chair of the Board for Doctorates
to be defended publicly on Friday, 5 march 2021 at 12:30 hours

by


## Bas François DES TOMBE

Master of Science in Civil Engineering,
Delft University of Technology, the Netherlands,
born in Amsterdam, the Netherlands.

This dissertation has been approved by the promotor

| | |
|---|---|
| Prof. dr. ir. M. Bakker | Delft University of Technology |

Composition of the doctoral committee:

| | |
|---|---|
| Rector Magnificus | Delft University of Technology, chairperson |
| Prof. dr. ir. M. Bakker | Delft University of Technology, promotor |
| | |
| *Independent members:* | |
| Dr. V.F. Bense | Wageningen University |
| Prof.dr.ir. T.J. Heimovaara | Delft University of Technology |
| Dr. T.A. Bogaard | Delft University of Technology |
| Prof.dr.ir. N.C. van de Giesen | Delft University of Technology |
| Prof.dr.ir. M.F.P. Bierkens | Utrecht University |
| Prof.dr.ir. T.N. Olsthoorn | Delft University of Technology |

This work was funded in part by the Dutch Research Council (NWO) within the program The New Delta with project number 869.15.006.

*Keywords:* Hydrology; Groundwater; flow; measurement; DTS; fiber optic; heat; tracer; residence time

*Printed by:* Proefschrift All In One

*Front & Back:* Eva van Aalst. https://www.evavanaalst.com/



ISBN 978-94-93184-81-7

An electronic version of this dissertation is available at http://repository.tudelft.nl/.

# Contents

# Summary

The pressure on groundwater systems, especially in coastal regions, increases as the population rapidly grows. In these regions, management of water tables and fluxes is important to minimize droughts, salt-water intrusion, and flooding. Proper management of such groundwater systems requires knowledge of how groundwater responds to water entering and leaving the system. Groundwater models can translate changes in inflow and outflow into changes in the groundwater table and flow. Proper calibration of these models depends on measurements of the flow and the groundwater table. While the groundwater table can be measured relatively easily, flow can only be measured either when it enters or exits groundwater systems (e.g., wells, infiltration, seepage), indirectly with tracers (solutes or heat), or with a variety of geophysical techniques. In this dissertation, a new approach is presented to measure horizontal groundwater in the aquifer with distributed temperature sensing (DTS) along cables that are inserted with direct-push equipment.

In a heat tracer test, temperature is measured to estimate groundwater flow. In this dissertation, the temperature is measured with fiber-optic cables that are inserted up to 45 m in unconsolidated aquifers using direct-push equipment, so that the cables are in direct contact with the aquifer. The temperature can be measured every 13 cm along fiber-optic cables with DTS. Two types of heat tracer tests are distinguished: passive heat tracer tests and active heat tracer tests. In passive heat tracer tests, the groundwater temperature fluctuations are induced naturally at the surface. In active heat tracer tests, a heating cable actively transfers heat to the groundwater.

Heat tracer tests benefit from accurate temperature measurements with uncertainty estimates. An approach is developed to estimate the uncertainty of temperatures estimated from DTS measurements. The uncertainty in DTS measurements is the result of the noise from the detectors and the uncertainty in the calibrated parameters that relate the backscatter intensity to temperature. The uncertainty varies along the fiber as the backscatter intensity decays and varies over time due to a fluctuating laser intensity. A new calibration procedure is

presented that reduces the uncertainty in the estimated temperature and provides a confidence interval to the estimated temperature. First, the noise in the backscatter intensity measurements is estimated. The parameter uncertainty is reduced by weighing the backscatter intensity with the inverse of the noise variance, so that large intensity measurements have a larger weight in the parameter estimation. The confidence intervals for the estimated temperatures are computed by propagating the noise and the parameter uncertainty with Monte Carlo sampling. In double-ended setups, measurements are made from both ends of the fiber resulting in large differences in uncertainty between both measurements. To improve the estimates along the entire fiber, the temperatures estimated from both ends of the fiber are averaged using the weighted average. Connectors that are used to connect fibers introduce time-variant losses. These losses are compensated for by making use of fiber sections with a matching temperature, to prevent a bias in the estimated temperature. The developed DTS calibration procedure is implemented in the "dtscalibration" Python package.

Passive heat tracer tests use the fiber-optic cables inserted in the aquifer to measure naturally occurring temperature fluctuations. This type of test works best when temperature of, e.g., infiltrating surface water varies seasonally, because variations with a shorter variation dampen out over a short distance. A passive heat tracer test was conducted at a bank filtration system, for which the travel time distribution of the soil passage is a critical design parameter. Groundwater flow from the infiltration basin to the pumping wells was simulated with a model for combined groundwater flow and heat transport. The temperature variation of the infiltrating water introduced a seasonal variation in the travel time distribution through seasonal variation of the viscosity. The travel time of the fastest 10% reduced from 49 to 42 days in the summer months, which increases the risk of pathogen contamination of the pumped water.

Active heat tracer tests rely on a heating cable to raise the temperature. The heating cable and fiber-optic cable are inserted together in the aquifer, without control of their relative position. A new method was developed to accurately estimate the specific discharge independent of the position of the fiber-optic cable relative to the heating cable, by fitting an analytical solution for two-dimensional horizontal groundwater flow and heat transport to the measured temperature response. The background temperature can be approximated as constant, or interpolated between the temperature at the start and end of the test. Two terms with thermal properties need to be estimated to compute the specific discharge from the fitted parameters. The first term represents the soil properties related to conduction, and is relatively constant for a wide variety of saturated sands. The second term represents the soil properties related to thermal dispersion and is uncertain, which limits the ability to estimate high

groundwater flows. The probability distribution of the specific discharge is estimated with a Monte-Carlo analysis. Active heat tracer tests were conducted in three case studies to test the approach.

The first case study was at the same location as the passive heat tracer test. The objective of the first case study was to test the method with measurements from fiber-optic cables inserted at different positions relative to the heating cable. Specific discharges between 0.4 and 0.6 m/day were found at the different locations, similar to estimates from previous studies. It was concluded that the specific discharge can indeed be estimated independent of the relative position of the heating and fiber-optic cables if the measured temperature increase was at least 0.5°C.

The objective of the second case study was to test whether cables that are inserted 45 m can be used to estimate the specific discharge in a thin layer at 30 m depth, where the flow was significantly higher than at other depths. The location was near the dike of a polder. The estimated specific discharges at all depths varied between 0.07 and 0.10 m/day, except for the thin layer, for which 0.20 m/day was estimated. It was shown with numerical experiments that the profile of the estimated specific discharge was smoother than in reality due to vertical conduction, but the peak specific discharge was estimated correctly for layers thicker than 1.7 m. The specific discharge was estimated accurately with a narrow confidence interval. The uncertainty in the thermal dispersivity does not affect the accuracy of the specific discharge estimate for these low flows.

The objective of the third case study was to determine whether estimation of the specific discharge can be improved by conducting two active heat tracer tests at the same location, but with different values of the specific discharge. The specific discharge was measured two times near a pumping well. The discharge of the pumping well was varied to change the specific discharge. If the ratio of the two specific discharges is known, the term representing the soil properties related to thermal dispersion can be estimated. This term could be accurately estimated at depths where the specific discharge was at least 1 m/day for one of the tests, which improved the estimates of the specific discharge at these depths significantly. The estimated value of this term varied strongly over depth, resulting in a thermal dispersivity that varied from 3.4 mm to 19 cm. This strong variation confirms the large uncertainty associated with obtaining the thermal dispersivity from literature. The measurements from the third case study were used a second time, this time pretending the ratio of the specific discharges of the two tests was not known. It was shown that estimates of this ratio are accurate because the thermal properties are the same in both tests and most of their associated uncertainty cancels. Estimates of this ratio may be used, e.g., to

monitor clogging of well filters or to estimate seasonal variation in groundwater flow.

# Samenvatting

De druk op grondwatersystemen neemt toe ten gevolgen van de snelle bevolkingsgroei, met name in de kustgebieden. Beheer van grondwaterpeilen in deze gebieden is belangrijk om droogte, zoutwaterintrusie en overstromingen te voorkomen. Goed beheer van het grondwater vereist kennis van hoe het grondwaterpeil reageert op infiltraties in en onttrekkingen uit het systeem. De effecten van infiltreren en onttrekkingen op het grondwaterpeil worden beschreven met grondwatermodellen. Kalibratie van dit soort modellen vereist zowel metingen van het grondwaterpeil als van grondwaterstroming. Hoewel het grondwaterpeil makkelijk kan worden gemeten, kan grondwaterstroming alleen worden gemeten als het grondwater het systeem ingaat of verlaat (o.a., putten, infiltratie, kwel), indirect met tracers (opgeloste stoffen of warmte), of met een variëteit aan geofysische metingen. In dit proefschrift wordt een nieuwe methode gepresenteerd om de horizontale grondwaterstroming te meten met distributed temperature sensing (DTS) langs kabels die geïnstalleerd zijn met sondeerapparatuur.

Bij een warmteproef wordt temperatuur gemeten om de grondwaterstroming te schatten. In dit proefschrift wordt de temperatuur gemeten met glasvezelkabels die met sondeerapparatuur tot 45 m diep zijn aangebracht in ongeconsolideerde watervoerende pakketten, en is het gebruik van putten voorkomen. De temperatuur kan elke 13 cm worden gemeten met DTS langs de glasvezelkabel. Twee soorten warmteproeven worden onderscheiden: passieve warmteproeven en actieve warmteproeven. In passieve warmteproeven hebben de temperatuurfluctuaties een natuurlijke oorsprong en in actieve proeven wordt het grondwater actief verwarmt met bijvoorbeeld een warmtekabel.

De grondwaterstroming kan beter geschat worden met nauwkeurige temperatuurmetingen en een schatting van hun onzekerheid. Er is een aanpak ontwikkeld om de onzekerheid in een DTS meting te schatten. De onzekerheid in een DTS meting komt voort uit ruis dat wordt geïntroduceerd door de lichtsensoren en de onzekerheden in de parameters die de intensiteit van het teruggekaatste licht relateren aan de temperatuur. De onzekerheid in de DTS meting

varieert langs de glasvezel omdat de intensiteit van het teruggekaatste licht afzwakt en varieert over tijd door een variërende laser intensiteit. Een nieuwe kalibratiemethode wordt gepresenteerd die de onzekerheid in de geschatte temperatuur vermindert en het betrouwbaarheidsinterval voor de temperatuur inschat. Hierin wordt eerst de distributie van de ruis in de metingen van het teruggekaatste licht geschat. De parameteronzekerheden worden gereduceerd door de metingen van de intensiteit van het teruggekaatste licht te wegen met de inverse van de variantie van de ruis, zodat metingen met een hogere intensiteit meer meewegen in het schatten van de parameters. Het betrouwbaarheidsinterval van de geschatte temperatuur wordt berekend met een Monte Carlo simulatie van de onzekerheid t.g.v. de ruis in de meting van de intensiteit van het teruggekaatste licht en de onzekerheid in de parameters die deze intensiteit relateren aan temperatuur. In DTS opstellingen waar van beide kanten gemeten wordt zitten verschillen in onzekerheid tussen de metingen van beide kanten. Om de metingen die gedaan worden met DTS opstellingen waar van beide kanten gemeten wordt te verbeteren, worden beide metingen gemiddeld met het gewogen gemiddelde. Stekkers die gebruikt worden om glasvezels met elkaar te verbinden, introduceren een demping van de lichtintensiteit die varieert over tijd. Deze demping kan worden gecorrigeerd door gebruik te maken van twee glasvezelsecties aan beide kanten van de stekker waarvan bekend is dat ze dezelfde temperatuur hebben. De DTS kalibratiemethode is geïmplementeerd in het “dtscalibration” Python pakket.

Passieve warmteproeven gebruiken de DTS metingen om de temperatuurfluctuaties met een natuurlijke oorsprong te meten. Dit soort proeven werken het best met seizoensfluctuaties in de temperatuur van het infiltrerende water, omdat fluctuaties met een kortere periode sneller dempen. De verblijftijd is een belangrijke ontwerpparameter in duinfiltratiesystemen. Een passieve warmteproef uitgevoerd om de distributie van de verblijftijd in een duinfiltratiesysteem te bepalen. Grondwaterstroming van het infiltratiepand tot aan de onttrekkingsputten is gesimuleerd met een model voor grondwaterstroming en warmtetransport. Naast het onttrokken debiet heeft de temperatuur van het infiltratiewater invloed op de verblijftijd. De seizoensvariatie in de temperatuur van het infiltratiewater resulteert via de viscositeit in een seizoensvariatie in de verblijftijd. De verblijftijd van de snelste 10% van het onttrokken water verminderde van 49 tot 42 dagen in de zomermaanden, waarmee het risico op pathogene besmettingen wordt vergroot.

In actieve warmteproeven wordt de temperatuur actief verhoogd met bijvoorbeeld een warmtekabel. De warmtekabel en glasvezelkabel worden te samen in het watervoerende pakket geïnstalleerd, waardoor controle over de onderlinge positie van de twee kabels ontbreekt. Een nieuwe methode is ontwik-

keld om het specifiek debiet te schatten onafhankelijk van de onderlinge positie van de twee kabels, door een analytische oplossing voor tweedimensionale horizontale grondwaterstroming en warmtetransport te fitten door de DTS metingen. De achtergrondtemperatuur kan als constant worden beschouwd, of lineair worden geïnterpoleerd tussen de temperatuur aan het begin en eind van de proef. Twee groepen met thermische eigenschappen moeten worden geschat om het specifiek debiet te schatten uit de gefitte parameters. De eerste groep heeft betrekking tot thermische conductie, en is relatief constant voor verschillende soorten zand. De tweede groep heeft betrekking tot de thermische dispersie en introduceert een grote onzekerheid in de schatting van het specifiek debiet voor hoge snelheden. De betrouwbaarheidsintervallen voor het geschatte specifiek debiet worden geschat met een Monte Carlo simulatie. Actieve warmteproeven zijn uitgevoerd in drie testopstellingen.

De eerste testopstelling maakte gebruik van dezelfde opstelling als waarmee de passieve warmteproef is uitgevoerd. De doelstelling van de eerste testopstelling was om het specifiek debiet te schatten met glasvezelkabels die op verschillende posities t.o.v. de warmtekabel zijn geïnstalleerd. Het specifiek debiet werd voor de verschillende glasvezelkabels geschat tussen de 0.4 en 0.6 m/dag, gelijk aan de bevindingen uit voorgaande studies. Er kan geconcludeerd worden dat het specifiek debiet inderdaad geschat kan worden onafhankelijk van de positie van de glasvezelkabel t.o.v. de warmtekabel mits de temperatuurstijging minimaal 0.5°C was.

De doelstelling van de tweede testopstelling was om de over een diepte van 45 m kabels te installeren en om het specifiek debiet in een dunne laag op 30 m diepte te meten, waar de stroming significant groter was dan op andere diepten. De opstelling bevond zich naast de dijk van een polder. Het geschatte specifiek debiet werd voor alle diepten geschat tussen de 0.07 and 0.10 m/dag, behalve voor de dunne laag, waar 0.20 m/dag werd geschat. Het is met numerieke simulaties aangetoond dat het profiel van het geschatte specifiek debiet gladder is dan in werkelijkheid door verticale conductie. In lagen dikker dan 1.7 m wordt de piek van het specifiek debiet goed geschat. De schattingen van het specifiek debiet waren accuraat. De onzekerheid t.g.v. de thermische dispersie had geen invloed op de nauwkeurigheid van de schatting van het specifiek debiet omdat de snelheden betrekkelijk laag waren.

De doelstelling van de derde testopstelling was het verbeteren van de schatting van het specifiek debiet door twee actieve warmteproeven uit te voeren op dezelfde locatie met verschillende specifieke debieten. Het specifiek debiet is dicht bij een put twee keer gemeten. Het debiet waarmee de put onttrok verschilde tussen beide metingen waardoor het specifiek debiet verschilde. Mits de

ratio tussen de twee pompdebieten bekend is, kunnen de dispersie-gerelateerde parameters worden geschat. De waarde van deze parameters kan worden geschat mits het specifiek debiet op zijn minst 1 m/dag was bij een van de twee actieve warmteproeven. De geschatte waarde voor de dispersie gerelateerde parameters varieerde sterk over diepte, wat leide tot een thermische dispersiviteit tussen de 3.4 mm en 19 cm. Deze sterke variatie bevestigd de grote onzekerheid die vooraf werd aangenomen voor de waarde van de thermische dispersiviteit. De metingen van de derde proefopstelling zijn nog een keer gebruikt, dit keer werd er gedaan alsof de ratio tussen de twee pompdebieten onbekend was. Er wordt aangetoond dat deze ratio nauwkeurig geschat kan worden omdat de thermische parameters weliswaar onbekend zijn, maar wel gelijk zijn voor beide proeven, waardoor de onzekerheden van de thermische parameters tegen elkaar wegvallen. De ratio kan bijvoorbeeld gebruikt worden om putverstoppingen te monitoren of om de seizoensvariatie in de stroomsnelheid te meten.

# 1 Introduction

## 1.1 Topic and context

The pressure on fragile groundwater systems in coastal regions increases as the population rapidly grows. In these regions, closure of the water budget is important to develop management scenarios for the reduction of droughts and saltwater intrusion. Groundwater is an important source of fresh water. The travel time of groundwater through an aquifer is of great importance for water quality. Challenges related to water quantity and quality benefit from groundwater flow measurements, but these are difficult to obtain and are usually inferred from groundwater models. Calibration of such models requires measurements of both head and flow. While head can be measured directly, flow can only be measured either when it enters or exits the aquifer (e.g., wells, infiltration, seepage), with tracers (solutes or heat), or with a variety of geophysical techniques. In this dissertation, a new approach is presented to measure groundwater flow that propagates horizontally through the aquifer with heat as a tracer using distributed temperature sensing (DTS) along cables that are inserted with direct-push equipment.

Temperatures can be measured with distributed temperature sensing (DTS) along optical fibers that may extend to several kilometers with a sub-meter resolution (e.g., Selker et al., 2006; Tyler et al., 2009). DTS systems function by shooting laser pulses through a fiber and measuring its backscatter. The temperature along the fiber can be estimated using calibration to fiber sections with a known temperature. Detailed calibration procedures are readily available (e.g., Hausner et al., 2011; Giesen et al., 2012; Krause and Blume, 2013; Hilgersom et al., 2016), but these procedures do not account for the spatial and temporal variation in signal intensity. The specification sheets of DTS measurement systems list the uncertainty in the temperature estimated under ideal conditions.

In practice, the uncertainty in the temperature estimate varies along the fiber, is different for each setup, and is temperature-dependent.

Optical fibers have previously been installed in wells to characterize the subsurface (e.g., Anderson, 2005; Saar, 2011; Read et al., 2013; Bense et al., 2016). But wells complicate heat tracer tests because their thermal properties are different from these of the soil (e.g., Selker and Selker, 2018), vertical mixing in the well and filter pack limits the vertical measurement resolution (e.g., Pehme et al., 2007a; Pehme et al., 2010; Coleman et al., 2015), and the position of the fiber in the well is uncertain (e.g., Moscoso Lembcke et al., 2015).

Bakker et al. (2015) developed a method to insert optical fibers and a heating cable vertically in an unconsolidated aquifer with direct push equipment. This installation method does not require wells, so that the cables are in direct contact with the aquifer and the disturbance of the aquifer is minimal. Bakker et al. (2015) performed two active heat tracer tests. The analyses of both tests were complicated by unknown positions of the fiber-optic cables relative to the heating cable. In the first test, the magnitude of the specific discharge was determined where a heating cable and a fiber-optic cable were installed together. The cables twisted around each other during installation, hence the position of the fiber-optic cable relative to the heating cable was unknown, which significantly affected the measured temperature increase during heating. In the second test, the magnitude and the direction of the specific discharge were estimated from 5 additional fiber-optic cables that were installed around the heating cable at distances of 1–2 m. The exact positions of the fiber-optic cables relative to the heating cable were known at the surface, but unknown at depth as installation of the cables with direct push gives small deviations from the vertical that were not measured.

At high groundwater flows, thermal dispersion greatly increases the uncertainty in the specific discharge estimated from active heat tracer tests (Rau et al., 2012). Similar to solute dispersivity, the thermal dispersivity is scale dependent (Marsily, 1986). Reported values range from 0.002 m for a heat pulse probe experiment (Hopmans et al., 2002), to 0.1 m for a push-pull pumping test (Vandenbohede et al., 2009), to 1 m for a closed geothermal system (Molina-Giraldo et al., 2011a). In addition to scale-dependency, the specific discharge is underestimated when heat transport through thermal dispersion is falsely attributed to conduction (Rau et al., 2012).

Opposed to actively heating the groundwater, temperature fluctuations may be naturally induced and traced with temperature measurements to estimate groundwater flow in passive heat tracer tests (e.g., Anderson, 2005; Hoehn and Cirpka, 2006; Constantz, 2008; Saar, 2011). In shallow aquifers, dikes, and

bank filtration systems, seasonal temperature fluctuation of the infiltrating water can be traced to support (regional) groundwater models (e.g., Molina-Giraldo et al., 2011b). Temperature measurements can be used in passive tracer tests as groundwater model constraints, but they require additional model boundary conditions and knowledge of the thermal parameters of the aquifer. Closure of the heat budget is needed in addition to closure of the water budget. Furthermore, the temperature may vary significantly in shallow aquifers such that the viscosity cannot be approximated as constant.

## 1.2 Objectives

The installation of optical fibers and heating cables with direct push introduces new possibilities to measure temperature in unconsolidated aquifers and to perform heat tracer tests. In this dissertation, methods are developed to measure groundwater flow in the first tens of meters of an aquifer with DTS. The objective of this dissertation is fourfold. Each objective is the topic of a separate chapter in this dissertation.

The objective in Chapter 2 is to estimate the spatial and temporal variability in the temperature and its associated uncertainty from DTS measurements.

The objective in Chapter 3 is to estimate the travel time in bank filtration systems with a passive heat tracer test that combines DTS measurements with numerical modeling of coupled groundwater flow and heat transport.

The objective in Chapter 4 is to develop an approach to estimate the magnitude of the groundwater flow with an active heat tracer test using a setup like that of Bakker et al. (2015) but which does not require knowledge of the relative positions of the cables.

The objective in Chapter 5 is to improve the estimation of the groundwater flow from two active heat tracer tests performed at the same location but under different flow conditions.

## 1.3 Outline

In Chapter 2, a calibration procedure is presented to estimate the spatial and temporal variability in the temperature and associated uncertainty from DTS measurements. The calibration procedure uses backscatter intensity measurements at Stokes (-Raman) and anti-Stokes (-Raman) wavelengths of commercially-available DTS systems. In Chapter 3, the seasonal variations in travel time in a bank filtration system is estimated using a passive heat tracer test with DTS

measurements and numerical modeling of coupled groundwater flow and heat transport. A new approach is presented in Chapter 4 to estimate groundwater flow from an active heat tracer test without knowledge of the position of the fiber-optic cable relative to the heating cable. The approach is tested in two case studies. In Chapter 5, two strategies are presented that combine two active heat trace tests performed at the same location to improve the estimation of groundwater flow. Furthermore, modifications to the DTS calibration procedure a presented that reduce the negative effects of connectors on the temperature estimation. The dissertation is concluded with a synthesis of the results of Chapters 2 to 5 and a discussion of further research perspectives.

# 2 Estimation of Temperature and Associated Uncertainty from Fiber-Optic Raman-Spectrum Distributed Temperature Sensing



**This chapter is based on:** des Tombe, Bas; Schilperoort, Bart; Bakker, Mark. (2020). Estimation of Temperature and Associated Uncertainty from Fiber-Optic Raman-Spectrum Distributed Temperature Sensing. Sensors, 20(8): 2235. https://doi.org/10.3390/s20082235. Erratum: Figure 6 of the published article contained an error which is corrected in Figure 2.6 of this dissertation.

**Abstract.** Distributed temperature sensing (DTS) systems can be used to estimate the temperature along optic fibers of several kilometers at a sub-meter interval. DTS systems function by shooting laser pulses through a fiber and measuring its backscatter intensity at two distinct wavelengths in the Raman spectrum. The scattering-loss coefficients for these wavelengths are temperature-dependent, so that the temperature along the fiber can be estimated using calibration to fiber sections with a known temperature. A new calibration approach is developed that allows for an estimate of the uncertainty of the estimated temperature, which varies along the fiber and with time. The uncertainty is a result of the noise from the detectors and the uncertainty in the calibrated parameters that relate the backscatter intensity to temperature. Estimation of the confidence interval of the temperature requires an estimate of the distribution of the noise from the detectors and an estimate of the multi-variate distribution of the parameters. Both distributions are propagated with Monte Carlo sampling to approximate the probability density function of the estimated temperature, which is different at each point along the fiber and varies over time. Various summarizing statistics are computed from the approximate probability density function, such as the confidence intervals and the standard uncertainty (the estimated standard deviation) of the estimated temperature. An example is presented to demonstrate the approach and to assess the reasonableness of the estimated confidence intervals. The approach is implemented in the open-source

Python package “dtscalibration”.

**Key points:** distributed temperature sensing; DTS; fiber optic; Raman; Stokes; temperature; calibration; uncertainty; confidence intervals.



**Publication history**

| | |
|---|---|
| Received | 20 February, 2020 |
| Revised | 9 April, 2020 |
| Accepted | 13 April, 2020 |
| Published | 15 April, 2020 |


## 2.1 Introduction

Temperatures can be measured with distributed temperature sensing (DTS) along optical fibers that may extend to several kilometers with a sub-meter resolution (e.g., Selker et al., 2006; Tyler et al., 2009). The application of DTS is of great value to characterize thermal dynamics at a scale that corresponds to, for example, many geophysical processes. Heat tracer tests with DTS have been used to estimate wind speed (e.g., Sayde et al., 2015; Ramshorst et al., 2019), evaporation (e.g., Euser et al., 2014; Schilperoort et al., 2018), soil moisture (e.g., Steele-Dunne et al., 2010), groundwater-surface water interaction (e.g., Selker et al., 2006; Lowry et al., 2007), and groundwater flow (e.g., Bakker et al., 2015; Bense et al., 2016). The specification sheets of DTS measurement systems list the uncertainty in the temperature estimated under ideal conditions. In practice, the uncertainty in the temperature estimate varies along the fiber, is different for each setup, and is temperature-dependent. Therefore, the uncertainty in the temperature estimate should be estimated separately for every DTS measurement.

DTS systems that estimate temperature from Raman-backscatter measurements shoot a laser pulse through a fiber-optic cable, which is scattered back to the DTS system by inhomogeneities in the fiber. Most of the backscattered laser has the same wavelength as the emitted laser (Rayleigh scattering), but a small fraction has different wavelengths (Raman scattering). The detectors in DTS systems measure the intensity of the backscatter at two distinct wavelengths: Stokes (-Raman) and anti-Stokes (-Raman) scatter. The temperature at the point of reflection is estimated from these two types of scatter. Stokes scatter has a longer wavelength than the laser and its intensity does not vary much with temperature, while anti-Stokes scatter has a shorter wavelength than the laser and its intensity varies significantly with temperature. The location of the measurement along the fiber is estimated from the time between sending the laser pulse and receiving the scatter. Temperature along the fiber is estimated from the

measured intensities of the Stokes and anti-Stokes scatter by calibrating to reference sections with a known temperature. In practice, these fiber sections are submerged in water baths of which the temperature is continuously measured with a separate temperature sensor. The water can be mixed with small pumps in an attempt to equalize the temperature of the water in the baths. Sequential temperature measurements require continuous calibration due to varying gains and losses in the DTS system. Detailed calibration procedures are available in the literature (e.g., Hausner et al., 2011; Giesen et al., 2012; Krause and Blume, 2013; Hilgersom et al., 2016). The uncertainty in the temperature estimates is strongly affected by the calibration procedure (e.g., Tyler et al., 2009; McDaniel et al., 2018).

Attenuation of light propagating through a fiber depends on its wavelength and therefore is different for Stokes and anti-Stokes scatter. The key in DTS calibration is to differentiate the attenuation from the temperature effects at the point of reflection. There are two types of setups to estimate temperature from Stokes and anti-Stokes scatter: single-ended and double-ended. In single-ended setups, only one end of the fiber is connected to the DTS system, and the difference in attenuation between the Stokes and the anti-Stokes scatter is approximated as constant over the fiber. However, this difference in attenuation is also affected by sharp bends, connectors, and bad splices, which may result in a shift in the temperature if not accounted for. In double-ended setups, measurements are carried out from both ends of the fiber to estimate the difference in attenuation between the Stokes and anti-Stokes scatter at each point along the fiber. In such setups, measurements from both ends of the fiber must be combined, including their uncertainty.

In this chapter, a new calibration procedure is presented for the temperature estimates for single-ended and double-ended setups, including estimates of the uncertainty in the form of confidence intervals. First, a brief review is given of how temperature can be estimated from Stokes and anti-Stokes intensity measurements. Next, the calibration steps are outlined for single-ended and double-ended setups. The spatial and temporal variability in the uncertainty of the temperature are demonstrated by an example of the double-ended calibration procedure. The new calibration procedure is implemented in the open-source Python package “dtscalibration”. This article concludes with a conclusion and a discussion with practical tips to reduce the uncertainty in the temperature.

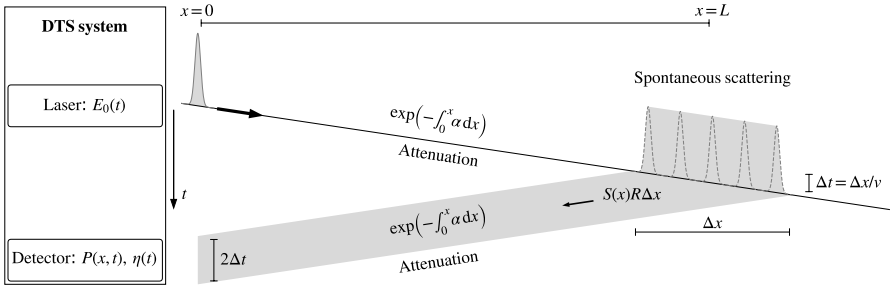


Figure 2.1: Path of a laser pulse.

## 2.2 Estimation of Temperature from Stokes and Anti-Stokes Scatter

The equations that relate the Stokes and anti-Stokes intensity measurements to temperature along a fiber are reviewed here briefly; a comprehensive resource that covers DTS theory is Hartog (2017). The path of a laser pulse emitted by a DTS system through a fiber is shown in Figure 2.1. The laser module emits a short laser pulse that is approximated here as an impulse with energy $E_0$. The pulse travels with the speed of light, $\upsilon$, through the fiber, during which it attenuates with $\exp\left(-\int_0^x \alpha_1\,\mathrm{d}x\right)$, where $\alpha_1$ is the attenuation at the wavelength of the laser pulse. A small fraction, $S(x)R(x)\Delta x$, of the energy of the laser pulse is scattered back over section $\Delta x$, where $S$ is the scattering-loss coefficient for the scattering at the wavelength of the laser pulse, and $R$ is the capture fraction, which depends on the fiber composition (e.g., diameter and numerical aperture (Eriksrud and Mickelson, 1982)). The backscatter pulse is $2\Delta t$ wide and is attenuated again on its way back to the detector. The intensity measured by the detector, $P$ from scattering at $x$ (between times $2x/\upsilon-\Delta t$ and $2x/\upsilon+\Delta t$) is given by (Hartog, 2017, Equation 3.5):

$$P(x,t) = \frac{1}{2}E_0\eta\upsilon SR\exp\left(-\int_0^x 2\alpha_1\,\mathrm{d}x\right) \tag{2.1}$$

where $\eta$ corrects for the sensitivity of the detector and the attenuation between the detector and where the fiber end is connected to the DTS system (Fukuzawa et al., 2013).

In practice, the backscatter is not returned as a pulse, but is dispersed, resulting in spatially correlated measurements. The spreading of the pulse is caused by the finite width of the emitted laser pulse, the measurement response of the detector, and intermodal dispersion of the pulse while propagating through the

fiber. The spreading of the pulse may be experimentally estimated following Simon et al. (Simon et al., 2020). Most of the scattered energy has the same wavelength as the emitted laser pulse (Rayleigh scattering), but a small part has different wavelengths. The scattering-loss coefficient $S_+$ for the Stokes wavelength and $S_-$ for the anti-Stokes wavelength are given by (Bolognini and Hartog, 2013; Hartog, 2017):

$$S_+(x,t) = \frac{K_+}{\lambda_+^4} \frac{\exp\left[\gamma/T(x,t)\right]}{\exp\left[\gamma/T(x,t)\right]-1} \tag{2.2}$$

$$S_-(x,t) = \frac{K_-}{\lambda_-^4} \frac{1}{\exp\left[\gamma/T(x,t)\right]-1} \tag{2.3}$$

where $K_+$ and $K_-$ correct for the fraction of the molecules in the fiber that scatter at the Stokes and anti-Stokes wavelengths (Davey et al., 1989), $\lambda$ is the wavelength, $T$ is the temperature along the fiber in Kelvin, and $\gamma$ is the sensitivity of the Stokes and anti-Stokes scattering to temperature in Kelvin and depends on the fiber material.

The Stokes and anti-Stokes power ($P_+$ and $P_-$, respectively) measured at the detector(s) in a DTS system are given by:

$$P_+(x,t) = \tfrac{1}{2} E_0 \eta_+ \upsilon S_+ R \exp\left[-\int_0^x (\alpha_1 + \alpha_+)\, \mathrm{d}x\right] \tag{2.4}$$

$$P_-(x,t) = \tfrac{1}{2} E_0 \eta_- \upsilon S_- R \exp\left[-\int_0^x (\alpha_1 + \alpha_-)\, \mathrm{d}x\right] \tag{2.5}$$

where $\alpha_+$ and $\alpha_-$ are the attenuation as a function of $x$ at the Stokes and anti-Stokes wavelengths. Most DTS systems use the ratio of Equation 2.4 over Equation 2.5 (Bolognini and Hartog, 2013):

$$\frac{P_+(x,t)}{P_-(x,t)} = \frac{\eta_+(t) K_+/\lambda_+^4}{\eta_-(t) K_-/\lambda_-^4} \exp\left(-\int_0^x \Delta\alpha(x')\, \mathrm{d}x'\right) \exp\left[\gamma/T(x,t)\right] \tag{2.6}$$

where Equations 2.2 and 2.3 are substituted for $S_+$ and $S_-$, respectively, and $\Delta\alpha$ $\left(\mathrm{m}^{-1}\right)$ is the differential attenuation, $\Delta\alpha(x) = \alpha_+ - \alpha_-$. Taking the logarithm of Equation 2.6 gives:

$$I(x,t) = -C(t) - \int_0^x \Delta\alpha(x')\, \mathrm{d}x' + \frac{\gamma}{T(x,t)} \tag{2.7}$$

where

$$I(x,t) = \ln\left(\frac{P_+(x,t)}{P_-(x,t)}\right) \tag{2.8}$$

$$C(t) = \ln\left(\frac{\eta_-(t) K_-/\lambda_-^4}{\eta_+(t) K_+/\lambda_+^4}\right) \tag{2.9}$$

where $C$ is the lumped effect of the difference in gain at $x = 0$ between Stokes and anti-Stokes intensity measurements and the dependence of the scattering intensity on the wavelength. An equation for $T$ may be obtained from Equation 2.7 as:

$$T(x,t) = \frac{\gamma}{I(x,t) + C(t) + \int_0^x \Delta\alpha(x')\,\mathrm{d}x'} \tag{2.10}$$

The temperature along the fiber can now be estimated from the Stokes and anti-Stokes intensity measurements, $I$, if the terms $\gamma$, $C$, and $\int_0^x \Delta\alpha(x')\,\mathrm{d}x'$ are known. These terms are estimated by calibration to reference sections.

## 2.3 Integrated Differential Attenuation

The differential attenuation, $\Delta\alpha$, is different for each fiber type, varies along a fiber, and may change at sharp fiber bends and fiber connections. The integrated differential attenuation ($\int_0^x \Delta\alpha(x')\,\mathrm{d}x'$) differs per setup and must be estimated experimentally to differentiate it from a shift in the temperature. It is estimated differently in single-ended setups than in double-ended setups.

### 2.3.1 Single-Ended Measurements

In single-ended setups, Stokes and anti-Stokes intensity is measured from a single end of the fiber. The differential attenuation is assumed constant along the fiber so that the integrated differential attenuation may be written as (e.g., Hausner et al., 2011):

$$\int_0^x \Delta\alpha(x')\,\mathrm{d}x' \approx \Delta\alpha x \tag{2.11}$$

The temperature can now be written from Equation 2.10 as:

$$T(x,t) \approx \frac{\gamma}{I(x,t) + C(t) + \Delta\alpha x} \tag{2.12}$$

The parameters $\gamma$, $C(t)$, and $\Delta\alpha$ must be estimated from calibration to reference sections, as discussed in Section 2.5. The parameter $C$ must be estimated for each time and is constant along the fiber. Confidence intervals for the estimated temperature are discussed in Section 2.7.1. When jumps in the integrated differential attenuation are expected, the measurements can be split into sections with a constant differential attenuation. Each additional section requires its own reference section to estimate the magnitude of the jump in the integrated differential attenuation.

### 2.3.2 Double-Ended Measurements

In double-ended setups, Stokes and anti-Stokes intensity is measured in two directions from both ends of the fiber. The forward-channel measurements are denoted with subscript F, and the backward-channel measurements are denoted with subscript B. Both measurement channels start at a different end of the fiber and have opposite directions, and therefore have different spatial coordinates. The first processing step with double-ended measurements is to align the measurements of the two measurement channels so that they have the same spatial coordinates. The spatial coordinate $x$ (m) is defined here positive in the forward direction, starting at 0 where the fiber is connected to the forward channel of the DTS system; the length of the fiber is $L$. Consequently, the backward-channel measurements are flipped and shifted to align with the forward-channel measurements. Alignment of the measurements of the two channels is prone to error because it requires the exact fiber length (McDaniel et al., 2018). Depending on the DTS system used, the forward channel and backward channel are measured one after another by making use of an optical switch, so that only a single detector is needed. However, it is assumed in this chapter that the forward channel and backward channel are measured simultaneously, so that the temperature of both measurements is the same. This assumption holds better for short acquisition times with respect to the time scale of the temperature variation, and when there is no systematic difference in temperature between the two channels. The temperature may be computed from the forward-channel measurements (Equation 2.10) with:

$$T_{\mathrm{F}}(x,t) = \frac{\gamma}{I_{\mathrm{F}}(x,t) + C_{\mathrm{F}}(t) + \int_0^x \Delta\alpha(x')\,\mathrm{d}x'} \tag{2.13}$$

and from the backward-channel measurements with:

$$T_{\mathrm{B}}(x,t) = \frac{\gamma}{I_{\mathrm{B}}(x,t) + C_{\mathrm{B}}(t) + \int_x^L \Delta\alpha(x')\,\mathrm{d}x'} \tag{2.14}$$

where $C_{\mathrm{F}}(t)$ and $C_{\mathrm{B}}(t)$ are the parameter $C(t)$ for the forward-channel and backward-channel measurements, respectively. $C_{\mathrm{B}}(t)$ may be different from $C_{\mathrm{F}}(t)$ due to differences in gain, and difference in the attenuation between the detectors and the point the fiber end is connected to the DTS system ($\eta_+$ and $\eta_-$ in Equation 2.9). The calibration procedure presented in van de Giesen et al. (Giesen et al., 2012) approximates $C(t)$ to be the same for the forward and backward-channel measurements, but this approximation is not made here.

Parameter $A(x)$ is introduced to simplify the notation of the double-ended calibration procedure and represents the integrated differential attenuation be-

tween locations $x_1$ and $x$ along the fiber. Location $x_1$ will be selected in Section 2.6.

$$A(x) = \int_{x_1}^{x} \Delta\alpha(x')\,\mathrm{d}x' \tag{2.15}$$

so that Equations 2.13 and 2.14 may be written as:

$$T_{\mathrm{F}}(x,t) = \frac{\gamma}{I_{\mathrm{F}}(x,t) + D_{\mathrm{F}}(t) + A(x)} \tag{2.16}$$

$$T_{\mathrm{B}}(x,t) = \frac{\gamma}{I_{\mathrm{B}}(x,t) + D_{\mathrm{B}}(t) - A(x)} \tag{2.17}$$

where

$$D_{\mathrm{F}}(t) = C_{\mathrm{F}}(t) + \int_{0}^{x_1} \Delta\alpha(x')\,\mathrm{d}x' \tag{2.18}$$

$$D_{\mathrm{B}}(t) = C_{\mathrm{B}}(t) + \int_{x_1}^{L} \Delta\alpha(x')\,\mathrm{d}x' \tag{2.19}$$

Parameters $D_{\mathrm{F}}$ and $D_{\mathrm{B}}$ must be estimated for each time and are constant along the fiber, and parameter $A$ must be estimated for each location and is constant over time. The calibration procedure is discussed in Section 2.6. $T_{\mathrm{F}}$ and $T_{\mathrm{B}}$ are separate approximations of the same temperature at the same time. The estimated $T_{\mathrm{F}}$ is more accurate near $x = 0$ because that is where the signal is strongest. Similarly, the estimated $T_{\mathrm{B}}$ is more accurate near $x = L$. A single best estimate of the temperature is obtained from the weighted average of $T_{\mathrm{F}}$ and $T_{\mathrm{B}}$ as discussed in Section 2.7.2.

## 2.4 Estimation of the Variance of the Noise in the Intensity Measurements

The Stokes and anti-Stokes intensities are measured with detectors, which inherently introduce noise to the measurements. Knowledge of the distribution of the measurement noise is needed for a calibration with weighted observations (Sections 2.5 and 2.6) and to project the associated uncertainty to the temperature confidence intervals (Section 2.7). Two sources dominate the noise in the Stokes and anti-Stokes intensity measurements (Hartog, 2017, p. 125). Close to the laser, noise from the conversion of backscatter to electricity dominates the measurement noise. The detecting component, an avalanche photodiode, produces Poisson-distributed noise with a variance that increases linearly with

the intensity. The Stokes and anti-Stokes intensities are commonly much larger than the standard deviation of the noise, so that the Poisson distribution can be approximated with a Normal distribution with a mean of zero and a variance that increases linearly with the intensity. At the far-end of the fiber, noise from the electrical circuit dominates the measurement noise. It produces Normal-distributed noise with a mean of zero and a variance that is independent of the intensity. However, in this chapter the sum of the two noise sources is approximated with a single Normal distribution with a variance that is independent of the intensity. This approximation holds better for small setups with little attenuation and DTS systems with avalanche photodiodes with a lower gain. In Appendix A, a procedure is presented to compute the intensity-dependent variance of the noise for when this approximation does not hold.



The variance of the noise in the Stokes ($\sigma^2_{P_+}$) and anti-Stokes ($\sigma^2_{P_-}$) measurements are estimated by fitting Equations 2.4 and 2.5 through the Stokes and anti-Stokes intensity measurements of the reference sections, after which the distribution of the residuals is used as an estimate of the distribution of the noise (Richter, 1995). Fiber sections that are used for calibration have an approximately spatially uniform reference temperature ($T_\mathrm{r}(t)$), so that Equations 2.4 and 2.5 are each expressed in a term that varies along the reference section but is constant over time ($H(x)$) and a term that varies with time ($G(t)$) but is constant for a reference section:

$$P_+(x,t) = G_+(t)H_+(x) \tag{2.20}$$

$$P_-(x,t) = G_-(t)H_-(x) \tag{2.21}$$

with

$$G_+(t) = E_0(t)\eta_+(t)\frac{K_+}{\lambda_+^4}\frac{\exp\left[\gamma/T_\mathrm{r}(t)\right]}{\exp\left[\gamma/T_\mathrm{r}(t)\right]-1} \tag{2.22}$$

$$G_-(t) = E_0(t)\eta_-(t)\frac{K_-}{\lambda_-^4}\frac{1}{\exp\left[\gamma/T_\mathrm{r}(t)\right]-1} \tag{2.23}$$

$$H_+(x) = \tfrac{1}{2}\upsilon R\exp\left(-\int_0^x\left[\alpha_\mathrm{I}(x')+\alpha_+(x')\right]\mathrm{d}x'\right) \tag{2.24}$$

$$H_-(x) = \tfrac{1}{2}\upsilon R\exp\left(-\int_0^x\left[\alpha_\mathrm{I}(x')+\alpha_-(x')\right]\mathrm{d}x'\right) \tag{2.25}$$

Values for $G(t)$ and $H(x)$ are obtained by minimizing the residuals between the Stokes and anti-Stokes intensity measurements and Equations 2.20 and 2.21 with a standard routine. Here, the "minimize" routine of the Python package scipy.optimize (Virtanen et al., 2020) is used, and is implemented in the package

"dtscalibration" (Section 2.8). $G(t)$ and $H(x)$ are, of course, highly correlated (Equations 2.20 and 2.21), but that is not relevant here as only the product of $G(t)$ and $H(x)$ is of interest. The residuals between the fitted product of $G(t)$ and $H(x)$ and the Stokes and anti-Stokes intensity measurements are attributed to the noise from the detectors. The variance of the residuals is used as a proxy for the variance of the noise in the Stokes and anti-Stokes intensity measurements. The consequence of a non-uniform temperature of the reference sections on the estimated variance is described in Section 2.10.

## 2.5 Single-Ended Calibration Procedure

In single-ended calibration, the temperature is estimated from Stokes and anti-Stokes intensity measurements with Equation 2.12. The parameters that need to be estimated from calibration are $\gamma$, $\Delta\alpha$, and $C$, where $C$ needs to be estimated for each time step. The parameters are estimated from the reference temperature at $M$ locations along the reference sections and at $N$ times. Equation 2.7 is reorganized to amend it for linear regression. The observation at location $m$ and time $n$, denoted with $I_{m,n}$, is written as a linear combination of the unknown parameters:

$$I_{m,n} = \frac{1}{T_{m,n}}\gamma - x_m\Delta\alpha - C_n, \quad \text{with} \quad m = 1, 2, .., M \quad \text{and} \quad n = 1, 2, .., N \tag{2.26}$$

where $T_{m,n}$ is the reference temperature at location $m$ and time $n$, $x_m$ is the location of point $m$ along the reference sections, and $C_n$ is the constant $C$ of the fiber at time $n$. In total, there are $N + 2$ unknown parameters and $MN$ observations.

The system of $N$ Equation 2.26 for location $m$ may be written in vector form as:

$$\mathbf{y}_m = \mathbf{X}_m\mathbf{a} + \boldsymbol{\epsilon}_m, \tag{2.27}$$

where $\boldsymbol{\epsilon}_m$ are the residuals between the observed values and the fitted values for location $m$, and

$$\mathbf{y}_m = \begin{bmatrix} I_{m,1} \\ I_{m,2} \\ \vdots \\ I_{m,N} \end{bmatrix}, \quad \mathbf{X}_m = \begin{bmatrix} \frac{1}{T_{m,1}} & -x_m & -1 & & & \\ \frac{1}{T_{m,2}} & -x_m & & -1 & & \\ \vdots & \vdots & & & \ddots & \\ \frac{1}{T_{m,N}} & -x_m & & & & -1 \end{bmatrix}, \quad \mathbf{a} = \begin{bmatrix} \gamma \\ \Delta\alpha \\ C_1 \\ C_2 \\ \vdots \\ C_N \end{bmatrix} \tag{2.28}$$

The vector **a** contains the unknown parameters that are to be estimated. The system of $MN$ equations for all locations may be combined into one system of equations:

$$\mathbf{y} = \mathbf{X}\mathbf{a} + \boldsymbol{\epsilon}, \tag{2.29}$$

where

$$\mathbf{y} = \begin{bmatrix} \mathbf{y}_1 \\ \mathbf{y}_2 \\ \vdots \\ \mathbf{y}_M \end{bmatrix}, \quad \mathbf{X} = \begin{bmatrix} \mathbf{X}_1 \\ \mathbf{X}_2 \\ \vdots \\ \mathbf{X}_M \end{bmatrix}, \quad \boldsymbol{\epsilon} = \begin{bmatrix} \boldsymbol{\epsilon}_1 \\ \boldsymbol{\epsilon}_2 \\ \vdots \\ \boldsymbol{\epsilon}_M \end{bmatrix} \tag{2.30}$$

This system (Equation 2.29) is solved by minimizing the sum of the squared weighted residuals $\chi^2$:

$$\chi^2 = (\mathbf{y} - \mathbf{X}\mathbf{a})^\intercal \mathbf{W} (\mathbf{y} - \mathbf{X}\mathbf{a}) \tag{2.31}$$

where $^\intercal$ refers to the transposed matrix and $\mathbf{W}$ is a diagonal matrix given by

$$\mathrm{diag}\,(\mathbf{W}) = \begin{bmatrix} \mathbf{W}_1 \\ \mathbf{W}_2 \\ \vdots \\ \mathbf{W}_M \end{bmatrix}, \quad \mathbf{W}_m = \begin{bmatrix} \frac{1}{\sigma^2_{I_{m,1}}} \\ \frac{1}{\sigma^2_{I_{m,2}}} \\ \vdots \\ \frac{1}{\sigma^2_{I_{m,N}}} \end{bmatrix} \tag{2.32}$$

The variance, $\sigma^2_{I_{m,n}}$, of the distribution of the noise in the observation at location $m$, time $n$, is a function of the variance of the noise in the Stokes and anti-Stokes intensity measurements ($\sigma^2_{P_+}$ and $\sigma^2_{P_-}$), and is approximated with (Ku et al., 1966):

$$\sigma^2_{I_{m,n}} \approx \left[\frac{\partial I_{m,n}}{\partial P_{m,n+}}\right]^2 \sigma^2_{P_+} + \left[\frac{\partial I_{m,n}}{\partial P_{m,n-}}\right]^2 \sigma^2_{P_-} \tag{2.33}$$

$$\approx \frac{1}{P^2_{m,n+}} \sigma^2_{P_+} + \frac{1}{P^2_{m,n-}} \sigma^2_{P_-} \tag{2.34}$$

The variance of the noise in the Stokes and anti-Stokes intensity measurements is estimated directly from Stokes and anti-Stokes intensity measurements using the steps outlined in Section 2.4.

The sum of the squared weighted residuals may be minimized with a standard routine. In this chapter, a custom sparse implementation of the weighted

least squares routine of the Python package Statsmodels is used (Seabold and Perktold, 2010), which returns the optimal parameter set, the covariance matrix of the optimal parameter set, and the residuals (this is part of the Python package "dtscalibration", which is described in Section 2.8). The number of reference sections required for calibration is discussed in Section 2.10.2.

## 2.6 Double-Ended Calibration Procedure

In double-ended calibration, the temperature is estimated using Stokes and anti-Stokes intensity measurements from both ends of the fiber. The temperature is estimated from Equations 2.16 and 2.17. The unknown parameters $\gamma$, $D_{\mathrm{F}}(t)$, $D_{\mathrm{B}}(t)$, and $A(x)$ are obtained from calibration to reference sections, similar to the single-ended calibration procedure. $x_1$ is chosen as the first location of the first reference section, so that the value for $A$ at that location equals 0 (Equation 2.15). There are $M$ locations along the reference sections where the temperature is measured at $N$ times. In total there are $2N+M$ unknowns: parameter $\gamma$, $N$ parameters $D_{\mathrm{F}}$, $N$ parameters $D_{\mathrm{B}}$, and $M-1$ parameters $A$ (since $A_1 = 0$). Equations 2.16 and 2.17 are reorganized to amend them for linear regression as:

$$\left.\begin{aligned} I_{\mathrm{F},m,n} &= \frac{1}{T_{m,n}}\gamma - D_{\mathrm{F},n} - A_m \\ I_{\mathrm{B},m,n} &= \frac{1}{T_{m,n}}\gamma - D_{\mathrm{B},n} + A_m \end{aligned}\right\} \quad \text{with} \quad m = 1, 2, .., M \quad \text{and} \quad n = 1, 2, .., N \tag{2.35}$$

where $D_{\mathrm{F},n}$ is the constant $D_{\mathrm{F}}$ at time $n$, $D_{\mathrm{B},n}$ is the constant $D_{\mathrm{B}}$ at time $n$ $A_m$ is the constant $A$ at location $m$, and $A_1 = 0$. The system of $2N$ equations for location $m$ may be written as:

$$\mathbf{y}_m = \mathbf{X}_m \mathbf{a} + \boldsymbol{\epsilon}_m, \tag{2.36}$$

where

$$\mathbf{y}_m = \begin{bmatrix} \mathbf{F}_m \\ \mathbf{B}_m \end{bmatrix}, \quad \mathbf{X}_m = \begin{bmatrix} \mathbf{R}_m & -\mathbf{I}(N,N) & \mathbf{0}(N,N) & -\mathbf{Q}_m \\ \mathbf{R}_m & \mathbf{0}(N,N) & -\mathbf{I}(N,N) & \mathbf{Q}_m \end{bmatrix}, \tag{2.37}$$

$$\mathbf{F}_m = \begin{bmatrix} I_{\mathrm{F},m,1} \\ I_{\mathrm{F},m,2} \\ \vdots \\ I_{\mathrm{F},m,N} \end{bmatrix}, \quad \mathbf{B}_m = \begin{bmatrix} I_{\mathrm{B},m,1} \\ I_{\mathrm{B},m,2} \\ \vdots \\ I_{\mathrm{B},m,N} \end{bmatrix}, \quad \mathbf{R}_m = \begin{bmatrix} \frac{1}{T_{m,1}} \\ \frac{1}{T_{m,2}} \\ \vdots \\ \frac{1}{T_{m,N}} \end{bmatrix} \tag{2.38}$$

where $\mathbf{I}$ is an identity matrix with its number of rows and columns between brackets, $\mathbf{0}$ is a matrix of zeros with its number of rows and columns between brackets, and $\epsilon_m$ are the residuals at location $m$. The matrix $\mathbf{Q}_m$ is defined differently for the first location than for the other locations. For $m = 1$, $\mathbf{Q}_m$ is a matrix of zeros size $N$ by $M - 1$. For $m > 1$, $\mathbf{Q}_m$ is a matrix of zeros of size $N$ by $M - 1$ except for column $m - 1$, which contains ones. The vector $\mathbf{a}$ contains the unknown parameters, has length $2N + M$, and is given by:

$$\mathbf{a} = \begin{bmatrix} \gamma \\ \mathbf{a}_{D,\mathrm{F}} \\ \mathbf{a}_{D,\mathrm{B}} \\ \mathbf{a}_A \end{bmatrix}, \quad \mathbf{a}_{D,\mathrm{F}} = \begin{bmatrix} D_{\mathrm{F},1} \\ D_{\mathrm{F},2} \\ \vdots \\ D_{\mathrm{F},N} \end{bmatrix}, \quad \mathbf{a}_{D,\mathrm{B}} = \begin{bmatrix} D_{\mathrm{B},1} \\ D_{\mathrm{B},2} \\ \vdots \\ D_{\mathrm{B},N} \end{bmatrix}, \quad \mathbf{a}_A = \begin{bmatrix} A_2 \\ A_3 \\ \vdots \\ A_M \end{bmatrix} \tag{2.39}$$

The weights of the observations at location $m$ are given by:

$$\mathrm{diag}\left(\mathbf{W}_m\right) = \begin{bmatrix} 1/\sigma^2\left[\mathbf{F}_m\right] \\ 1/\sigma^2\left[\mathbf{B}_m\right] \end{bmatrix} \tag{2.40}$$

where the elements of $\sigma^2\left[\mathbf{F}_m\right]$ and $\sigma^2\left[\mathbf{B}_m\right]$ are approximated with Equation 2.34 applied to the forward and backward channels, respectively.

The equations for all $M$ locations are gathered in a single set of equations given by Equations 2.29 and 2.30, where $\mathbf{y}_m$, $\mathbf{X}_m$, $\mathbf{a}$ are given by Equations 2.37–2.39. This is a system of $2MN$ equations for $M + 2N$ unknown parameters. The system is solved by minimizing $\chi^2$ as given by Equation 2.31, where $\mathbf{W}$ is given by Equation 2.32 with Equation 2.40 for $\mathbf{W}_m$.

The set of estimated parameters contains estimates of $A$ for the locations along the reference sections only. An estimate of $A$ and its variance for locations outside the reference sections are required to estimate the temperature outside of the reference sections. An estimate of $A$ for location $p$ and time $n$ outside the reference sections is obtained by setting $T_\mathrm{F} = T_\mathrm{B}$ using Equations 2.16 and 2.17, which gives:

$$A_{p,n} = \frac{I_{\mathrm{B},p,n} - I_{\mathrm{F},p,n}}{2} + \frac{D_{\mathrm{B},n} - D_{\mathrm{F},n}}{2} \tag{2.41}$$

The variance of $A_{p,n}$ is approximated with:

$$\sigma^2\left[A_{p,n}\right] \approx \frac{1}{4}\left(\sigma^2\left[I_{\mathrm{B},p,n}\right] + \sigma^2\left[I_{\mathrm{F},p,n}\right] + \sigma^2\left[D_{\mathrm{F},n}\right] + \sigma^2\left[D_{\mathrm{B},n}\right] - 2\sigma\left[D_{\mathrm{F},n}, D_{\mathrm{B},n}\right]\right) \tag{2.42}$$

$$\approx \frac{1}{4}\left(\frac{1}{P^2_{\mathrm{B},m,n+}}\sigma^2_{P_{\mathrm{B}+}} + \frac{1}{P^2_{\mathrm{B},m,n-}}\sigma^2_{P_{\mathrm{B}-}} + \frac{1}{P^2_{\mathrm{F},m,n+}}\sigma^2_{P_{\mathrm{F}+}} + \frac{1}{P^2_{\mathrm{F},m,n-}}\sigma^2_{P_{\mathrm{F}-}} + \sigma^2\left[D_{\mathrm{F},n}\right] + \sigma^2\left[D_{\mathrm{B},n}\right] - 2\sigma\left[D_{\mathrm{F},n}, D_{\mathrm{B},n}\right]\right) \tag{2.43}$$

where $\sigma^2_{P_{\mathrm{B}+}}$, $\sigma^2_{P_{\mathrm{B}-}}$, $\sigma^2_{P_{\mathrm{F}+}}$, and $\sigma^2_{P_{\mathrm{F}-}}$ are estimated directly from the Stokes and anti-Stokes intensity measurements of the forward and the backward channels using the procedure presented in Section 2.4, the terms $\sigma^2\left[D_{\mathrm{F},n}\right]$ and $\sigma^2\left[D_{\mathrm{B},n}\right]$ are parameter uncertainties from the diagonal of the covariance matrix, and the term $\sigma\left[D_{\mathrm{F},n}, D_{\mathrm{B},n}\right]$ is the square-root of the covariance between $D_{\mathrm{F},n}$ and $D_{\mathrm{B},n}$ from the covariance matrix. A single estimate of $A_p$ and $\sigma^2\left[A_p\right]$ at location $p$ is obtained using the inverse temporal-variance weighted mean:

$$A_p = \sigma^2\left[A_p\right]\left(\sum_{n=1}^{N}\frac{A_{p,n}}{\sigma^2\left[A_{p,n}\right]}\right) \tag{2.44}$$

$$\sigma^2\left[A_p\right] = \frac{1}{\sum_{n=1}^{N} 1/\sigma^2\left[A_{p,n}\right]} \tag{2.45}$$

The number of reference sections required for calibration is discussed in Section 2.10.2.

## 2.7 Confidence Intervals of the Temperature

The uncertainty in the estimated temperature varies along the fiber as the laser pulse attenuates when propagating through the fiber, and varies over time due to varying gains and losses in the DTS device. The two sources that contribute to the uncertainty in the temperature estimate are the uncertainty in the calibrated parameters and the uncertainty associated with the noise in the Stokes and anti-Stokes intensity measurements. The former dominates the uncertainty in the estimated temperature for measurements with longer acquisition times,

while the latter dominates measurements with shorter acquisition times. Other sources of possible uncertainty are not taken into account here. These include the uncertainty introduced by the model that relates measured Stokes and anti-Stokes intensities to temperature, and the uncertainty in measured temperatures obtained with external sensors. The latter is generally much smaller than the uncertainty in the DTS temperature from the noise in the Stokes and anti-Stokes intensity measurements.



Estimation of the confidence intervals of the temperature starts with estimating separate probability density functions for the Stokes and anti-Stokes intensity measurements and the calibrated parameters. The probability density functions are propagated through the model using a Monte Carlo sampling procedure following the steps from Joint Committee for Guides in Metrology (2008a) and Joint Committee for Guides in Metrology (2008b). This procedure results in an approximation of the probability density function for the estimated temperature, which is different at each location and varies over time. Various summarizing statistics are computed from the approximate probability density function, including the expected value, the standard deviation, and the confidence intervals. The standard deviation is also called the temperature resolution, but in line with Joint Committee for Guides in Metrology (2008a), the term standard uncertainty is used here. The procedure is explained first for single-ended measurements, followed by the procedure for double-ended measurements.

### 2.7.1 Single-Ended Measurements

Estimation of the confidence intervals for the temperatures measured with a single-ended setup consists of five steps. First, the variances of the Stokes and anti-Stokes intensity measurements are estimated following the steps in Section 2.4. A Normal distribution is assigned to each intensity measurement that is centered at the measurement and using the estimated variance. Second, a multi-variate Normal distribution is assigned to the estimated parameters using the covariance matrix from the calibration procedure presented in Section 2.5. Third, the distributions are sampled, and the temperature is computed with Equation 2.12. Fourth, step three is repeated, e.g., 10,000 times for each location and for each time. The resulting 10,000 realizations of the temperatures approximate the probability density functions of the estimated temperature at that location and time. Fifth, the standard uncertainties are computed with the standard deviations of the realizations of the temperatures, and the 95% confidence intervals are computed from the 2.5% and 97.5% percentiles of the realizations of the temperatures.

### 2.7.2 Double-Ended Measurements

Double-ended setups require four additional steps to estimate the confidence intervals for the temperature. First, the variances of the Stokes and anti-Stokes intensity measurements of the forward and backward channels are estimated following the steps in Section 2.4. A Normal distribution is assigned to each intensity measurement that is centered at the measurement and using the estimated variance. Second, a multi-variate Normal distribution is assigned to the estimated parameters using the covariance matrix from the calibration procedure presented in Section 2.6. Third, Normal distributions are assigned for $A$ for each location outside of the reference sections. These distributions are centered around $A_p$ and have variance $\sigma^2\left[A_p\right]$ given by Equations 2.44 and 2.45. Fourth, the distributions are sampled and $T_{\mathrm{F},m,n}$ and $T_{\mathrm{B},m,n}$ are computed with Equations 2.16 and 2.17, respectively. Fifth, step four is repeated to compute, e.g., 10,000 realizations of $T_{\mathrm{F},m,n}$ and $T_{\mathrm{B},m,n}$ to approximate their probability density functions. Sixth, the standard uncertainties of $T_{\mathrm{F},m,n}$ and $T_{\mathrm{B},m,n}$ ($\sigma\left[T_{\mathrm{F},m,n}\right]$ and $\sigma\left[T_{\mathrm{B},m,n}\right]$) are estimated with the standard deviation of their realizations. Seventh, for each realization $i$ the temperature $T_{m,n,i}$ is computed as the weighted average of $T_{\mathrm{F},m,n,i}$ and $T_{\mathrm{B},m,n,i}$:

$$T_{m,n,i} = \sigma^2\left[T_{m,n}\right]\left(\frac{T_{\mathrm{F},m,n,i}}{\sigma^2\left[T_{\mathrm{F},m,n}\right]} + \frac{T_{\mathrm{B},m,n,i}}{\sigma^2\left[T_{\mathrm{B},m,n}\right]}\right) \tag{2.46}$$

where

$$\sigma^2\left[T_{m,n}\right] = \frac{1}{1/\sigma^2\left[T_{\mathrm{F},m,n}\right] + 1/\sigma^2\left[T_{\mathrm{B},m,n}\right]} \tag{2.47}$$

The best estimate of the temperature $T_{m,n}$ is computed directly from the best estimates of $T_{\mathrm{F},m,n}$ and $T_{\mathrm{B},m,n}$ as:

$$T_{m,n} = \sigma^2\left[T_{m,n}\right]\left(\frac{T_{\mathrm{F},m,n}}{\sigma^2\left[T_{\mathrm{F},m,n}\right]} + \frac{T_{\mathrm{B},m,n}}{\sigma^2\left[T_{\mathrm{B},m,n}\right]}\right) \tag{2.48}$$

Alternatively, the best estimate of $T_{m,n}$ can be approximated with the mean of the $T_{m,n,i}$ values. Finally, the 95% confidence interval for $T_{m,n}$ are estimated with the 2.5% and 97.5% percentiles of $T_{m,n,i}$.

## 2.8 Python Implementation

The presented calibration procedure is implemented in the Python package "dtscalibration" (Tombe and Schilperoort, 2020). It is open source, has a BSD 3-or-later license and is available online at `https://github.com/dtscalibration/`

`python-dts-calibration`, together with installation instructions, examples, and documentation. The package reads DTS measurement files into an object, which has several calibration and plotting methods. Calibration and calculation of confidence intervals can be conducted within 10 lines of Python code, as is demonstrated in the examples of Section 2.9 and Supplementary Materials 1. Several routines are implemented to read Stokes and anti-Stokes intensity measurement files from the following DTS devices: AP Sensing CP320, Sensornet Oryx, Sensornet Halo, SensorTran 5100, Silixa Ultima, Silixa XT. The package inherits many functions (e.g., visualization, parallel computing) from xarray (Hoyer and Hamman, 2017) so that the code base remains small. Most computations are performed by Dask (Dask Development Team, 2016) in chunks and in parallel, so that gigabytes of DTS measurement data can be processed on a personal computer with limited memory.



## 2.9 Example

An example of a double-ended setup is presented to demonstrate the spatial and temporal variability in the uncertainty of the temperature. This example attempts to estimate the uncertainty of the temperature along the entire fiber for a given acquisition time. The uncertainty in the estimated temperature can easily be reduced by increasing the acquisition time, but that limits the ability to observe temporal variation in temperature. Alternatively, the uncertainty can be reduced by increasing the sampling distance, but that limits the ability to observe spatial variation in temperature.

### 2.9.1 Setup and Data Collection

A schematic representation of the setup is shown in Figure 2.2. Sections of the fiber are submerged in water baths with a measured temperature as listed in Table 2.1. A uniform temperature in all water baths is desired so that the temperature measured with an external temperature sensor resembles the temperature of the fiber. Therefore, an aluminum bath filled with water is placed in a cold climate room, and a second one is placed in a warm climate room. The air in the climate rooms circulates around the water baths and the air temperature is kept constant with a maximum variation of 0.5 °C to achieve a uniform temperature in the water baths. A cooler turns on if the air temperature in the climate rooms is 0.3 °C above its target temperature, and a heater turns on if the air temperature in the climate rooms is 0.2 °C below the target temperature. Both baths contain two coils of fiber. Another coil of fiber is placed in a cooler box filled with water, without temperature control, but with an aquarium air pump to attempt to mix

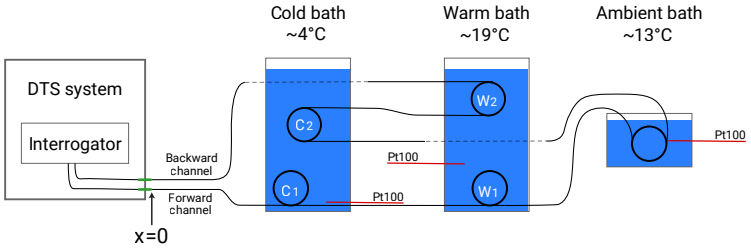


Figure 2.2: The setup of the example.

Table 2.1: Fiber sections submerged in water baths.

| Name | Fiber Section (m) | Average Temperature (°C) | Number of Measurement Locations | Notes |
|---|---|---|---|---|
| Cold 1 | 7.5–17.0 | 4.35 | 37 | Used for calibration |
| Warm 1 | 24.0–34.0 | 18.52 | 39 | Used for calibration |
| Ambient | 40.0–50.0 | 12.62 | 39 | |
| Cold 2 | 70.0–80.0 | 4.35 | 39 | |
| Warm 2 | 85.0–95.0 | 18.52 | 39 | |

the water and achieve a uniform temperature. All coils of fiber are lifted from the bottom of the baths with plastic spacers so that the coils are approximately centered. The setup was left to rest to achieve a stable and uniform temperature in the water baths before starting the measurements.

The DTS system used in this example is a Silixa Ultima-S DTS system (Hertfordshire, UK) that measures fibers up to 2 km with a factory-reported spatial resolution of approximately 30 cm. The system is configured to measure the Stokes and anti-Stokes intensity with an acquisition time of 2 s in the forward direction and 2 s in the backward direction, every 12.7 cm along 100 m of fiber (Figure 2.2). The system's specification sheet lists several values for the standard uncertainty (referred to as the temperature resolution) for different single-ended setups using the built-in calibration routine. According to the specification sheet, the standard uncertainty is 0.34 °C if the fiber is shorter than 500 m, sampled every 12.7 cm, and measured for a second, which translates roughly to a standard uncertainty of 0.17 °C for an acquisition time of 4 s. The used fiber (j-BendAble made by j-fiber GmbH, Jena, Germany) is an OM3 fiber with a germanium-doped core with a diameter of 50 µm and a silica cladding with a diameter of 125 µm. The temperature in the warm- and cold-water baths is measured by the DTS system with two Pt100 RTDs, and the temperature in the ambient water bath is measured with a Pt100 RTD using a Fluke 1524 Handheld Thermometer.

### 2.9.2 Estimation of the Temperature and the Associated Uncertainty

The variance of the noise in the Stokes and anti-Stokes intensity measurements of the forward and backward channels were estimated using measurements from the two reference sections ('Cold 1' and 'Warm 1' in Table 2.1) with the procedure described in Section 2.4. A scatter plot with the residuals of the intensity measurements of the forward channel is shown in Appendix B. The residuals of the Stokes intensity measurements are plotted on the horizontal axis and the residuals of the anti-Stokes intensity measurements on the vertical axis. The residuals may be approximated with a Normal distribution and show no clear correlation (Pearson correlation coefficient is 0.02).



Double-ended calibration was performed to estimate the optimal parameter values and their covariance following the procedure described in Section 2.6. The calibration uses measurements from the two reference sections (Table 2.1). Instead of using all the measurements from the measurement period of one day, 1000 time samples were used, evenly spaced over a single day ($N = 1000$). Inherent to DTS systems, neighboring measurement locations are spatially correlated (Section 2.2). To reduce this correlation, every other measurement location was disregarded so that the distance between the used measurement locations is 25.4 cm, which is close to the spatial resolution and results in a total of 193 measurement locations. The number of locations along the reference sections that are used for calibration is 76 ($M = 76$).

The 95% confidence intervals are estimated with the approach described in Section 2.7. The estimated temperature and its confidence interval at the first time step are shown in Figure 2.3a. The difference between the estimated temperature and reference temperature is shown in Figure 2.3b with markers, where the confidence interval minus the estimated temperature at the first time step is shown with a blue fill. For the estimation of the confidence intervals, a Monte Carlo sample size of 10,000 was used; doubling the sample size for this measurement setup did not change the 95% confidence intervals significantly, but it did smooth the edges of the confidence intervals (i.e., the roughness of the edges of the blue fill in Figure 2.3b). The percentage of reference temperature measurements that fall within the 95% confidence interval of the estimated temperature for all 1000 time steps are listed for each section in Table 2.2. For the ambient bath, only 92.3% of the temperature measurements fall within the 95% confidence interval.

The mean difference between the reference temperature and the estimated temperature for all times is shown for each location along the reference sections in Figure 2.4 with orange markers. The estimated temperature of the ambient

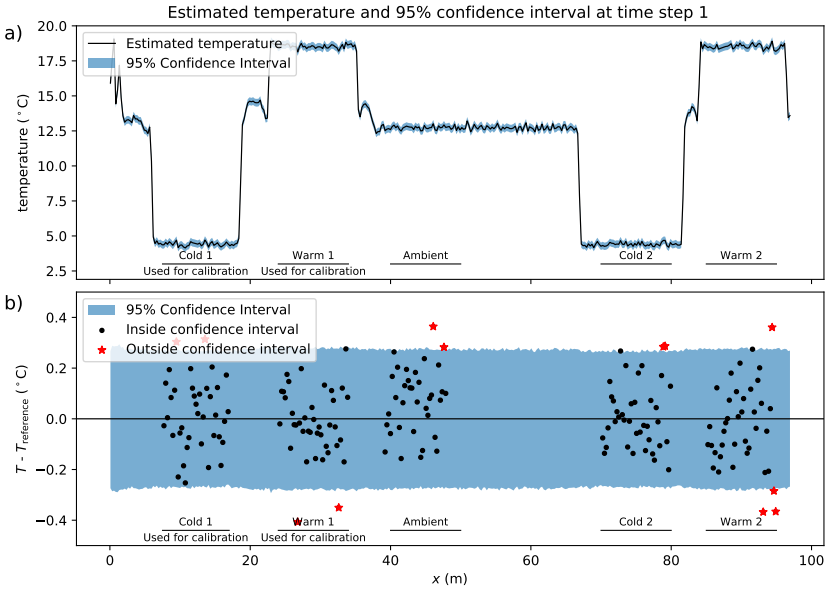


Figure 2.3: (**a**) Temperature with its 95% confidence intervals at the first time step. (**b**) Differences between the estimated temperature and the reference temperature at the first time step.

Table 2.2: Percentage of reference temperature within estimated 95% confidence intervals.

| Cold 1 | Warm 1 | Ambient | Cold 2 | Warm 2 | Total |
|---|---|---|---|---|---|
| 95.6% | 95.0% | 92.3% | 94.7% | 94.3% | 94.4% |

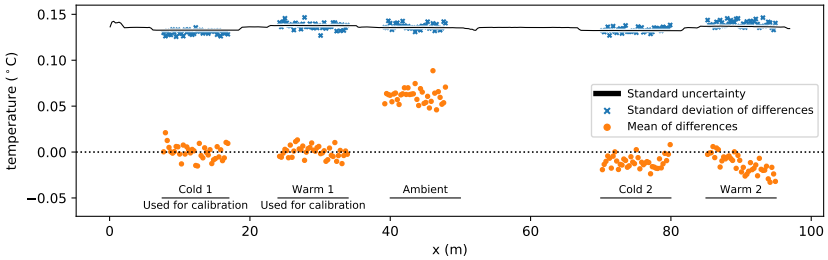


Figure 2.4: Spatial variation of the standard uncertainty of the estimated temperature, and the mean and standard deviation of the differences between the estimated and reference temperature.

bath is on average 0.06 °C above the corresponding reference temperature. This bias may be the result of either the external temperature sensor not representing the temperature of the fiber due to local temperature variations in the water bath, or the external temperature sensor is calibrated differently. This could have been confirmed by simultaneously submerging all temperature sensors in a water bath and comparing their measurements, but this was not done here. The mean difference of reference section Warm 2 shows a spatial correlation between the mean differences, which can indicate non-uniform temperatures in the water bath. The spatial variability in the standard deviation of the differences between the reference temperature and the estimated temperature is shown in Figure 2.4 with blue markers. The standard uncertainty is estimated for each location from the Monte Carlo samples from all times and is shown with a black line. It varies with the temperature, with slightly smaller values for the fiber sections in the cold baths and slightly larger values for the fiber sections in the warm baths. The standard deviation of the difference between the reference temperature and the estimated temperature for all times is shown with blue markers and is well described at each location with the standard uncertainty.

The mean difference between the reference temperature and the estimated temperature for all reference locations is plotted over time in Figure 2.5 with orange markers. Each marker represents the mean of 193 differences. The mean of the differences are slightly above zero probably caused by the bias in the ambient bath temperature. The standard uncertainty at each time is computed from the Monte Carlo samples from all locations and is shown with a black line. The standard deviation of the difference between the reference and estimated temperature for all locations is shown with blue markers, which roughly follow the estimated standard uncertainties. The increase in standard uncertainty after 11.5 h coincides with a strong decrease in Stokes and anti-Stokes intensity of the

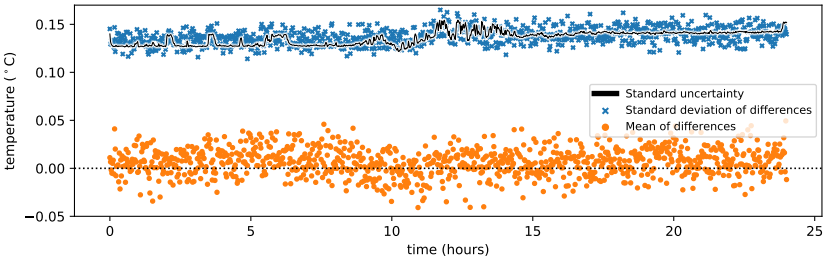


Figure 2.5: Temporal variation of the standard uncertainty of the estimated temperature, and the mean and standard deviation of the differences between the estimated and reference temperature.

forward and backward channels (not shown here), caused by either a decrease in laser strength or a decrease in sensitivity of the detector.

### 2.9.3 Effect of Parameter Uncertainty

As stated, the uncertainty of the temperature is a function of the uncertainty in the estimated parameters and the uncertainty in the Stokes and anti-Stokes intensity measurements. The estimation of the standard uncertainty of the temperature was repeated except for that the covariance matrix of the optimal parameters was not propagated to the Monte Carlo set, so that the standard uncertainty consists of only the uncertainty introduced by the noise in the Stokes and anti-Stokes intensity measurements (Section 2.7.2). The standard uncertainty of the temperature was recalculated, and was on average 0.001 °C smaller than the original values and did not show any patterns or trends. Hence, it is concluded that for this experiment the contribution of the parameter uncertainty to the standard uncertainty is small compared to the uncertainty introduced by the noise in the Stokes and anti-Stokes intensity measurements.

### 2.9.4 Effect of Difference in Reference Temperatures

As stated in Section 2.6, reference sections at two different temperatures are required to estimate the parameters that relate Stokes and anti-Stokes intensity measurements to temperature and only one reference section is needed if its temperature varies sufficiently over time. To test the consequence of calibrating to reference sections with a variation in temperature that is too small, an additional calibration is performed with two reference sections at the same temperature: Cold 1 and Cold 2 (Table 2.1). 95% of the reference temperatures were between 4.33 and 4.39 °C. Values for the $A(x)$ parameters along the reference sections are correctly estimated, but the parameters $\gamma$, $D_{\mathrm{F}}(t)$, and $D_{\mathrm{B}}(t)$ are

not. Their estimated values are of the right order of magnitude, and the temperature of the cold-water baths is estimated well with those parameters (not shown). The temperatures outside the 4.33–4.39 °C range are not correctly estimated. The 95% confidence intervals for the estimated temperature outside the reference sections are enormously wide, because of the large parameter uncertainty. The standard uncertainty of the $A(x)$ estimates are the same as in the first calibration configuration, but the standard uncertainty of the $\gamma$, $D_{\mathrm{F}}(t)$, and $D_{\mathrm{B}}(t)$ estimates are two orders of magnitude larger than their estimated values. As expected, this calibration configuration failed due to the lack of difference in temperature between the reference sections and the lack of temperature variation of the reference sections.



## 2.10 Discussion

### 2.10.1 Improved Temperature Estimation for Double-Ended Setups

The estimation of the uncertainty of the temperature from Stokes and anti-Stokes intensity measurements requires several approximations. In this section, the practical implications of these approximations are assessed. Single-ended measurements have several inherent drawbacks compared to double-ended measurements. The differential attenuation is approximated to be constant, step changes are neglected (e.g., fiber splices, sharp bends), and fiber sections with a different differential attenuation are not accounted for (e.g., coiled up fiber sections, different fiber types). This includes sharp bends in 'bend-tolerant' fiber (Remouche et al., 2012; Hilgersom et al., 2016). The step losses in Stokes and anti-Stokes intensity measurements can be corrected manually, if they are identified and the temperature is the same at either side of the step loss (Hausner and Kobs, 2016). Uncorrected step losses result in a bias in the estimated temperature that is not expressed in the confidence intervals. Commercially available DTS systems usually include an internal reference fiber section for calibration purposes. The use of the internal reference section is not recommended for single-ended measurements because of the step change in the integrated differential attenuation at the connector. The type of the internal fiber is most likely different, with a different differential attenuation than the fiber connected to the DTS system. Hence, it is recommended to use double-ended setups rather than single-ended setups.

The proposed calibration procedure to estimate the integrated differential attenuation in double-ended setups differs from the two-step procedure of van de

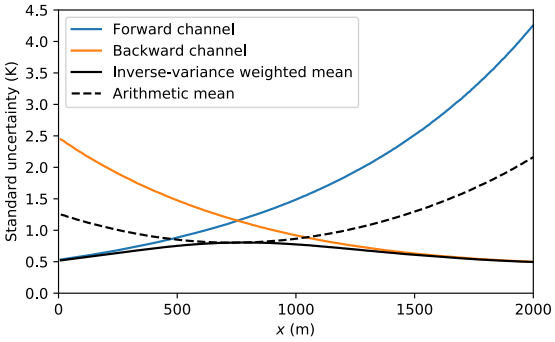


Figure 2.6: Synthetic example of the standard uncertainty of the estimated temperature using arithmetic mean and the inverse-variance weighted mean.

Giesen et al. (Giesen et al., 2012). They estimate the differential attenuation integrated between neighboring measurement locations, average them over time for the entire fiber, and sum them to estimate the integrated differential attenuation. In Section 2.6 of this chapter, estimation of the integrated differential attenuation is achieved in one step, and formulated so that it can be used in weighted linear regression.

The presented calibration procedure can lead to better temperature estimates compared to existing calibration procedures. Parameters that are time invariant are kept constant and are estimated from all available data, which improves their estimation. By weighing Stokes and anti-Stokes measurements with their uncertainty, the estimation of parameters is less affected by measurement noise along reference sections with a low signal strength, i.e., at the end of the fiber.

Furthermore, weighted averaging of the temperature from the forward and backward-channel measurements results in better temperature estimates than arithmetic averaging or using either of the individual channel measurements. Consider the synthetic temperature measurement of a double-ended setup shown in Figure 2.6. The approximated standard uncertainty is computed using the procedure outlined in Section 2.7.2 and is shown for the forward-channel temperature measurements in orange and for the backward channel in blue. The standard uncertainty of the inverse-variance weighted mean is shown with the solid black line and is much smaller near the ends of the fiber. The standard uncertainty of the inverse-variance weighted mean is equal to that of the arithmetic mean where the standard uncertainty of the forward-channel measurements is equal to that of the backward-channel measurements.

### 2.10.2 Calibration to Reference Sections

The presented calibration procedures require either one or two reference sections with a different temperature. In single-ended setups, two reference sections are needed to differentiate between $\gamma/T_r$ and $C(t) + x\Delta\alpha$. In double-ended setups, two reference sections are needed to differentiate between $\gamma/T_r$ and $D_\mathrm{F}(t)$, and between $\gamma/T_r$ and $D_\mathrm{B}(t)$. Only one reference section is needed in single-ended and double-ended setups if the reference temperature varies sufficiently over time. To examine the minimum temperature variation that is needed when using one reference section, the analysis of the example of Section 2.9 is repeated using only the reference section in the ambient water bath, which varies between 12.53 and 12.73 °C. This temperature variation of only 0.2 °C proved to be sufficient for this setup. The contribution of the parameter uncertainty to the standard uncertainty is again small compared to the uncertainty introduced by the noise in the Stokes and anti-Stokes intensity measurements. As expected, the likely bias in the estimated temperature of the ambient bath that was apparent in Figure 2.4 translates to a bias in the estimated temperature (not shown). For example, the temperature estimates along the sections in the cold and warm water baths are 0.03 and 0.10 °C too low, respectively. The minimum temperature difference needed for calibration depends on many factors, including: the matrix solver and its settings, the length of the reference sections, the Stokes and anti-Stokes intensity, and the noise in the Stokes and anti-Stokes intensity measurements.

All existing calibration procedures rely on the temperature of reference sections measured with external sensors. Any deviation of the fiber temperature from the temperature measured with an external sensor introduces errors. Problems that are commonly occurring with DTS calibration are ill-defined positions of the reference sections and non-uniform temperature of the water baths. Both can be discovered at different stages of the calibration procedure. They may introduce a bias in the estimated temperature, which is not accounted for in the estimation of the standard uncertainty and confidence intervals. Therefore, an additional external temperature sensor is recommended for identification of a bias in the reference temperature. A bias may then be identified by, for example, composing a figure of the time-averaged difference between the estimated temperature and the reference temperature, similar to Figure 2.4. A non-uniform temperature of the reference sections also negatively affects the parameter estimation by introducing an error in the coefficient matrix, in the first column of $\mathbf{X}_m$ in Equations 2.30 and 2.37. Investigation of the contribution of the parameter uncertainty to the uncertainty of the estimated temperature is explained in Section 2.9.3. A non-uniform temperature of the reference sections may also result in an overestimation of the noise in the Stokes and anti-Stokes inten-

sity measurements. The variance of the noise in the intensity measurements are estimated from the residuals between Equations 2.20–2.21 and the intensity measurements assuming a uniform reference temperature (Section 2.4). A non-uniform temperature of a reference section increases the residuals, which are incorrectly attributed to the noise from the detector. A comparison of the estimated variance of different reference sections can indicate the location of non-uniform temperature sections. Alternatively, trends in the time-averaged differences between the estimated and reference temperature can also indicate a non-uniform temperature of the reference sections, of which an example is shown with orange markers in Figure 2.4.

## 2.11 Conclusion

A new approach is presented to calibrate temperature from Stokes and anti-Stokes intensity measurements and to provide a confidence interval for the estimated temperature. The uncertainty in the estimated temperature is caused by the noise from the Stokes and anti-Stokes detectors, and the uncertainty in the calibrated parameters that relate the Stokes and anti-Stokes intensity measurements to temperature. Estimation of the confidence interval for the estimated temperature requires an estimation of the distribution of the noise from the Stokes and anti-Stokes detectors and a multi-variate distribution of the parameters that relate the Stokes and anti-Stokes intensity measurements to temperature. All these distributions are propagated with Monte Carlo sampling to approximate the probability density function of the temperature, which is different at each location and varies over time. Various summarizing statistics can be computed from the approximated probability density function, such as standard uncertainties and confidence intervals.

Several improvements were made to existing calibration procedures to reduce the uncertainty in the estimated temperature. The integrated differential attenuation differs per setup and must be experimentally estimated to differentiate it from a shift in temperature. The integrated differential attenuation for double-ended setups is formulated such that it can be used directly in linear regression and the uncertainty in the parameter estimation is reduced. The parameter estimation is further improved by making use of the fact that some parameters are time-invariant, and to use all available data to estimate their value. The linear regression accounts for spatial and temporal variation in the signal intensity, so that large-intensity measurements have a larger weight in the parameter estimation than the small-intensity measurements.

In double-ended setups, the temperature is estimated from measurements made from both ends of the fiber. Close to the ends of the fiber, the difference in Stokes and anti-Stokes intensity between the forward and backward measurements is large, resulting in a large difference in the uncertainty of the temperature estimated from the forward and backward measurements. The estimated temperature is a weighted average of the temperatures estimated from the forward and backward-channel measurements. Compared to unweighted averaging, this reduces the uncertainty in the estimated temperature. The uncertainty of the temperature that is estimated with the proposed calibration procedure is assessed in an example. The estimated temperature and 95% confidence intervals adequately represent the temperature of the reference sections.



The calibration procedure is implemented in "dtscalibration", an open-source Python package that is freely available under the BSD 3-or-later license from `https://github.com/dtscalibration/python-dts-calibration`. The package contains the new calibration procedures for both single-ended and double-ended setups, can compute confidence intervals of the estimated temperature, and includes several routines for visualization of the results.

- Dataset: B. F. des Tombe (2019). *DTS measurements supporting a DTS calibration paper*. Dataset license: GPL-3.0-or-later. DOI: `10.4121/UUID:71B5C3C2-4105-4F4F-BD1E-D7C56732A665`

## 2.12 Acknowledgement

The authors thank Zoltan Perko (Delft University of Technology, the Netherlands) for his help with the calibration procedure and reviewing the manuscript. The comments of Scott Tyler (University of Nevada, Reno, NV) and four anonymous reviewers greatly improved the manuscript. The authors thank Frank Smits and Tom Kind (Waternet, the Netherlands) for hosting the setup of the example. A Python notebook of the example is found as supplement material (Article_S1.pdf and Article_S1.ipynb) at `http://www.mdpi.com/1424-8220/20/8/2235/s1`. This work was funded by the Netherlands Organization for Scientific Research (NWO, the Netherlands) within the program the New Delta, project number 869.15.006.

# 3 Estimating travel time in bank filtration systems from a numerical model based on DTS measurements



**This chapter is based on:** des Tombe, B. F., Bakker, M. , Schaars, F. and van der Made, K. (2018), Estimating Travel Time in Bank Filtration Systems from a Numerical Model Based on DTS Measurements. Groundwater, 56: 288-299. doi:10.1111/gwat.12581

**Abstract.** An approach is presented to determine the seasonal variations in travel time in a bank filtration system using a passive heat tracer test. The temperature in the aquifer varies seasonally because of temperature variations of the infiltrating surface water and at the soil surface. Temperature was measured with distributed temperature sensing (DTS) along fiber optic cables that were inserted vertically into the aquifer with direct push equipment. The approach was applied to a bank filtration system consisting of a sequence of alternating, elongated recharge basins and rows of recovery wells. A SEAWAT model was developed to simulate coupled flow and heat transport. The model of a two-dimensional vertical cross-section is able to simulate the temperature of the water at the well and the measured vertical temperature profiles reasonably well. MODPATH was used to compute flow paths and the travel time distribution. At the study site, temporal variation of the pumping discharge was the dominant factor influencing the travel time distribution. For an equivalent system with a constant pumping rate, variations in the travel time distribution are caused by variations in the temperature-dependent viscosity. As a result, travel times increase in the winter, when a larger fraction of the water travels through the warmer, lower part of the aquifer, and decrease in the summer, when the upper part of the aquifer is warmer.

**Impact statement:** Passive heat tracer experiment with DTS measurements and numerical modeling may be used to estimate travel times in Bank Filtration

Systems.

**Publication history**

| | |
|---|---|
| Manuscript received | 12 December, 2016 |
| Manuscript revised | 07 July, 2017 |
| Manuscript accepted | 12 July, 2017 |
| Version of Record online | 23 August, 2017 |
| Issue Online | 01 March, 2018 |



## 3.1 Introduction

A bank filtration system is a type of Managed Aquifer Recharge system where infiltration of water is induced at the bank of a water body and recovered by wells (e.g., Maliva and Missimer, 2012). It is a cost-effective and sustainable filtration method for the production of potable water (Ray et al., 2003; Huelshoff et al., 2009; Maliva and Missimer, 2012). The travel time during soil passage is a critical design parameter of a bank filtration system and needs to be large enough to result in, for example, pathogen-safe water (Schijven et al., 2003; Toze et al., 2010). Although tracer experiments have been used to determine the travel time from one observation well to another, it is practically very difficult to use them to determine the travel time distribution of a bank filtration system (Zheng et al., 2011; Ma et al., 2012). In this chapter, it is demonstrated how the travel time distribution can be derived from a passive heat tracer experiment. There are a variety of other methods that can be used to determine travel times in subsurface systems, see, e.g., the recent summary by Dreuzy and Ginn (2016).

In recent years, the use of heat as a tracer has increased due to the wide availability of temperature loggers and improved computer codes (Anderson, 2005). The application of Distributed Temperature Sensing (DTS) in hydrology made it possible to measure temperature along long fiber optic cables with a fine spatial resolution in a practical manner (e.g., Selker et al., 2006; Westhoff et al., 2007; Tyler et al., 2009; Steele-Dunne et al., 2010; Becker et al., 2013). Fiber optic cables have been lowered in boreholes to measure temperature variations, for example to determine the terrestrial heat flow (e.g., Hurtig et al., 1993; Förster et al., 1997; Henninges et al., 2005) or local groundwater flow velocities and heat transport (e.g., Read et al., 2013; Coleman et al., 2015). Estimation of aquifer thermal parameters using boreholes depends on the borehole thermal properties and the location of the heat source and temperature sensor within the borehole (Moscoso Lembcke et al., 2015). Alternatively, fiber optic cables may be inserted into unconsolidated aquifers using direct-push equipment, so that no borehole is needed (Bakker et al., 2015).

Two types of heat tracer experiments may be distinguished: active tracer experiments, where the water is actively heated and the response is measured (e.g., Leaf et al., 2012; Wagner et al., 2014b; Bakker et al., 2015), and passive heat tracer experiments, where groundwater temperature changes are caused by natural fluctuations in temperature (see, e.g., Anderson, 2005; Hoehn and Cirpka, 2006; Constantz, 2008; Saar, 2011). Passive heat tracer experiments usually cover a larger area than active heat tracer experiments and are well suited to determine the travel time distribution in bank filtration systems, provided the natural temperature fluctuations are large enough. The temperature of the groundwater in bank filtration systems is influenced by the temperature variations of the infiltrating water and the temperature variations at the soil surface, which may vary significantly throughout the year (e.g., Molina-Giraldo et al., 2011b). Measured temperature profiles may be simulated with numerical models for coupled groundwater flow and heat transport. When such models are used for seasonally varying temperature conditions, they need to include the effect of the temperature of the groundwater on the flow field via the temperature-dependent viscosity.



The main objective of this chapter is to derive the variation in the monthly travel time distribution of water in a bank filtration system from a passive heat tracer experiment using a numerical model and DTS measurements. The temperature variation with depth is measured along vertically inserted fiber optic cables with a DTS system using the procedure developed by Bakker et al. (2015). The measured temperature variations are simulated in a 2D vertical cross-section with the coupled flow and heat transport code SEAWAT (Thorne et al., 2006). The numerical model is used to determine the variation of the monthly travel time distribution of the water. The second objective of this chapter is to determine the effect of variations in viscosity caused by temperature changes on the travel time distribution. The proposed approach is applied to a study site in the Netherlands.

## 3.2 Study site

The study site is located in the dunes on the west coast of the Netherlands (Figure 3.1), where the drinking water company Provinciaal Waterleidingbedrijf Noord-Holland (PWN) operates a bank filtration system that produced 88 million cubic meters of potable water in 2014. In addition to filtration, the system serves as a back-up storage for when no water is available for infiltration, and to level out fluctuations in water quality. The system is also called a “Managed Aquifer Recharge system” or a “Dune Filtration system”. The system is designed

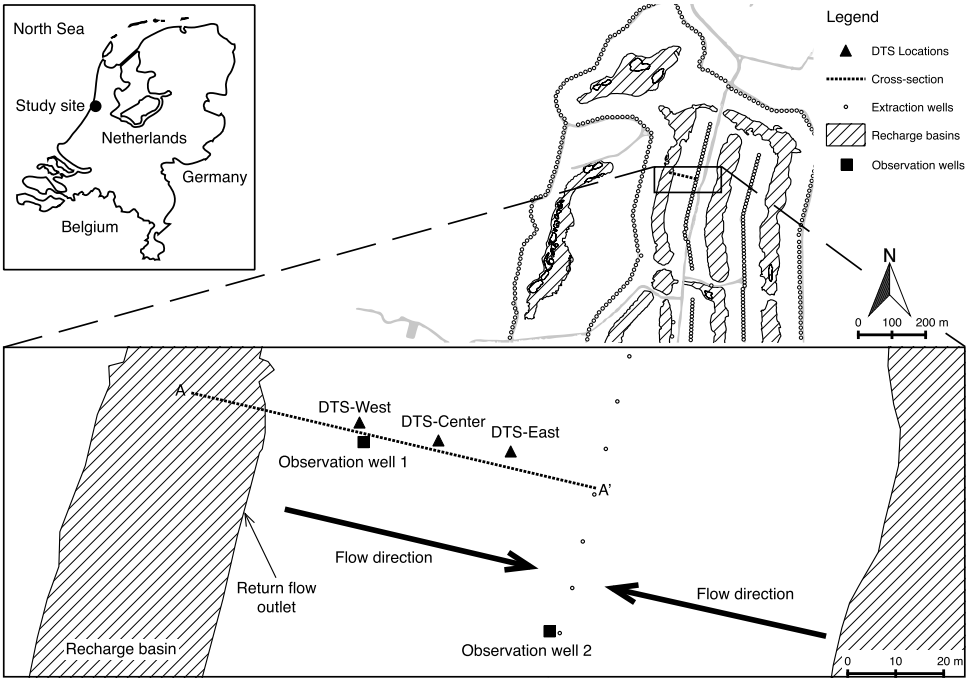


Figure 3.1: Map of the study site. Recharge basins (hatched), extraction wells (circles), DTS locations (triangles), and an observation well (square). The WGS84 coordinates of the center DTS location are (4.6184°, 52.5514°).

such that the travel time in the aquifer is at least 40 days. It consists of 12 parallel elongated shallow recharge basins to infiltrate pre-treated river water and 682 shallow wells to recapture the water. The recharge basins are 20 to 40 meters wide, several hundred meters long, and 1 to 2 meters deep. Rows of wells are located between the basins. The well screens extend from 2.5 meters to 10 meters below surface level. The wells are spaced 10 meters apart and are connected via collection pipes to vacuum pumps with a controllable flow rate. The row of pumping wells is located in the middle between two recharge basins. The distance from the row of wells to either of the two banks is approximately 70 meters (Figure 3.1). Recharge due to precipitation is approximately 1 mm $d^{-1}$. The flow rate (continuously), water temperature (continuously), and water quality (daily) are measured in the pumping station. In case pathogens are detected in the extracted water, wells continue to extract water to clean the system, but the water is routed back to the recharge basin ('Return Flow Outlet' in Figure 3.1), rather than to the treatment plant.

A schematic cross-section along A-A' (Figure 3.1) is shown in Figure 3.2. The aquifer is approximately 36 m thick, is subdivided in three sub-layers, and

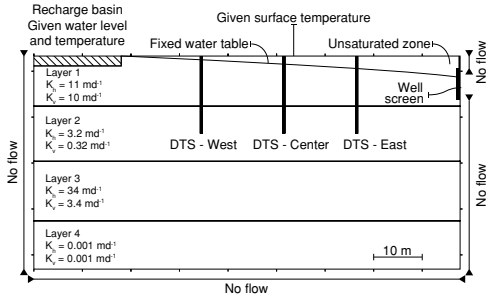


Figure 3.2: Schematic cross-section of the aquifer along A-A' in Figure 3.1, including flow boundaries for water and heat.



is bounded at the bottom by a 10.5 m thick clay layer. The first layer is 10.5 m thick and consists of coarse sand. The second layer is 12.5 m thick and consists of fine sand with thin clay layers. The third layer is 13 m thick and consists of coarse sand. Estimated saturated hydraulic conductivity values are presented in Figure 3.2 (Sander de Haas, PWN, personal communication, October 2014). Fiber optic cables were pushed 15 m into the ground at three locations using direct-push equipment (Bakker et al., 2015) and are labeled West, Center, and East. Fiber optic cables were connected in series using a Fujikura-FSM-70S fusion splicer, resulting in one long cable that was buried underground from the measurement locations to a nearby building with the DTS unit. There are two observation wells near the cross-section. Observation well 1 is located near DTS-West (5.50 m below surface) and Observation well 2 (8.20 m below surface) is located in the gravel pack of a pumping well, three pumping wells (30 m) away from the cross-section (Figure 3.2).

## 3.3 Measurements

The total discharge of the entire row of 45 wells is measured at the pumping station. The pumping rate is averaged per well and divided by 2, as approximately half the water comes from the recharge basin East of the rows of wells. The daily pumping rate (blue) and its three-months moving average (black) are shown in Figure 3.3a. The return flow to the basin, when a pollution is detected in the extracted water, is indicated with the orange fill in Figure 3.3a.

The temperature is measured in Observation wells 1 and 2 and is shown in Figure 3.3b with green and purple lines, respectively. Although Observation well 2 is not located in the studied cross-section A-A', the measured temperature is expected to be representative for the same location in the cross-section, as flow lines are approximately parallel to the cross-section. A temperature sensor was

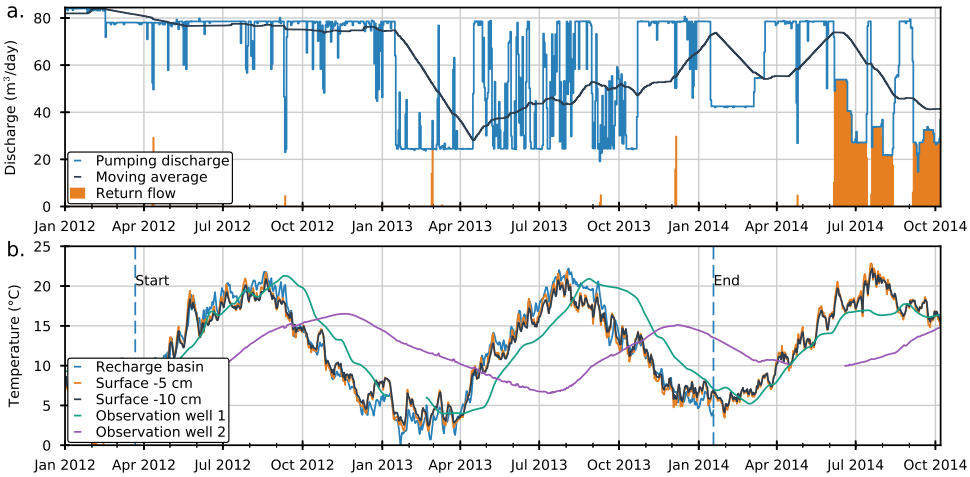


Figure 3.3: a: Discharge of the pumping well (blue) divided by two, its three-month moving average (black), and the discharge returned to the recharge basin upon detection of pollution (orange). b: Temperature of the recharge basin (blue), measured between the 'Start' and 'End' labels, temperature at 5 cm and 10 cm below surface level (orange and black), and temperature in Observation wells 1 and 2 (green and purple).

placed at the bottom of the recharge basin. The last readout was in January 2014, after which the sensor failed. The measured time series is shown with a blue line in Figure 3.3b between 'Start' and 'End'. Temperature measurements at 10 cm below ground surface at weather station De Bilt of the Royal Netherlands Meteorological Institute (located 63 km South East of the study site) show a remarkable resemblance with the available temperature measurements of the recharge basin and were used to fill the missing recharge basin temperature measurements (black line in Figure 3.3b). It is noted that this gap-filling is an approximation and does not take into account, for example, changes in the temperature of the recharge basin caused by the return flow in June, July, and October 2014. Temperature measurements at 5 cm below ground surface from the same weather station were used for the temperature at the ground surface of the study site (orange line in Figure 3.3b). The temperature signal at Observation wells 1 and 2 clearly differ in both the amplitude and the phase from the temperature signal in the recharge basin and at the ground surface.

Temperature profiles were measured along the fiber optic cable on April 24, June 3, August 7, and October 1 of 2014, and were averaged over 24 hours. The Silixa Ultima DTS system (Silixa Ltd., London, UK) was used for the first three measurement dates, providing a 0.13 m sample spacing. The Sensornet Oryx DTS system (Sensornet Ltd., Elstree, Hertfordshire, UK) was used for the measurements in October 2014, with a sample spacing of 1 m. The attenuation along

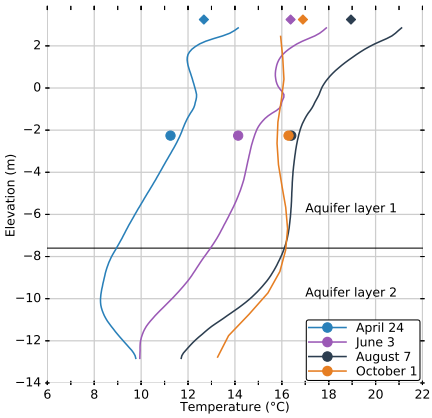


Figure 3.4: Temperature profile measured using DTS in 2014 at DTS-West location (lines), Observation well 1 temperature (dot), surface temperature (diamond).

the cable is corrected for by using the double-ended approach (Giesen et al., 2012) and cold and warm temperature baths were used for calibration. Four temperature profiles measured at location West are shown in Figure 3.4. The temperature at Observation well 1, located next to the DTS-West location, is plotted for validation of the DTS measurements (dots). The measured temperature profiles match the temperature sensor measurements within 1 °C. The surface temperatures at -5 cm, measured at the weather station, are shown with diamonds. These are significantly lower than the DTS measurements, (up to 2 °C in August), except for October, when the -5 cm surface temperature is higher than the DTS measurement.

The vertical temperature profiles in the aquifer vary throughout the year. In April, the coolest water is present at ~ -10 m, while the water is warmer above and below this depth. In June and August, the temperature decreases almost monotonically with depth, while in October the temperature increases with depth till ~ -8 m after which it decreases. The largest temperature fluctuations are observed at the surface (7 °C over the measurement period), while the temperature fluctuations at ~ -13 m (layer 2, which has lower permeability) is only half the fluctuation at the surface (3.5 °C). In April, June and August the vertical temperature gradient near the surface indicates that heat is transported via conduction from the surface into the aquifer, while the reverse happens in October.

## 3.4 Mathematical model

Heat transport in porous media is governed by thermal advection and thermal conduction. The heat transport equation may be written in a form analogous to the solute transport equation as (e.g., Thorne et al., 2006),

$$\frac{\partial T}{\partial t} = \nabla \left( [D^* + \mathbf{D}] \, \nabla T \right) - \frac{1}{R} \nabla \left( \mathbf{u} \, T \right), \tag{3.1}$$



where $T$ is temperature [$\Theta$], $t$ is time [T], $\mathbf{u}$ is the groundwater velocity vector $\left[\mathrm{LT^{-1}}\right]$, $D^*$ is the thermal diffusivity $\left[\mathrm{L^2T^{-1}}\right]$, $\mathbf{D}$ is the dispersion tensor $\left[\mathrm{L^2T^{-1}}\right]$, and $R$ is the thermal retardation [-]. The latter three are related to the soil properties as,

$$D^* = \frac{k_\mathrm{b}}{\rho_\mathrm{b} c_\mathrm{b}}, \quad \mathbf{D} = \alpha \frac{\mathbf{u}}{R}, \quad R = \frac{\rho_\mathrm{b} c_\mathrm{b}}{\theta_\mathrm{w} \rho_\mathrm{w} c_\mathrm{w}}, \tag{3.2}$$

where $\rho_\mathrm{b}$ and $\rho_\mathrm{w}$ are the density of the bulk and water, respectively $\left[\mathrm{ML^{-3}}\right]$, $\theta_\mathrm{w}$ is the water content [-], $c_\mathrm{b}$ and $c_\mathrm{w}$ are the specific heat capacity of the bulk and water, respectively $\left[\mathrm{L^2T^{-2}\Theta^{-1}}\right]$, $k_\mathrm{b}$ is the isotropic bulk thermal conductivity $\left[\mathrm{LMT^{-3}\Theta^{-1}}\right]$, and $\alpha$ is the dispersivity tensor [L] with principal components $\alpha_\mathrm{L}$ (longitudinal) and $\alpha_\mathrm{T}$ (transverse). The water, solids, and air fractions are approximated as a single effective-medium of which the temperature is at instantaneous equilibrium.

The bulk density and bulk thermal capacity are calculated by the volume-weighted average of the properties of the moisture, air and solids fractions (Nield and Bejan, 2006),

$$\rho_\mathrm{b} c_\mathrm{b} = \theta_\mathrm{s} \rho_\mathrm{s} c_\mathrm{s} + \theta_\mathrm{w} \rho_\mathrm{w} c_\mathrm{w} + \theta_\mathrm{a} \rho_\mathrm{a} c_\mathrm{a} \tag{3.3}$$

where $\theta_\mathrm{s}$ and $\theta_\mathrm{a}$ are the volumetric fractions of the solids and air, respectively [-], $\rho_\mathrm{s}$ and $\rho_\mathrm{a}$ are the density of the solids and air, respectively $\left[\mathrm{ML^{-3}}\right]$, and $c_\mathrm{s}$ and $c_\mathrm{a}$ are the specific heat capacity of the solids and air, respectively $\left[\mathrm{L^2T^{-2}\Theta^{-1}}\right]$.

The bulk thermal conductivity depends on the pore structure (Nield and Bejan, 2006; Wang and Pan, 2008). Many averaging schemes exist, which either approximate the pore structure (e.g., series, parallel, EMI (Bruggeman, 1935), Maxwell / Hashin & Shtrikman (Hashin and Shtrikman, 1962)) or use empirical relations (e.g., Johansen, 1977; Campbell, 1985). Estimates for unsaturated soils are more difficult because of the large difference in thermal conductivity between the air and solid phase (Johansen, 1977). The volume-weighted geometric mean is used here, which is suggested as a reasonable estimate (Johansen, 1977; Nield and Bejan, 2006),

$$k_\mathrm{b} = k_\mathrm{s}^{\theta_\mathrm{s}} k_\mathrm{w}^{\theta_\mathrm{w}} k_\mathrm{a}^{\theta_\mathrm{a}}, \tag{3.4}$$

where $k_s$, $k_w$, $k_a$ are the thermal conductances for solids, water, and air, respectively.

Groundwater flow is influenced by the temperature via viscosity and density. The hydraulic conductivity is defined as,

$$K_{sat} = \frac{\kappa \rho_w g}{\mu}, \tag{3.5}$$

where $K_{sat}$ is the saturated hydraulic conductivity $\left[LT^{-1}\right]$, $\kappa$ is the intrinsic permeability $\left[L^2\right]$, $\mu$ is the dynamic viscosity $\left[ML^{-1}T^{-1}\right]$, and $g$ is the gravitational acceleration $\left[LT^{-2}\right]$. The relations between density and temperature (Langevin et al., 2007, Eq. 14) and dynamic viscosity and temperature (Langevin et al., 2007, Eq. 19) are approximated by,

$$\rho_w(T) = 999.1 - 0.1125 \cdot (T - 12), \tag{3.6}$$

$$\mu(T) = 10^{-3} \cdot \left[1 + 1.55 \cdot 10^{-2} \cdot (T - 20)\right]^{-1.572}, \tag{3.7}$$

where $\rho_w$ is in kg m$^{-3}$, $\mu$ is in kg m$^{-1}$ s$^{-1}$, and $T$ is in °C. The groundwater temperature at the study site varies roughly between 4 and 20 °C. The corresponding variation in the water density is only 0.18 %, but the viscosity varies with 36 %, which results in a 57 % higher hydraulic conductivity for water of 20 °C than for water of 4 °C.

The hydraulic conductivity, thermal conductivity and heat capacity depend on the moisture content, each of which is lower in the unsaturated zone. This needs to be accounted for when modeling temperature signals in bank filtration systems (Molina-Giraldo et al., 2011b). When vertical flow through the unsaturated zone is neglected, the moisture content above the water table may be calculated as (Genuchten, 1980),

$$S_e(h) = \frac{\theta_w(h) - \theta_{w,r}}{n - \theta_{w,r}} = \left[\frac{1}{1 + (\beta h)^{1/(2-m)}}\right]^m, \tag{3.8}$$

where $S_e$ is the effective saturation [-], $\theta_w$ is the water content [-], $\theta_{w,r}$ is the residual soil-water content [-], $n$ is the porosity [-], $h$ is the height above the water table (cm), and $\beta$ $(\text{cm}^{-1})$ and $m$ (-) are soil-specific parameters. Values for medium grain-sized sand are used $\beta = 0.035\,\text{cm}^{-1}$, m = 0.67 (Tuller and Or, 2005). The hydraulic conductivity in the unsaturated zone is calculated with the van Genuchten equation (1980),

$$K_{unsat} = K_{sat}\sqrt{S_e}\left[1 - \left(1 - S_e^{1/m}\right)^m\right]^2 \tag{3.9}$$

## 3.5 Boundary conditions

Two dimensional groundwater flow and heat transport (Equation 3.1) are simulated in a vertical cross-section (Figure 3.2) that is 10 m wide (the distance between two pumping wells). Total net precipitation on cross-section A-A' is ~1% of the mean pumping rate and is neglected. Flow in the direction normal to the cross-section is neglected, including near the pumping well. Two rows of wells are positioned at an equal distance from each recharge basin (Figure 3.1), so that the vertical axis at the center of the recharge basin can be modeled as a no-flow boundary for water and heat. Two recharge basins are located at an approximately equal distance from the row of wells, so that the vertical boundary above and below the well screen can be modeled as a no-flow boundary for water and heat. The row of wells is modeled as a vertical line-sink with given uniform extraction rate. As stated, radial flow in the horizontal plane near the well is neglected. Vertical flow of water and heat at the bottom of the clay layer is neglected (no-flow boundary). The head and temperature are specified for the cells representing the recharge basin. The water level in the recharge basin is fixed to 2.92 m above mean sea level and the resistance of the leaky bed at the bottom of the recharge basin is set to 1 day. The top boundary is a no-flow for groundwater and given temperature for heat transport. Estimates of the conductive and advective heat fluxes in the system are presented in Appendix C, which shows that vertical advective heat transport is small compared to vertical conductive heat transport and horizontal advective heat transport. Vertical advective heat transport together with recharge is neglected at the top boundary.

## 3.6 Model description

The coupled differential equations for the flow of heat and water are solved with the finite difference code SEAWAT (Langevin et al., 2007). Flow and heat transport are solved iteratively using the generalized conjugate gradient solver, where the thermal conduction is solved with an implicit finite difference scheme and the thermal convection is solved using a third-order total-variation-diminishing scheme with a stability constraint (Zheng and Wang, 1999). The input files for SEAWAT were written and the output files were read using the open-source Python package FloPy (Bakker et al., 2016) in Jupyter notebooks.

The modeled cross-section is 46 m deep, 88 m long and 10 m wide. The cross-section is discretized vertically into 107 model layers, with cells of 7.5 cm high near the surface (to account for the large temperature gradients) increasing to 1 m high for the lower part of the model. The cross-section is discretized horizontally into 88 columns of 1 m long. The modeling period is from 2012 to 2014,

Table 3.1: Hydraulic and thermal aquifer properties

| | | |
|---|---|---|
| $\rho_s$ | Density of the solids | 2710 kg m$^{-3}$ |
| $\rho_w$ | Density of the water (at 12 °C) | 999.1 kg m$^{-3}$ |
| $\rho_a$ | Density of the air | 1.2 kg m$^{-3}$ |
| $c_s$ | Specific heat capacity of solids | 835 J kg$^{-1}$ °C$^{-1}$ |
| $c_w$ | Specific heat capacity of water | 4183 J kg$^{-1}$ °C$^{-1}$ |
| $c_a$ | Specific heat capacity of air | 1005 J kg$^{-1}$ °C$^{-1}$ |
| $k_s$ | Thermal conductivity of solids | 4.85 W m$^{-1}$ °C$^{-1}$ |
| $k_w$ | Thermal conductivity of water | 0.58 W m$^{-1}$ °C$^{-1}$ |
| $k_a$ | Thermal conductivity of air | 0.0257 W m$^{-1}$ °C$^{-1}$ |
| $n$ | Porosity | 0.35 |
| $S_s$ | Storage coefficient | $10^{-5}$ m$^{-1}$ |
| $S_y$ | Specific yield | 0.25 |
| $\alpha_L$ | Longitudinal dispersivity | 0.1 m |
| $\alpha_T$ | Transversal dispersivity | 0.01 m |



with a spin-up period starting in 1988. All boundary conditions are specified on a daily basis and each day is split into 10 calculation steps to comply with the convergence criteria. The flow is modeled as transient, with the specific yield set to 0.25 for unsaturated cells and the storage coefficient for saturated cells set to $10^{-5}$ m$^{-1}$. Values for the aquifer properties used in the SEAWAT model are presented in Table 3.1 and Figure 3.2. The recharge basin is modeled using the River package and the well using the Well package in SEAWAT.

No unsaturated packages currently exist for SEAWAT. Therefore, an approximate approach is used to model flow and heat transport through the unsaturated zone. First the water table is calculated by averaging the head in the top cells of the last year of the spin-up period. Then the water table is used to calculate the thermal capacity, the thermal conductance, and the hydraulic conductivity in the unsaturated zone at reference temperature using Equations 3.3, 3.4, and 3.9, respectively.

The spin-up period starts in 1988 with a uniform temperature of 12 °C and a water table equal to the surface elevation. A yearly sine function is used for the temperature of the recharge basin and at the soil surface during spin-up (based on available temperature measurements). A constant discharge was of 60 m$^3$d$^{-1}$ is used during spin-up (average of the period 2010-2014). The spin-up period is split in two parts. In the first part, 1988-2007, the top of the model is horizontal and no unsaturated zone is modeled. The head in the top cells is averaged over the year 2007 and is used to compute the average position of the water table and to calculate unsaturated zone properties for the second part of the spin-up period from 2008-2011.

No formal calibration is conducted, for example using a parameter estimation package such as PEST (Doherty, 2016), because the temperature of the recharge basin and at the surface were not measured correctly during the entire experiment. Although reasonable substitutes are obtained (see Figure 3.3), it makes formal calibration an exercise on how aquifer and heat transport parameters can take on surrogate roles to compensate for errors in the input series.



The travel time of a water particle from the recharge basin to the extraction well is computed with MODPATH (Pollock, 2012). MODPATH uses a continuous velocity field by linearly interpolating the velocities across cell boundaries calculated with SEAWAT. The porosity (Table 3.1) is used to calculate an average pore flow velocity. The cumulative flux along the cell faces representing the well screen is computed at the desired arrival time. One thousand particles are spaced such that each particle represents 0.1% of the extracted volume. The particles are released and tracked backward in time until they reach the recharge basin to compute the travel time for each of the one thousand particles.

## 3.7 Model results

The measured temperature in Observation well 1 (blue) and Observation well 2 (orange) and their corresponding modeled temperatures (black and purple, respectively) are shown in Figure 3.5. The root-mean-square error (RMSE) between modeled and measured temperatures is 1.28 °C at Observation well 1 and 0.72 °C at Observation well 2. The amplitudes of the modeled temperature variations are in accordance with the amplitudes of the measured temperatures, with the largest differences for Observation well 1 in the winter months. The phase-shift and the timing of the modeled temperature peaks coincide with the measurements. The RMSE between the modeled and measured heads at Observation well 1 is 0.49 m (not shown). Comparison of the modeled heads to measured heads at Observation well 2 is not meaningful, as radial flow in the horizontal direction is neglected.

Temperature measurements (blue) at the three DTS locations for the four measurement dates are compared to model results (orange) in Figure 3.6. The fixed water table is shown with the dashed line. The measured and simulated temperature profiles show similar behavior but also distinct differences. The RMSE between the modeled and measured temperature profiles is 1.81 °C. The lowest RMSE of (1.21 °C) is calculated for location East in October and the highest RMSE of (2.20 °C) is calculated for location West in June. The temperature transition from the approximate water table to the surface is visible in both the modeled and the measured temperature profiles. The bends in the temperature

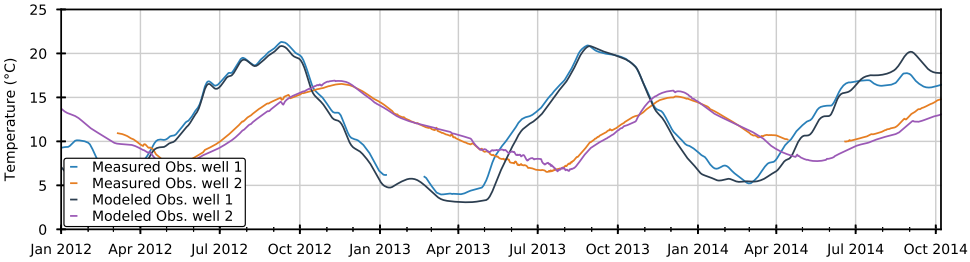


Figure 3.5: Measured and modeled temperature at Observation well 1 and 2



profiles just above the water table are matching well for April and October, 2014. The bend in the temperature profile of June 2014 is located higher in the model as compared to the measurement. At that time the actual water table is probably lower compared to other months due to high pumping rates, so that the bend in the measurements is at a lower elevation than in the model. In August, the specified temperature at the surface is 2 °C lower than the surface temperature measured with DTS (Figure 3.4), resulting in an offset between measured and simulated temperature in the upper part of the temperature profiles in August. Furthermore, a bend is missing in the upper half of the August measurement at location West. This is likely due to the effects of the return flow (orange fill in Figure 3.3), when all of the cold extracted water in June and July was returned to the recharge basin. These effects are not accounted for in the specified temperature of the recharge basin.

The travel time of the extracted water was calculated for each month between November 2013 and October 2014 and is shown in Figure 3.7. Note that the travel time, plotted on the vertical axis, is on log-scale. The color of the line represents the travel time for which xx% of the flow is faster and is referred to as the $t_{xx\%}$ line. The gray-level of the fill represents the maximum depth reached by a water particle: the light-gray fill represents water particles that only moved through the first aquifer layer, the medium-gray fill represents water particles that reached the second aquifer layer, and the dark-gray fill represents water particles that reached the third aquifer layer. Water particles that reach the third aquifer layer take at least 500 days to travel from the recharge basin to the extraction well. The bottom graph shows the corresponding monthly discharge of the pumping well. The $t_{50\%}$ line varies significantly from month to month and is strongly related to the pumping discharge (when the discharge is high, $t_{50\%}$ is low). The shortest travel times are less than 40 days and occur in the months with the highest discharge.

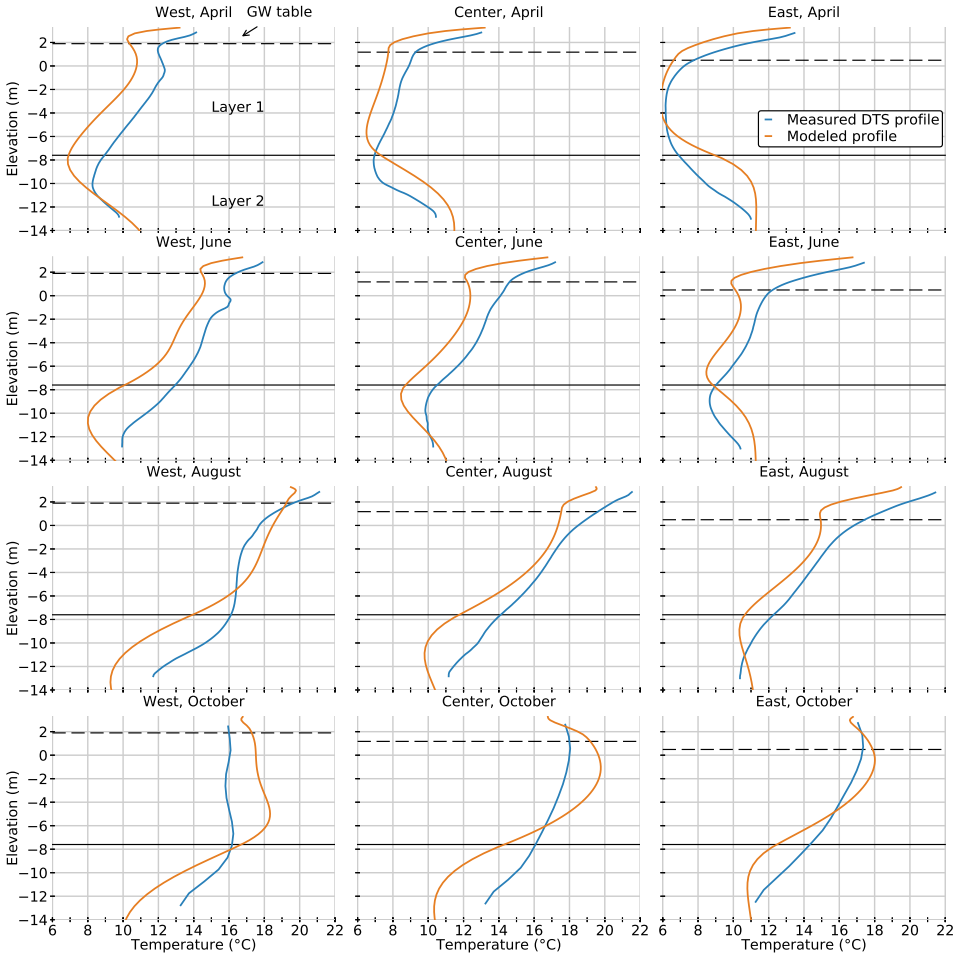


Figure 3.6: Measured DTS temperature (blue) and modeled temperature (orange), fixed water table in model (black dashed line), and interface between aquifer layer 1 and aquifer layer 2 (black solid line).

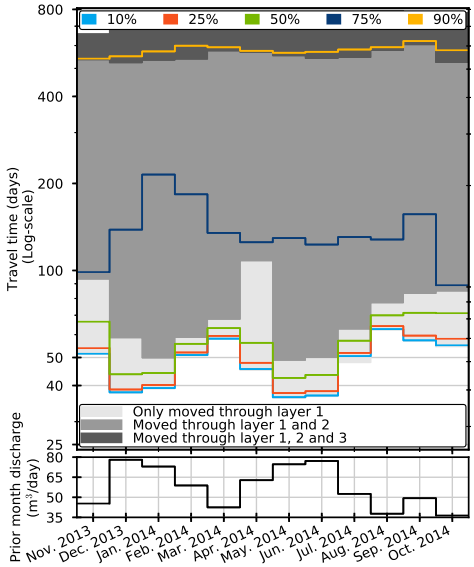


Figure 3.7: Upper: travel time distribution per month. The distribution of the travel time is plotted with the colored lines. Note that the vertical axis is log-scaled. Lower: monthly average discharge of the prior month.

## 3.8 Travel time variation under constant pumping

An additional simulation was performed with a constant discharge and a sinusoidal variation of the temperature in the recharge basin and at the surface to isolate the effect of a seasonal temperature variation on the flow. An illustrative figure of the approximate instantaneous streamlines is shown in Figure 3.8; the discharge is the same between any two adjacent streamlines. The largest fraction of the water flows through the first aquifer layer. The placement of the recharge basin at the top of the aquifer and the extraction well near the top of the aquifer result in curvature of the groundwater streamlines and pathlines. The flow velocities in the second aquifer layer are low, with a vertical velocity component pointing downward at DTS-West and upwards at DTS-East.

The variation of the travel time from month to month at the study site is strongly affected by the variation in the discharge of the wells (Figure 3.7). The effect of seasonal temperature variations on the travel time distribution in the simulation with a constant discharge and a sinusoidal variation of the temperature in the recharge basin and at the surface is shown in Figure 3.9. The figure contains two sets of lines. The dashed lines include solely the effects of varying density, while the continuous lines include both the effect of varying density and viscosity. The influence of density variations on the travel time distribution is negligible, as stated, resulting in virtually the same travel times for each month.

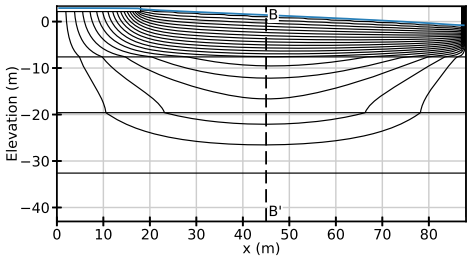


Figure 3.8: Modeled instantaneous streamlines in the vertical cross-section at the study site

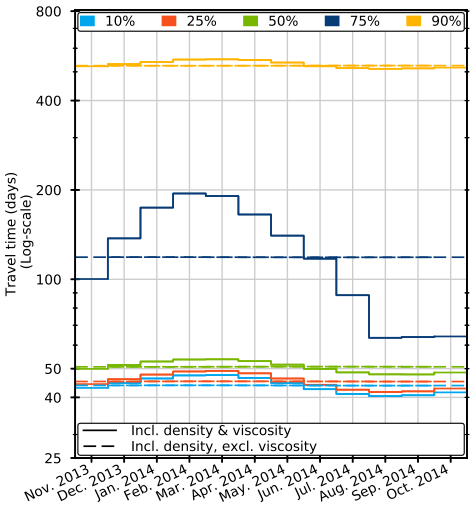


Figure 3.9: Travel time distribution with constant discharge and a sinusoidal surface and recharge basin temperature

The influence of a varying viscosity on the travel time distribution is significant. For constant viscosity, the $t_{10\%}$ is constant and equal to 45 days throughout the year, while a varying viscosity results in a variation from 42 days in the warmest period (August) to 49 days in the coldest period (February). The $t_{75\%}$ line shows a much larger range, varying from 64 to 195 days, while the travel time for constant viscosity is 119 days.

The cumulative flow is computed in the aquifer at section B-B' (Figure 3.8) and is shown in Figure 3.10. In February, 30% of the water flows through the second and third aquifer layer, while it is 24% (so 20% less) in August. Water that travels via the second and third aquifer layer moves a lot slower, as can be seen from the distance between the streamlines shown in Figure 3.8. This seasonal difference results in the large variation of the $t_{75\%}$ line in Figure 3.9.

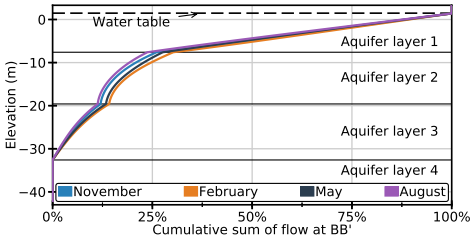


Figure 3.10: The modeled cumulative sum of the flow along section B-B' (Figure 3.8) under constant pumping, on the 15$^{th}$ of the month.



## 3.9 Discussion

Temperature measurements of the water in the recharge basin and at the soil surface are essential for the simulation of flow and heat transport in the system. These measurements were not available for the period of the experiment at the study site. Surface temperatures from weather station De Bilt were used as reasonable substitutes. Aquifer parameters at the study site have been studied for several decades by the drinking water company that operates the bank filtration system, so that reasonable estimates were available.

A separate model was constructed to determine the importance of heat conduction from the top boundary. The top model boundary for heat flow was simulated as isolating instead of a given temperature. This model showed a similar temperature response at Observation well 2 as the model with a given temperature along the top boundary, but the vertical temperature profiles differed significantly near the top of the model, where they are normal to the isolating top boundary. Travel time distributions were also calculated for this modified model and did not differ much from the scenario with a given surface temperature.

The temperature boundary at the bottom is approximated with an isolating boundary. If this boundary is deep enough, the temperature variation along the bottom should be negligible. The maximum temperature variation over 2013-2014 is 0.34 °C at the bottom of the model below the recharge basin, 0.27 °C in the center of the bottom and 0.06 °C at the bottom below the well. These variations are small compared to the temperature variation at the surface, which means that the placement of the bottom boundary is deep enough.

Radial flow in the horizontal plane near the well is neglected. The consequences of this approximation are estimated by calculating the travel time in a 1D situation and comparing it to the travel time in a 2D horizontal situation. The travel time is at most 2.6% shorter when modeled as 2D flow than when modeled as 1D flow but ~15% of the flow has significantly larger travel times.

This means that neglecting radial flow is reasonable when estimating the shortest travel time but less reasonable when estimating the largest travel times. This is in line with the primary interest of the drinking water company, which is the fastest few percent of the flow.



## 3.10 Conclusions

A passive heat tracer experiment was conducted at a bank filtration system to estimate seasonal variations in the travel time distribution. The bank filtration system consists of recharge basins and rows of recovery wells. The temperature in the system varies throughout the year because of temperature variations of the recharge basin and at the surface. The temperature was measured at two observation wells regular temperature sensors. The temperature was also measured at three locations along vertically installed fiber optic cables using Distributed Temperature Sensing (DTS). The main advantages of the latter method are that the fiber optic cables are in direct contact with the aquifer and are able to measure the temperature distribution along vertical lines in the aquifer.

A coupled flow and heat transport model was constructed with SEAWAT. As the model is able to simulate the measured temperature profiles and the measured temperature in the two observation wells, it can be used to compute the travel time distribution from the recharge basin to the wells. The discharge of the pumping wells varies significantly at the study site, which strongly affects the shortest travel times and overshadows the effect of temperature changes on the travel time distribution. The influence of seasonal temperature variations on the travel time distribution was examined by simulating flow in the system with a constant pumping discharge and approximating the temperature of the recharge basin and at the surface with a sinusoidal function with a period of 1 year. This model showed that viscosity changes caused by temperature changes resulted in a significant temporal variation of the travel time distribution. Arrival of the fastest 10% of the water varied between 42 and 49 days. In the winter, a larger portion of the water flows through the deeper, less permeable aquifer layer, when the water in that layer is warmer as compared to the water in the top aquifer layer. As a result, arrival of the fastest 75% of the water varied between 64 and 195 days.

In conclusion, a passive heat tracer experiment consisting of DTS measurements of temperature along vertically installed fiber optic cables combined with numerical modeling of flow and heat transport is a promising approach to estimate travel time distributions in bank filtration systems. Seasonally varying

viscosity needs to be taken into account in the design of the maximum pumping rate for bank filtration systems, especially when the pumping discharge is relatively constant. Operators need to be aware that the risk of pathogen contamination may increase in the summer months because of shorter travel times, which may warrant lower pumping rates.

## 3.11 Acknowledgements



This work was funded in part by the Netherlands Organization for Scientific Research (NWO), program The New Delta with project number 869.15.006. The authors thank Sander de Haas, Ed Rasenberg, and Lucas Borst for hosting the study site at PWN, Ruben Caljé (Artesia, NL) for his assistance with the DTS equipment and analyzing the temperature measurements, and Koen Hilgersom (TU Delft, NL) for assistance with the splicing of the fiber optic cables. The constructive suggestions of the Associate Editor, Grant Ferguson, and two anonymous reviewers helped improve this chapter.

# 4 Estimation of the variation in specific discharge over large depth using DTS measurements of the heat pulse response



**This chapter is based on:** des Tombe, B. F., Bakker, M.,Smits, F., Schaars, F., & Van Der Made, K.-J. (2019). Estimation of the variation in specific discharge over large depth using Distributed Temperature Sensing (DTS) measurements of the heat pulse response. Water Resources Research, 55, 811–826. https://doi.org/10.1029/2018WR024171.

**Abstract.** An approach is presented to determine groundwater flow in unconsolidated aquifers with a heat pulse response test using a heating cable and a fiber-optic cable. The cables are installed together using direct push so that the cables are in direct contact with the aquifer. The temperature response is measured for multiple days along the fiber-optic cable with Distributed Temperature Sensing (DTS). The new approach fits a two-dimensional analytical solution to the temperature measurements, so that the specific discharge can be estimated without knowledge of the position of the fiber-optic cable relative to the heating cable. Two case studies are presented. The first case study is at a managed aquifer recharge system where fiber-optic cables are inserted 15 m deep at various locations to test the fitting procedure. Similar and relatively large specific discharges are found at the different locations with little vertical variation (0.4–0.6 m/d). The second case study is at a polder, where the water level is maintained 2 m below the surrounding lakes, resulting in significant groundwater flow. The heating and fiber-optic cables are inserted to a depth of 45 m. The specific discharge varies 0.07–0.1 m/d and is significantly larger in a thin layer at 30 m depth. It is shown with numerical experiments that the estimated specific discharge is smoother than in reality due to vertical conduction, but the peak specific discharge is estimated correctly for layers thicker than ∼1.5 m.

**Key points**

- A fiber-optic cable and a heating cable are inserted together using direct push
- The variation of groundwater flow perpendicular to the cables is estimated from a heat pulse response test
- Magnitude of the flow is determined without knowledge of the relative position of the two cables

**Publication history**

| | |
|---|---|
| Received | 27 September, 2018 |
| Accepted | 21 December, 2018 |
| Accepted article online | 3 January, 2019 |
| Published online | 30 January, 2019 |



## 4.1 Introduction

The calibration of groundwater models requires measurements of both head and flow. While head can be measured directly, flow can only be measured either when it enters or exits the aquifer (e.g., wells, seepage meters, river discharge), or indirectly with tracers (e.g., solutes, heat) or a variety of geophysical techniques. In this chapter, the specific discharge is estimated from a heat pulse response test using a heating cable and a fiber-optic cable that are installed together with direct-push equipment to a depth of tens of meters. The temperature response is measured along the fiber-optic cable with Distributed Temperature Sensing (DTS) from which the specific discharge is estimated without knowledge of the position of the fiber-optic cable relative to the heating cable.

The use of heat as a tracer has increased over the past decades (e.g., Anderson, 2005; Saar, 2011). Pioneering work on the use of heat as a tracer started in the 1960s with determining groundwater recharge from annual temperature fluctuations at the surface (Suzuki, 1960; Stallman, 1965; Bredehoeft and Papaopulos, 1965), which was extended to the basin scale by Cartwright (1970) and Domenico and Palciauskas (1973). Somogyvári and Bayer (2017) applied inversion algorithms from seismic tomography to a thermal tracer test to reveal aquifer features between two shallow wells. In the 1990s probes were developed with a needle-like heater and thermocouple to determine thermal properties of soil samples (e.g., Ren et al., 1999). Later on, these probes were used to estimate groundwater flow (e.g., Ren et al., 2000; Greswell et al., 2009; Banks et al., 2018). The exact distance between the heater and thermocouple proved to be a large source for errors (Kluitenberg et al., 1995; Greswell et al., 2009), which limits

its practical use to small scale measurements. Thermal response tests were also used in other fields, for example, to measure wind speeds (Sayde et al., 2015).

Groundwater flow can also be estimated from characteristic thermal signatures on a borehole temperature log using naturally occurring temperature gradients (e.g., Trainer, 1968; Drury et al., 1984; Reiter, 2001). The use of DTS adds great detail to thermal response measurements in boreholes; a review of several applications is given in Bense et al. (2016). Layering of the subsurface can be characterized when the borehole is heated (e.g., Leaf et al., 2012). Fractures in bedrock can be identified by temporary sealing parts of the borehole (e.g., Coleman et al., 2015). Read et al. (2014) actively heated a fiber-optic cable to estimate the vertical flow in a well. Thermal response tests are also regularly applied in the field of geothermal energy to quantify the horizontal groundwater flow, which significantly affects the performance of geothermal systems (Chiasson et al., 2000). The performance of ground-coupled heat pumps can be assessed in aquifers with significant groundwater flow by idealizing the borehole as infinitely thin and neglecting vertical heat transfer (e.g., Diao et al., 2004; Wagner et al., 2013; Wagner et al., 2014a). The findings of Diao et al. (2004) were used by Selker and Selker (2018), who presented a method to estimate the vertical variation in the horizontal specific discharge from the thermal response measured in a grouted borehole.



The use of a heating cable in a borehole introduces four additional challenges when estimating groundwater flow. First, large temperature gradients in a borehole may result in vertical flow in the borehole (e.g., Drury et al., 1984). Second, permeable layers are cross-connected vertically via open boreholes and filter beds (e.g., Pehme et al., 2007b; Pehme et al., 2010; Coleman et al., 2015). Third, the filter and the filter pack affect the horizontal streamlines (Drost et al., 1968). Fourth, the exact positions of the heating cable and temperature sensors in the borehole are difficult to determine at depth, while they greatly influence the estimates of the thermal properties (Moscoso Lembcke et al., 2015).

The use of boreholes may be avoided in unconsolidated aquifers by installing fiber-optic and heating cables with direct push (Bakker et al., 2015), where it is assumed that the installation does not disturb the flow field. A thermal response can be measured accurately along the fiber-optic cables with DTS. Bakker et al. (2015) performed two tests in relatively homogeneous dune sand of a managed aquifer recharge system where the specific discharge was relatively large ($0.5\ \mathrm{md}^{-1}$). In the first test, the magnitude of the specific discharge was determined up to 20 m depth from a heat pulse response test where a heating cable and a fiber-optic cable were installed together. The heating and fiber-optic cables were taped together, but they twisted around each other during installation.

As a result, the position of the fiber-optic cable relative to the heating cable in the subsurface was unknown, which significantly affected the measured temperature increase during heating, even when the centers of the two cables were just 1 cm apart (see Figure 4.1a). As a result, only the measured temperature decrease during cooling (after the heating cable is turned off) was used to determine the specific discharge. In the second test, Bakker et al. (2015) determined both the magnitude and the direction of the specific discharge from 5 additional fiber-optic cables that were installed around the heating cable at distances of 1–2 m. The exact positions of the fiber-optic cables relative to the heating cable were known at the surface, but unknown at depth as installation of the cables with direct push gives small deviations from the vertical that were not measured.



The objective of this chapter is to determine the magnitude of the specific discharge from a heat pulse response test with one heating cable and one fiber-optic cable, like the first test in Bakker et al. (2015). First, a new approach is presented to determine the specific discharge from the temperature measurements during both heating and cooling when the position of the fiber-optic cable relative to the heating cable is unknown. This approach is tested in Case Study I, which uses the data of the heat pulse response test presented in Bakker et al. (2015). The range of applicability of the approach was explored by carrying out Case Study II, where the fiber-optic and heating cables were installed much deeper (up to 45 m), the specific discharge was much smaller, and was expected to have a larger variation with depth. Finally, three aspects affecting the accuracy of the proposed method on the estimated specific discharge are explored: vertical conductive heat transfer, hydrodynamic dispersion, and heterogeneity in horizontal layers.

## 4.2 Mathematical formulation

Consider combined groundwater flow and heat transfer in a horizontally infinite aquifer. The aquifer is discretized vertically in many horizontal layers. Water and heat are approximated to move only within a layer; vertical transfer between layers is neglected (but is considered in the Discussion section). Each layer is homogeneous, with a steady state uniform groundwater flow aligned with the $x$-axis. Viscosity and density effects, if any, are neglected. The temperature of both the water and the solids is approximated to be at instantaneous equilibrium. The temperature distribution in a layer is governed by (e.g., Smith and Chapman, 1983; Hopmans et al., 2002; Rau et al., 2012)

$$D_x \frac{\partial^2 T}{\partial x^2} + D_y \frac{\partial^2 T}{\partial y^2} - q \frac{\rho_w c_w}{\rho c} \frac{\partial T}{\partial x} = \frac{\partial T}{\partial t} \tag{4.1}$$

where $T$ [$\Theta$] is the temperature in the aquifer, $x$ and $y$ [L] are the horizontal coordinates, $t$ [T] is time, $D_x$ and $D_y$ [$L^2T^{-1}$] are the thermal dispersion coefficients in the $x$ and $y$ directions, respectively, $q$ [$LT^{-1}$] is the specific discharge in the $x$-direction, and $\rho c$ and $\rho_w c_w$ [$ML^{-1}T^{-2}\Theta^{-1}$] are the volumetric heat capacity of saturated soil and water, respectively. All parameters are constants that do not vary in space and time, such that the differential equation (Equation 4.1) is linear and solutions can be superimposed. The thermal dispersion coefficients consist of a thermal conduction term and a term that accounts for the effect of hydrodynamic dispersion in the water phase (e.g., Marsily, 1986; Rau et al., 2012)



$$D_x = \frac{\kappa}{\rho c} + \beta_x q \frac{\rho_w c_w}{\rho c} \tag{4.2}$$

$$D_y = \frac{\kappa}{\rho c} + \beta_y q \frac{\rho_w c_w}{\rho c} \tag{4.3}$$

where $\kappa$ [$L^2MT^{-3}$] is the isotropic bulk thermal conductivity, and $\beta_x$ and $\beta_y$ [L] are the longitudinal and transverse thermal dispersivities, respectively, which are of the same order of magnitude as the solute transport dispersivities (Marsily, 1986; Hopmans et al., 2002).

A vertical heating cable acts as a vertical line source located at the origin of the coordinate system. The cable produces a constant amount of heat per unit length $p$ [$MLT^{-3}$] when turned on at time $t = 0$. The temperature is measured with respect to the background temperature and is initially zero everywhere and remains zero at infinity. The specific discharge is approximated as steady and uniform in each layer; the effect of the cables on the flow field is neglected. The differential equation (Equation 4.1) with the stated initial and boundary conditions and a point source at the origin of strength $p$ was solved for solute transport by Hunt (1983), after which the analogy to heat transfer was made by Zubair and Chaudhry (1996) and Diao et al. (2004). The solution is written here as

$$T = \frac{p}{4\pi\rho c\sqrt{D_x D_y}} \exp\left(\frac{x}{B}\right) \mathrm{W}\left(\frac{A}{t}, \frac{r}{B}\right) \tag{4.4}$$

where

$$A = \frac{r^2}{4D_x} \tag{4.5}$$

$$B = 2D_x \frac{\rho c}{q\rho_w c_w} \tag{4.6}$$

$$r = \sqrt{x^2 + \frac{D_x}{D_y} y^2} \tag{4.7}$$

$$W\left(\frac{A}{t}, \frac{r}{B}\right) = \int_{A/t}^{\infty} \frac{1}{s} \exp\left(-s - \frac{r^2}{4B^2 s}\right) ds \tag{4.8}$$



where W is known in the groundwater literature as the Hantush Well function (Hantush, 1956). The corresponding steady state temperature, $T(t_\infty)$, is given by (Zubair and Chaudhry, 1996; Diao et al., 2004)

$$T(t_\infty) = \frac{p}{2\pi\rho c\sqrt{D_x D_y}} \exp\left(\frac{x}{B}\right) K_0\left(\frac{r}{B}\right) \tag{4.9}$$

where $K_0$ is the modified Bessel function of the second kind and order zero. Combination of Equations 4.4 and 4.9 gives

$$T(t) = \frac{T(t_\infty)}{2\,K_0\left(\frac{r}{B}\right)} W\left(\frac{A}{t}, \frac{r}{B}\right) \tag{4.10}$$

It is noted that half the steady state temperature is reached when $t = 2\frac{A}{r/B} = \frac{r\rho c}{q\rho_w c_w}$ (Wilson and Miller, 1978). The solution for a heat source that is turned on at $t = 0$ and turned off at $t = t_0$ is obtained from superposition as

$$T(t, t_0) = \begin{cases} \frac{T(t_\infty)}{2K_0(r/B)} W\left(\frac{A}{t}, \frac{r}{B}\right), & 0 < t \le t_0 \\ \frac{T(t_\infty)}{2K_0(r/B)} \left[W\left(\frac{A}{t}, \frac{r}{B}\right) - W\left(\frac{A}{t-t_0}, \frac{r}{B}\right)\right], & t > t_0 \end{cases} \tag{4.11}$$

The temperature response presented in Equation 4.11 is expressed as a function of three lumped parameters, $A$, $\frac{r}{B}$, and $T(t_\infty)$, which account for the position of the fiber-optic cable relative to the heating cable ($x$ and $y$), and the parameters of the problem ($q$, $\rho c$, $\rho_w c_w$, $\kappa$, $\beta_x$, $\beta_y$, and $p$).

The temperature response depends on the location of the measurement relative to the heat source. Example temperature responses at 1 cm downstream (blue crosses) and 1 cm upstream (orange diamonds) of the heat source are

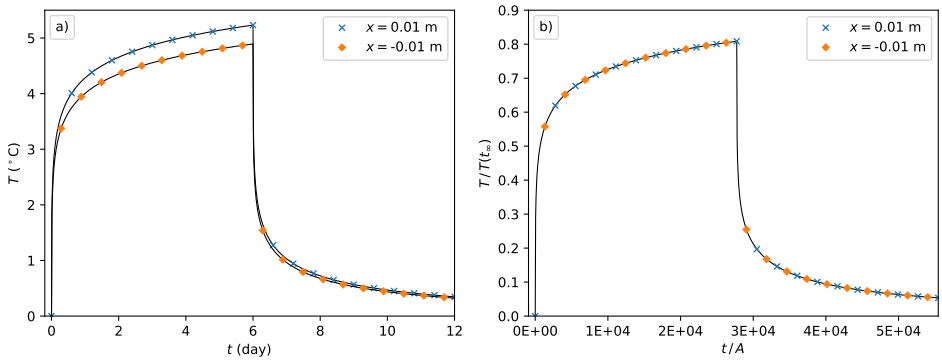


Figure 4.1: a) Example of a temperature response 1 cm downstream (blue crosses) and 1 cm upstream (orange diamonds) of the heat source using the mean parameter values of Table 4.2 and $q = 0.5$ md$^{-1}$. b) Non-dimensionalized form of the temperature response shown in Figure 4.1a.



shown in Figure 4.1a. The two temperature responses are significantly different during the heating period, but are similar after the heat source is turned off. The scaled temperature $\frac{T(t)}{T(t_\infty)}$ is plotted as a function of the scaled time $\frac{t}{A}$ in Figure 4.1b. The two temperature responses have the same $A$ and $r/B$, such that they overlap in Figure 4.1b.

## 4.3 Estimation of specific discharge from measurements

Values for the lumped parameters $A$, $\frac{r}{B}$, and $T(t_\infty)$ are obtained by fitting Equation 4.11 to temperature measurements of a heat pulse response test as described in Section 4.4. Note that these parameters can be obtained without knowledge of the exact position of the temperature measurement relative to the heat source. The specific discharge is obtained from $A$ and $r/B$ by rewriting Equation 4.6 as

$$q = 2D_x \frac{\rho c}{\rho_w c_w} \frac{1}{B} \tag{4.12}$$

Multiplication by $r/\sqrt{4D_x A}$, which equals one (Equation 4.5), gives

$$q = \frac{\rho c}{\rho_w c_w} \frac{r}{B} \frac{1}{\sqrt{A}} \sqrt{D_x} \tag{4.13}$$

Substitution of Equation 4.2 for $D_x$ finally gives

$$q = \frac{1}{\rho_w c_w} \frac{r/B}{\sqrt{A}} \sqrt{\rho c \left(\kappa + \beta_x q \rho_w c_w\right)} \tag{4.14}$$

Table 4.1: Values for the thermal properties used for Case Studies I and II.

| Parameter | Estimated distribution | Units |
|---|---|---|
| $\rho_w c_w$ | 4.185 | $MJm^{-1}°C^{-1}$ |
| $\kappa\rho c$ | $N(\mu$=566, $\sigma$=15.7) | $GJ^2s^{-1}m^{-2}°C^{-2}$ |
| $\beta_x \rho c$ | $LogN(\mu$=0.137, $\sigma$=0.110)[a] | $MJ°C^{-1}$ |

[a]95% of the log-Normal distribution lies between 0.027 and 0.425 $MJ°C^{-1}$

The specific discharge $q$ can now be determined from parameters $A$, $\frac{r}{B}$, and a third term. Note that $A$ and $\frac{r}{B}$ are both functions of $r$, but the ratio $\frac{r/B}{\sqrt{A}} = \frac{q\rho_w c_w}{\rho c\sqrt{D_x}}$ does not depend on $r$, which makes the expression for the specific discharge independent of the position of the temperature measurement relative to the heat source. The term under the square root sign consists of a thermal conductivity component and a hydrodynamic dispersion component. Equation 4.14 may be solved explicitly for $q$ by rewriting the equation

$$q = \frac{1}{\rho_w c_w}\left(\left[\frac{r/B}{\sqrt{A}}\right]^2 \frac{\beta_x \rho c}{2} + \frac{r/B}{\sqrt{A}}\sqrt{\kappa\rho c + \left[\frac{1}{2}\frac{r/B}{\sqrt{A}}\beta_x \rho c\right]^2}\right) \quad (4.15)$$

Equations 4.14 and 4.15 allow for the calculation of the specific discharge without knowledge of the position of the temperature measurement relative to the heat source by estimating $\frac{r/B}{\sqrt{A}}$, $\rho_w c_w$, $\kappa\rho c$, and $\beta_x \rho c$. Approximate values and distributions for the thermal properties of saturated sand with a porosity of 0.35 are used for Case Studies I and II (Table 4.1). The thermal dispersivity $\beta_x$ has the largest uncertainty. Similar to solute dispersivity, the thermal dispersivity is scale dependent (Marsily, 1986). Reported values range from 0.002 m for a heat pulse probe experiment (Hopmans et al., 2002), to 0.1 m for a push-pull pumping test (Vandenbohede et al., 2009), to 1 m for a closed geothermal system (Molina-Giraldo et al., 2011a). The scale of the presented heat pulse test is somewhere between the heat probe experiment of (Hopmans et al., 2002) and the push-pull pumping test of (Vandenbohede et al., 2009). The distribution of $\beta_x$ used to estimate the distribution of $\beta_x \rho c$ in Table 4.1 is log-Normal with a 95% confidence interval between 0.01–0.16 m.

## 4.4 Curve fitting procedure

The temperature response is measured with DTS along the fiber-optic cable and is normalized by subtracting the background temperature. Temperature measurements are representative for short sections of the cable. The pulse response

for each section is described by Equation 4.11. The parameters $T(t_\infty)$, $A$, and $\frac{r}{B}$ for each of these sections are estimated from the measured temperature response with the curve fitting procedure described below. The residuals, $\varepsilon$ [Θ], are the differences between modeled and measured temperatures. The root mean squared error, RMSE [Θ], is defined as

$$\text{RMSE} = \sqrt{\frac{\sum_{t=1}^{m} \varepsilon_t^2}{m}} \tag{4.16}$$

where $m$ is the number of time steps.



The residuals are likely correlated in time. A first-order autoregressive model is used to remove the autocorrelation in the residuals

$$\varepsilon_t = \alpha\, \varepsilon_{t-1} + n_t \tag{4.17}$$

where $\alpha$ [-] is the autoregressive parameter, and $n_t$ [Θ] is the remaining noise at time step $t$. The noise is approximated as independent and identically distributed. The parameters $T(t_\infty)$, $A$, $\frac{r}{B}$, and $\alpha$ are estimated by minimizing the root mean squared noise

$$\text{RMSN} = \sqrt{\frac{\sum_{t=2}^{m} n_t^2}{m-1}} = \sqrt{\frac{\sum_{t=2}^{m} \left(\varepsilon_t - \alpha\, \varepsilon_{t-1}\right)^2}{m-1}} \tag{4.18}$$

The RMSN is minimized with a Levenberg-Marquardt algorithm (Marquardt, 1963) using `LMFIT` (Newville et al., 2014), a high-level Python interface to the `scipy.optimize` module (Virtanen et al., 2020). A Monte-Carlo analysis is performed in three steps to estimate the uncertainty of the estimated specific discharge. First, the covariance matrix is estimated for the parameters $A$, $\frac{r}{B}$, $T(t_\infty)$, and $\alpha$. Second, a set of $10^6$ parameter combinations is drawn from a multivariate Normal distribution. Parameter sets of $\kappa\rho c$ and $\beta_x \rho c$ are drawn independently from the distributions presented in Table 4.1. Third, the specific discharge is calculated for each of the parameter combinations with Equation 4.15, and the 2.5 and 97.5 percentiles are used for the 95% confidence interval. The estimation of the confidence interval assumes the thermal response is correctly approximated by Equation 4.15. A Jupyter notebook with the curve fitting procedure and test data is provided as supplement material.

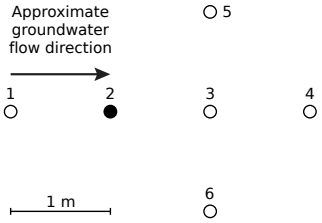


Figure 4.2: Top view of Case Study I. The circles represent the locations of the fiber-optic cables at the surface. The heating cable is located at the filled circle.

## 4.5 Case Studies

The presented approach is applied to two case studies. It is tested in Case Study I, which uses the data from Bakker et al. (2015). The range of applicability is explored in Case Study II, where the cables are installed much deeper, the specific discharge is a lot smaller and varies more with depth.

### 4.5.1 Case Study I: Dunes near Castricum

The objective of Case Study I is to test the presented approach when the temperature response is measured at different positions relative to the heating cable. Use is made of the dataset described in Bakker et al. (2015), who conducted an active heat pulse response test at a managed aquifer recharge system in the coastal dune area near Castricum, The Netherlands. Water flows from elongated infiltration basins over a distance of 80 m to a row of shallow wells parallel to these basins; the median residence time is approximately 50 days (Tombe et al., 2018b). Fiber-optic cables were inserted with direct-push equipment at six locations; at location 2 the fiber-optic cable is accompanied by a heating cable (Figure 4.2). The fiber-optic cable is 6 mm thick, contains 2 multi-mode 50/125 $\mu$m fibers and is heavily reinforced to protect the fibers during installation. The heating cable is an off-the-shelf model that is 7 mm thick and produces 30 $\mathrm{Wm}^{-1}$. The cables at location 2 reached a depth of 21 m below surface level, while the others reached a depth of 15 m. The heating cable was surrounded by multiple closely spaced fiber-optic cables to determine both the magnitude and direction of the velocity, but the direction is not considered in this chapter. The position of each cable relative to the heating cable is known at the surface (Figure 4.2) but unknown at depth, as the cables were inserted with direct push, which gives small deviations from the vertical that were not measured.

A heat pulse of 30 $\mathrm{Wm}^{-1}$ was generated for 3.8 days and the response was measured with DTS for 8.4 days with an acquisition time of 10 minutes on a 25 cm sampling interval. The Silixa Ultima was used with a spatial resolution of 0.29 m and a factory reported accuracy of 0.02 °C corresponding to the 10

minute acquisition time and the total fiber length. The measurements in the first 10 minutes after the heating cable is turned on ($t = 0$) and off ($t = 3.8$ d) are excluded from the fitting procedure. The model is unable to simulate these measured temperatures, because both the heating cable and the fiber-optic cable are approximated as infinitely thin in the model. However, their thickness is finite and their volumetric heat capacity is different than that of the surrounding soil, which influences the short-term temperature response measured in the fiber-optic cable.

A good fit was obtained for each cable at all depths with a RMSE of 0.03–0.09°C. The vertical variation in specific discharge and the 95% confidence intervals are estimated from the temperature measurements with respect to the background temperature at 6 locations with the procedure described in Section 4.4 and are shown in Figure 4.3. The mean width of the 95% confidence interval is 0.33 $md^{-1}$ for all locations except Location 4, where it is 0.60 $md^{-1}$. As the system is shallow, with a short residence time, the background temperature varied slightly during the experiment. A linear interpolation between the first and last temperature measurement was performed to account for the variation in background temperature. The error introduced by the approximation of the background temperature resulted in unrealistic values for the estimated specific discharge with a large confidence interval at depths where the temperature increase remained below 0.5 °C during the test; these are not shown in Figure 4.3. The temperature response at location 1 (upstream of the heating cable) remained below this threshold and is therefore not shown in Figure 4.3.

A similar specific discharge is estimated for each of the cables and the 95% confidence intervals are close to each other or overlap, even though the positions of the fiber-optic cables relative to the heating cable were unknown and vary between being next to the heating cable (location 2, orange line in Figure 4.3) up to several meters from the heating cable (locations 3–6). A slightly higher specific discharge, together with a larger confidence interval, is calculated for location 4 (green line). A qualitative estimate for the specific discharge is obtained from Tombe et al. (2018b) by dividing the distance between the recharge basin and the extraction well (80 m) by the median of the residence time (50 days) and multiplying it by the porosity (0.35), resulting in an estimate of 0.56 $md^{-1}$. Bakker et al. (2015) estimated a pore-water velocity profile (Figure 6 in their paper), which is similar to the specific discharge profile (Figure 4.3 of this chapter) when multiplied with the porosity. It is noted that Bakker et al. (2015) did not account for thermal dispersion, which affects the estimate of the specific discharge significantly for this case (see Section 4.6.2).

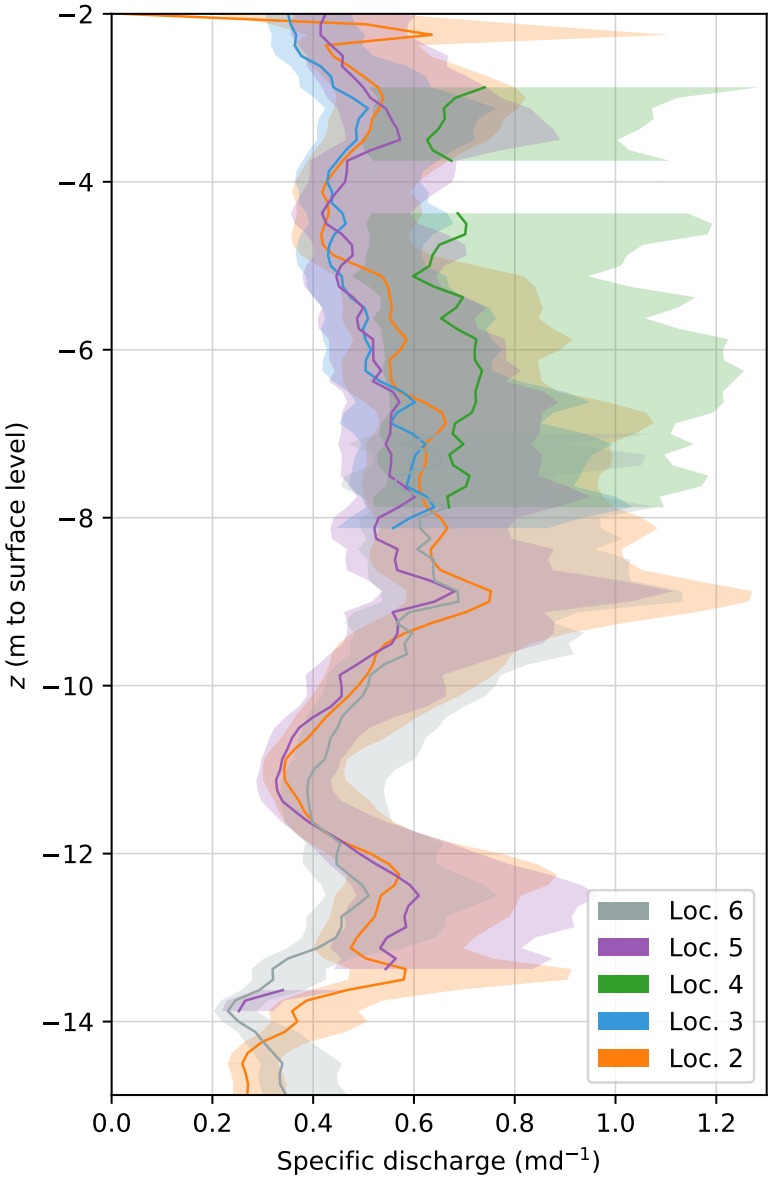


Figure 4.3: The specific discharge (line) and the 95% confidence intervals (shaded) estimated for locations 2–6 of Case Study I, at depths where the measured temperature increase was at least 0.5 °C.

### 4.5.2 Case Study II: Horstermeer polder

The objective of Case Study II is to explore the range of applicability of the proposed approach. It is investigated whether the specific discharge can be measured over larger depth (up to 45 m) and whether vertical variations of the specific discharge can be measured accurately. This case study is located in the Horstermeer polder in the Netherlands, which is an approximately circular polder with a diameter of 3 km. The heating cable and fiber-optic cable are installed at the edge of the polder, 50 m from the surrounding lakes and canals. The water level in the polder is maintained at approximately 2 m below the surrounding lakes and canals, resulting in significant groundwater flow from the lakes and canals into the polder. The cover layer is approximately 1.5 m thick and is very heterogeneous, while the aquifer below consists of different types of sands. Wielink (2016) showed with geophysical methods and through numerical modeling that horizontal flow is significantly larger at a depth between 25 to 35 m.



Installation of the fiber-optic cables was modified from the approach used in Case Study I (Bakker et al., 2015). Thinner push rods were used to reach a depth of 45 m, but these only fit a single composite fiber-optic cable and a heating cable. The same fiber-optic cable was used as in Case Study I, which contains two fibers. Their endings are welded together with a flexible fiber near the drive point (Figure 4.4) to support double-ended DTS calibration (Giesen et al., 2012). A plastic cover is attached to the steel drive point and filled with epoxy to fix the fragile fibers and the heating cable. A thinner heating cable with a diameter of 5 mm was installed (compared to Case Study I), which can generate a heat pulse of 20 $\mathrm{Wm}^{-1}$. In contrast to Case Study 1, the heating and fiber-optic cables were not taped together, but were kept loose during installation. Slack tends to occur in one of the cables when they are taped together, making it more difficult to lace the cables through the push rods. Alternatively, a fiber-optic cable with an embedded resistance wire could have been used. This has the advantage of being easier to install, but may cause problems with getting too hot and was not investigated.

The heat pulse was generated for 4.8 days. The temperature response along the fiber-optic cable was measured with the Silixa Ultima for 10.9 days with an acquisition time of 5 minutes on a 0.125 m sampling interval. The factory-reported temperature accuracy is 0.024 °C. The pulse response over the depth is shown in Figure 4.5a. The temperature measurements in the first two meters below surface level reflect partially saturated soils and are influenced by surface temperature fluctuations; their interpretation is beyond the scope of this chapter. The thermal properties of the drive point are different than that of the

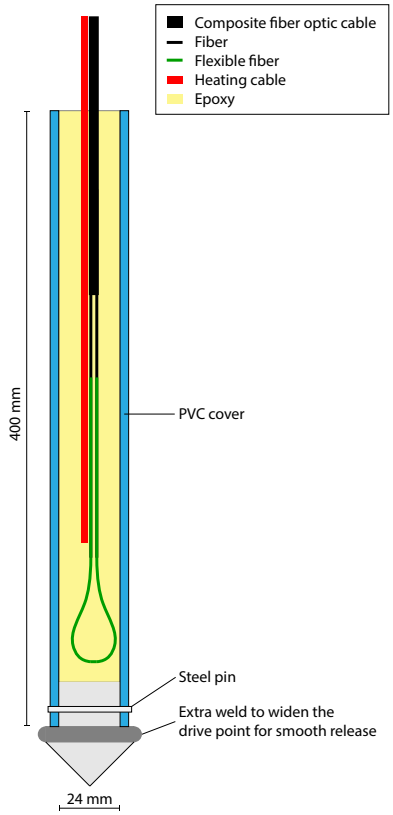


Figure 4.4: Custom made drive point. Not to scale.

aquifer, which influences the temperature measurements in the bottom two meters and are therefore not shown in Figure 4.5a. The temperature increase just before the heating cable was turned off is shown in Figure 4.5b. The largest temperature increase of 5.9 °C is observed at 23.2 m below surface level and the smallest increase of 3.1 °C at 30 m below surface level. The temperature increase fluctuates with depth, as the fiber-optic cable twists around the heating cable and the temperature increase just upstream of the heating cable is significantly smaller than just downstream (Figure 4.1a).

The specific discharge was estimated with the procedure presented in Section 4.4. A good fit was obtained at all depths with a RMSE of 0.04–0.05 °C. The measured (dots) and modeled (dashed lines) temperature responses at 23.2 (blue) and 30 m (orange) below surface level are shown in Figure 4.5c; the corresponding residuals are shown with colored dots in Figures 4.5d and Figure 4.5e, respectively. The temporal variation in the residuals is similar at all depths and shows a daily pattern originating from the DTS-system. The noise (Equa-

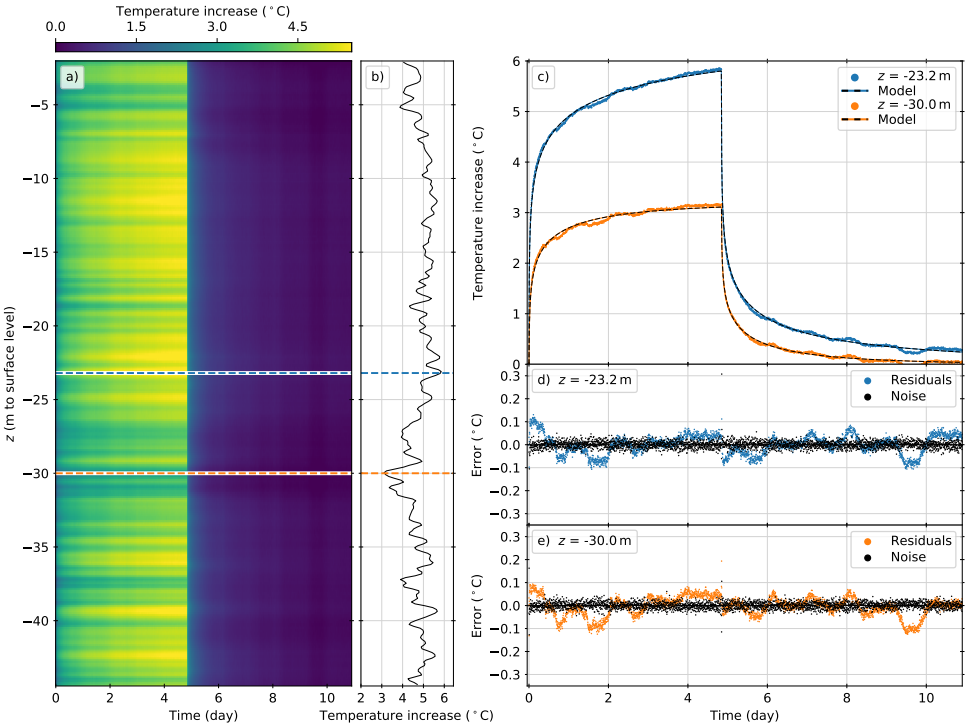


Figure 4.5: a) Measured temperature response for Case Study II. b) Temperature profile at $t = 4.8$ d, just before the heating cable was turned off. c) Measured and modeled temperature response at two depths. d, e) Residuals and noise at two depths.

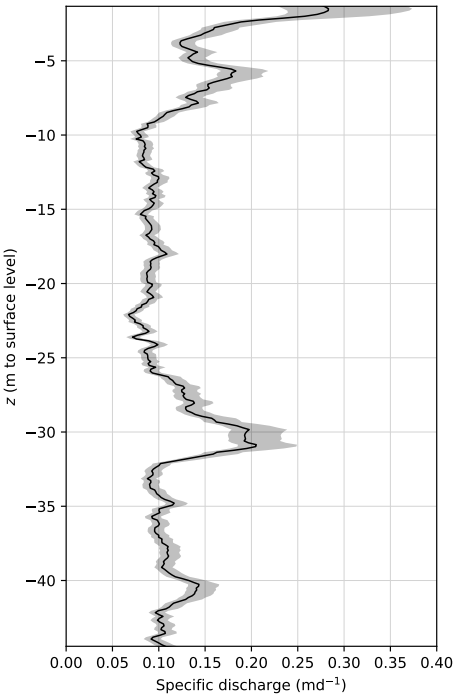


Figure 4.6: The specific discharge and its 95% confidence interval estimated for Case Study II.

tion 4.17), shown with black dots in Figures 4.5d and 4.5e, does not show this temporal variation and is distributed approximately Normal. Similar to Case Study I, the measurements in the first 10 minutes after the heating cable is turned on ($t = 0$) and off ($t = 4.8$ d) are excluded from the fitting procedure. The estimated specific discharge and its 95% confidence interval are shown in Figure 4.6. The mean width of the 95% confidence interval is 0.026 md$^{-1}$. The specific discharge varies between 0.07 and 0.11 md$^{-1}$, except for the first 8 m and between 27–32 m below surface level, where the specific discharge is larger, as was expected from the geophysical study and numerical modeling of Wielink (2016). The largest specific discharge of 0.2 md$^{-1}$ is estimated at 31 m below surface level.

## 4.6 Discussion

Several approximations were made to estimate the specific discharge from the temperature measurements of which three require extra attention and are discussed below.

Table 4.2: Parameters used in the numerical model.

| | |
|---|---|
| $\rho c$ | 2.730 MJm$^{-1}$°C$^{-1}$ |
| $\rho_w c_w$ | 4.185 MJm$^{-1}$°C$^{-1}$ |
| $\kappa$ | 2.4 Wm$^{-1}$°C$^{-1}$ |
| $\beta_x$ | 0.05 m |
| $\beta_y$ | 0.005 m |
| $\beta_z$ | 0.0005 m |

### 4.6.1 Vertical conductive heat transfer

In the presented approach the aquifer is discretized vertically in many horizontal layers. The temperature measurements in each layer are considered independent of the other layers and heat transfer between layers is neglected. If there is a large difference in the specific discharge between two layers, a temperature difference develops during the test and heat is exchanged vertically by means of conduction. This is neglected in the presented approach. If vertical heat transfer is not negligible, sharp changes in the specific discharge and thin layers with a different specific discharge can be missed. A sharp change in the specific discharge is estimated for Case Study II at approximately 28–32 m below surface level, and the question arises whether the maximum specific discharge at this depth is correctly estimated.

A numerical model was constructed to investigate the effect of vertical heat conduction on the estimated specific discharge. An aquifer is modeled with a constant horizontal specific discharge of 0.1 md$^{-1}$, except for a layer where the specific discharge is higher ($q_f$). The layer is located halfway the aquifer and has a thickness $H$. A 20 Wm$^{-1}$ vertical line source is located at the origin and is turned on at the beginning of the model run and turned off after 4.8 days. Other parameters are given in Table 4.2. Coupled groundwater flow and heat transfer are modeled with SEAWAT (Langevin et al., 2007). The equations for thermal conduction and hydrodynamic dispersion are solved with an implicit finite difference scheme and the thermal advection is solved using a third-order total-variation-diminishing scheme (Zheng and Wang, 1999). The cell sizes vary from $0.5 \times 0.5 \times 2.5$ cm to $1 \times 1 \times 1$ m ($x$, $y$, $z$). The smallest cells are used at the origin near the top and bottom of the layer with larger specific discharge, while the largest cells are used near the boundaries of the model.

The temperature response is modeled for two values of $q_f$ and two values of $H$, resulting in four cases labeled A–D (Table 4.3). The specific discharge is estimated from the modeled temperature at 2 cm from the heating cable perpendicular to the flow direction using the presented approach. Results are shown with blue and orange lines in Figure 4.7, which also shows the true specific discharge (black). A similar specific discharge is estimated from modeled temperatures at 2 cm upstream and 2 cm downstream of the heating cable (not shown).

Table 4.3: Model configurations.

| Case | $q_f$ (md$^{-1}$) | $H$ (m) |
|---|---|---|
| A | 0.2 | 5.0 |
| B | 0.5 | 5.0 |
| C | 0.2 | 2.0 |
| D | 0.5 | 2.0 |

The true specific discharge jumps at the boundary of the layer with higher $q_f$, while the estimated specific discharge shows a smooth transition. The height of the transition zone, from 10% to 90% of the total increase, is termed the spatial resolution of the estimated specific discharge here. The spatial resolution for $q_f = 0.2$ md$^{-1}$ (Case A) is 1.71 m and reduces to 1.35 m for $q_f = 0.5$ md$^{-1}$ (Case B). For Cases A and B, the layer thickness is 5 m, which is larger than the spatial resolution, so that the largest estimated specific discharge approximates the true specific discharge quite well. When the layer thickness is smaller than the spatial resolution (Cases C and D), the peak of the specific discharge is underestimated. For example, when $H = 1$ m (Cases C and D) the peak of the estimated specific discharge is only 55% of the true specific discharge (Figure 4.7b).

The thickness of the region with a larger specific discharge of Case Study II is approximately 4 m (between 28–32 below surface level) and thus larger than the spatial resolution of the estimated specific discharge. It is therefore expected that the peak specific discharge in this layer is estimated reasonably well, but the estimated transition of the specific discharge is likely smoother than in reality.

### 4.6.2 Hydrodynamic dispersion

The parameters $A$, $r/B$, and $T_\infty$, are obtained from temperature measurements with the curve fitting procedure presented in Section 4.4. In addition, estimates of $\kappa\rho c$, $\beta_x\rho c$, and $\rho_w c_w$ (Equation 4.15) are needed to calculate the specific discharge. The estimate of the specific discharge increases for larger $\beta_x$ and the increase is larger for a larger specific discharge. Similar observations were made in studies by Hopmans et al. (2002) and Lu et al. (2018). The effect of hydrodynamic dispersion can be neglected when $\kappa \gg \beta_x q \rho_w c_w$ (Equation 4.14) or

$$q \ll \frac{\kappa}{\beta_x \rho_w c_w} \tag{4.19}$$

The condition for neglecting hydrodynamic dispersion with the values of Table 4.2 becomes

$$q\beta_x \ll 0.05\ \text{m}^2\text{d}^{-1} \tag{4.20}$$

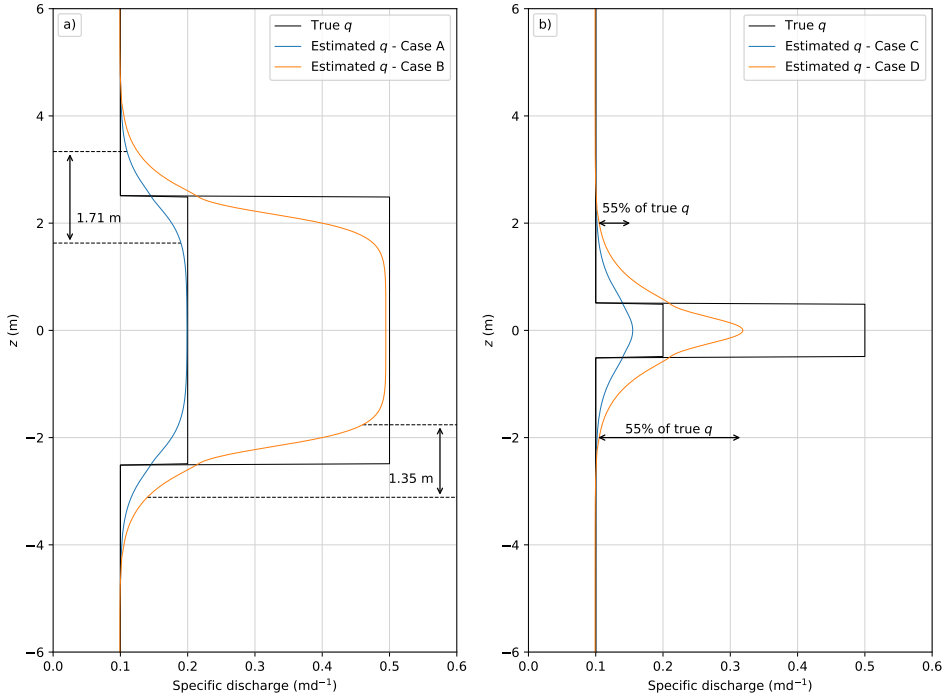


Figure 4.7: a) True (black) and estimated specific discharge for Case A (blue) and Case B (orange). b) True (black) and estimated specific discharge for Case C (blue) and Case D (orange).

The uncertainty in $\beta_x$ is much larger than the uncertainty in $\kappa$ and $\rho_w c_w$. This makes it difficult to decide for what values of $q$ dispersion can be neglected. For $\beta_x = 0.05$ m (Table 4.2), dispersion may be neglected when $q \ll 1$ md$^{-1}$.

The term under the square root sign in Equation 4.14 reduces to $\sqrt{\kappa\rho c}$ when hydrodynamic dispersion is neglected, so that Equation 4.14 can be written as

$$q = \frac{\sqrt{\kappa\rho c}}{\rho_w c_w}\frac{r/B}{\sqrt{A}} \tag{4.21}$$

$$\approx 0.18\,\frac{r/B}{\sqrt{A}}\,(\mathrm{md}^{-1}) \tag{4.22}$$



The term $\sqrt{\kappa\rho c}$ is relatively constant for different types of saturated sand, because either a larger porosity or a larger clay content results in a larger $\rho c$ and a lower $\kappa$.

The specific discharge is estimated for location 2 of Case Study I (next to the heating cable) for three values of $\beta_x$ and the results are shown in Figure 4.8. The estimated specific discharge is significantly larger when $\beta_x = 0.1$ m (green) than when hydrodynamic dispersion is neglected ($\beta_x = 0$ m, blue), as is to be expected as $q$ is around 0.5 md$^{-1}$. For example, the estimated specific discharge is 72% larger at 9 m below surface level for $\beta_x = 0.1$ m than for $\beta_x = 0$ m. The effect of hydrodynamic dispersion on the estimated specific discharge is much smaller for Case Study II (Figure 4.9), with a maximum increase of 20% at 31 m below surface level. This is to be expected as $q = 0.1$–$0.2$ md$^{-1}$ $\ll 1$ md$^{-1}$. The same holds for the confidence intervals of the estimated specific discharge presented in Figure 3 and 6; the confidence intervals are wider for large flows due to the uncertainty in the dispersivity.

### 4.6.3 Heterogeneity in horizontal layers

In this study, effective values of $\rho_w c_w$, $\kappa\rho c$, and $\beta_x \rho c$ for the measurement area are used to estimate an effective value of $q$. The size of the measurement area is estimated by calculating the area that is heated at least 0.1°C during the test. The measurement area is approximately 5.9 m$^2$ if the specific discharge is 0.1 md$^{-1}$ and 8.3 m$^2$ if the specific discharge is 0.5 md$^{-1}$, using the values of Table 4.2 and a heat pulse of 4.8 days. Not all parts of the measurement area contribute equally to the estimate of the effective $q$. Knight et al. (2007) assessed the effect of heterogeneity on the estimation of the heat capacity and water content in the vadose zone with a dual-probe heat-pulse sensor. They concluded that the measurements are local and the area close to the heater and the sensor contributes

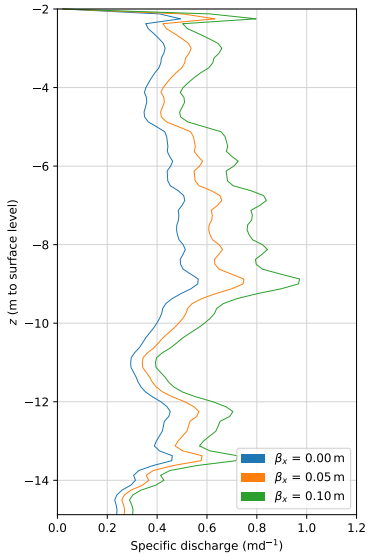


Figure 4.8: The specific discharge for three values of $\beta_x$ for location 2 of Case Study I.

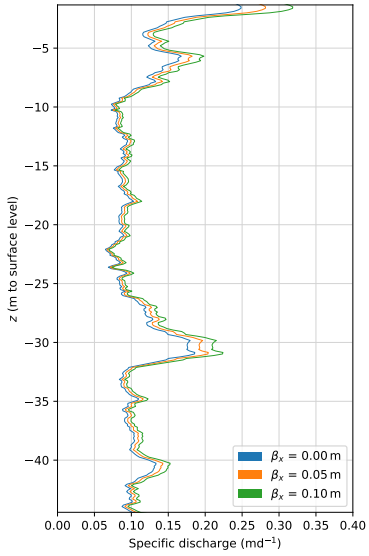


Figure 4.9: The specific discharge for three values of $\beta_x$ for Case Study II.

most. Oliver (1993) performed a similar assessment for a pumping test by quantifying the influence of the storativity and transmissivity at each location on the observed drawdown. He concluded that at later times the influence extends farther away from the well and the effective values represent a larger area. Future research into the combined effect of heterogeneity and test duration is needed to understand the full effect of heterogeneity on the estimated effective values.

## 4.7 Conclusion

A new approach is presented to estimate the specific discharge from a heat pulse response test using a heating cable and a single fiber-optic cable. The temperature is measured along the fiber-optic cable with a Distributed Temperature Sensing (DTS) system. The two cables are installed together with direct-push equipment, such that the cables are in direct contact with the aquifer and no borehole is needed; it is assumed that the disturbance of the flow field due to installation is neglected. Bakker et al. (2015) found that the cables twist when they are installed together, such that the position of the fiber-optic cable relative to the heating cable in the subsurface is unknown. The presented approach can be used to estimate the magnitude of the specific discharge independent of the position of the fiber-optic cable relative to the heating cable.

The aquifer is discretized vertically in many horizontal layers. Each layer is approximated as homogeneous with a uniform flow perpendicular to the heating cable. The temperature response in each layer is fitted with three lumped parameters, from which the specific discharge is calculated by estimating a conduction term and a hydrodynamic dispersion term. The conduction term appears to be relatively constant for different types of sand. Hydrodynamic dispersion can be neglected when the specific discharge is significantly smaller than 1 $md^{-1}$. The estimate of the specific discharge increases for a larger longitudinal thermal dispersivity. The uncertainty in the dispersivity results in larger uncertainty in the estimation of larger specific discharge values.

The new approach was successfully tested in Case Study I using data of Bakker et al. (2015). In Case Study II it was demonstrated that smaller values of the specific discharge ($\sim$0.1 $md^{-1}$) can be measured accurately over larger depth ($\sim$45 m) including a region with significantly higher specific discharge ($\sim$0.2 $md^{-1}$).

Vertical heat transfer between layers is neglected in the presented approach to estimate the specific discharge from the measured temperature response. The estimated specific discharge is smoother than in reality near jumps in the specific discharge. It was concluded from a 3D numerical model that the sharp

increase in the specific discharge in Case Study II results in a smooth transition in the estimate of the specific discharge over a distance of 1.35–1.71 m, termed the spatial resolution of the presented approach. The specific discharge in layers that are thinner than the spatial resolution are not fully captured. The layer in Case Study II where the specific discharge is larger is thick enough (∼4 m), that the peak flow in this layer is captured. Results at a finer resolution than the spatial resolution require the use of a 3D model that accounts for vertical heat transfer to estimate the specific discharge from the measured temperature response.



## 4.8 Acknowledgments

All temperature measurements and derived estimates are available at `https://doi.org/10.5281/zenodo.1436300`. This work was funded in part by the Netherlands Organization for Scientific Research (NWO) within the program The New Delta with project number 869.15.006, and by Waternet, the Water Authority Amstel, Gooi and Vecht, the Municipality of Amsterdam, and the Province of Noord-Holland. The authors thank Tom Kind from Waternet for his assistance with the experimental setup of Case Study II.

# 5 Improved flow characterization from two active heat tracer tests



## 5.1 Introduction

Dispersion of heat is the spreading of heat with respect to the average pore flow velocity caused by local variations in the pore flow velocity. The value of the dispersivity is the same for solutes as it is for heat, although not all researchers agree (see discussion in Vandenbohede et al. (2009)). At high flows that are estimated with active heat tracer tests (Chapter 4), the uncertainty in the specific discharge estimate is dominated by the uncertainty in the dispersion (Section 4.6.2). Estimation of the specific discharge can be improved by combining the results from two active heat tracer tests performed at the same location but under different flow conditions. In this chapter, heat tracer tests are performed in the vicinity of a well that pumped at two different rates. The setup is designed to do 8 active heat tracer tests simultaneously. An approach is presented that improves the estimates of the specific discharges but requires that a ratio of the specific discharges of the two tests is known a priori. The ratio of the two specific discharges is discussed separately. This ratio can be estimated with small uncertainty from the thermal parameters, and may, for example, be used to monitor the clogging of filters or to estimate seasonal variations of groundwater, which can be valuable for regional groundwater models.

At low flow, the estimation of the specific discharge is not sensitive to the longitudinal thermal dispersivity so that the specific discharge can be estimated accurately. However, at high flow, the uncertainty in the longitudinal thermal dispersivity leads to large uncertainty in the estimate of the specific discharge (Section 4.6.2). Thermal dispersivity is of the same order as solute dispersivity, and similar to solute dispersivity, its values changes with the scale of the experiment (Section 4.3). The longitudinal thermal dispersivity can be estimated by

performing two active heat tracer tests at the same location, with unknown specific discharges that are different, but of which the ratio is known. This estimate of the longitudinal dispersivity can be used to obtain more accurate estimates of the specific discharges.

In certain cases, the variation of the specific discharge over time is of larger interest than the values of the specific discharges themselves. The ratio of two specific discharges at the same location at different times may already be estimated by estimating the specific discharge for each test separately using the approach presented in Section 4.3. The ratio itself can be estimated accurately because most of the uncertainty contributed by the thermal parameters cancels out, because the thermal properties are known to be the same for both tests.

An extensive pumping test was performed in a confined aquifer. Heat tracer tests were conducted at two different extraction rates during the pumping test, which lasted for over 3 months. Heating cables and fiber-optic cables were installed at 8 locations to do 8 independent active heat tracer tests simultaneously. The locations varied in distance from the well, so that a wide range of flows could be measured, and the proposed improvement to the estimation of the specific discharge could be tested. The driving points that were used at the site were modified to make use of loopback connectors to simplify the manufacturing. Unexpectedly, the loopback connectors negatively affected the DTS measurements. Modifications to the DTS calibration procedure are presented that reduce the effects from the loopback connectors.



This chapter is organized as follows. First, the equations are derived to estimate the thermal dispersion from two active heat tracer tests at different flow rates (Section 5.2). Next, it is explained how the uncertainty that is contributed by the thermal parameters cancels out in the estimation of the ratio of the specific discharges (Section 5.3). The study site and setup are described in Section 5.4, followed by a description of the modified approach for DTS calibration subject to artifacts from connectors in Section 5.5. Results of the two approaches are described in Section 5.6, followed by conclusions in Section 5.7.

## 5.2 Estimation of the thermal dispersion given the ratio of the specific discharges

Consider two heat tracer tests performed at the same location, like the ones presented in Chapter 4. The soil is actively heated with a heating cable, and the temperature response is measured with DTS along a fiber-optic cable. A function of three lumped parameters is fitted to the thermal response. The specific

discharge is obtained from the lumped parameters with estimates of $\rho_w c_w$, $\kappa\rho c$, and $\beta_x \rho c$ (Section 4.3). The first term is the volumetric heat capacity of water and has a known value. The second term is the product of the isotropic thermal conductivity of the soil and the volumetric heat capacity of the soil. It is fairly constant for different types of saturated sand, and can therefore be estimated from literature values. The third term is the product of the longitudinal dispersivity and the volumetric heat capacity of the soil. The range of values of the third term is large, which introduces significant uncertainty in the estimates of the specific discharge, especially at larger values of the specific discharge. A good estimate of the third term may be obtained by combining the measurements from two heat tracer tests when the ratio of specific discharges from the two tests is known. In addition, the estimates can be beneficial for other heat tracer tests where similar lumped thermal parameters can be expected.



The parameters $A$, $r/B$, and $T(t_0)$ are estimated for both tests using the procedure presented in Section 4.4, with a modified formulation of the thermal response that is presented in Appendix D.1. The parameters $A$ and $r/B$ at low and high flow are given by

$$A_1 = \frac{r_1^2}{4D_{x,1}}, \qquad A_2 = \frac{r_2^2}{4D_{x,2}} \tag{5.1}$$

$$\frac{r_1}{B_1} = \frac{r_1 \rho_w c_w q_1}{2\rho c D_{x,1}}, \qquad \frac{r_2}{B_2} = \frac{r_2 \rho_w c_w q_2}{2\rho c D_{x,2}} \tag{5.2}$$

where subscripts 1 and 2 refer to the thermal response measured at low and high flow, respectively. $D_x$ is the longitudinal thermal dispersion coefficient (Equation 4.2), and $r$ is the radial distance between the heating cable and the fiber-optic cable, which is a function of the longitudinal and transverse thermal dispersion coefficient (Equation 4.7). Parameters $D_x$ and $r$ are different under low and high flow conditions. The specific discharge of each test can be estimated from the fitted parameters with (Section 4.3)

$$q_1 = \frac{1}{\rho_w c_w}\left(\left[\frac{r_1/B_1}{\sqrt{A_1}}\right]^2 \frac{\beta_x \rho c}{2} + \frac{r_1/B_1}{\sqrt{A_1}}\sqrt{\kappa\rho c + \left[\frac{1}{2}\frac{r_1/B_1}{\sqrt{A_1}}\beta_x \rho c\right]^2}\right) \tag{5.3}$$

$$q_2 = \frac{1}{\rho_w c_w}\left(\left[\frac{r_2/B_2}{\sqrt{A_2}}\right]^2 \frac{\beta_x \rho c}{2} + \frac{r_2/B_2}{\sqrt{A_2}}\sqrt{\kappa\rho c + \left[\frac{1}{2}\frac{r_2/B_2}{\sqrt{A_2}}\beta_x \rho c\right]^2}\right) \tag{5.4}$$

The term $\beta_x \rho c$ is estimated by combining Equations 5.3, and 5.4 to

$$\beta_x \rho c = \text{function}\left(f, \frac{r_1/B_1}{\sqrt{A_1}}, \frac{r_2/B_2}{\sqrt{A_2}}, \kappa\rho c\right) \tag{5.5}$$

$$= \sqrt{\kappa\rho c}\,\frac{\sqrt{-fg}\left(f^2\left(\frac{r_1/B_1}{\sqrt{A_1}}\right)^2 - \left(\frac{r_2/B_2}{\sqrt{A_2}}\right)^2\right)}{fg\frac{r_1/B_1}{\sqrt{A_1}}\frac{r_2/B_2}{\sqrt{A_2}}} \tag{5.6}$$

where

$$f = \frac{q_1}{q_2} \tag{5.7}$$

$$g = f^2\left(\frac{r_1/B_1}{\sqrt{A_1}}\right)^2 - f\left(\frac{r_1/B_1}{\sqrt{A_1}}\right)^2 - f\left(\frac{r_2/B_2}{\sqrt{A_2}}\right)^2 + \left(\frac{r_2/B_2}{\sqrt{A_2}}\right)^2 \tag{5.8}$$

5

where $f$ has a known value that is larger than zero and not equal to one. Equation 5.6 returns a single value for $\beta_x \rho c$ since all the parameters are positive. This equation was obtained with the software package Maple and was numerically validated. An example where $\beta_x \rho c$ is estimated is shown in Section 5.6.1.

## 5.3 Accurate estimation of the ratio of specific discharges

The variation of the specific discharge over time has a larger interest than the specific discharges themselves in cases such as: monitoring the clogging of filters, estimating seasonal variation of flow with regional groundwater models, or estimating the effect of dike reinforcement. An expression for the ratio of the specific discharge of the two active heat tracer tests, $f$, can be obtained from Equations 4.14 and 5.7 as

$$f = \frac{r_1/B_1\sqrt{A_2}}{r_2/B_2\sqrt{A_1}}\sqrt{\frac{\kappa\rho c + q_1\beta_x\rho c\rho_w c_w}{\kappa\rho c + q_2\beta_x\rho c\rho_w c_w}} \tag{5.9}$$

which shows that the uncertainty in $f$ that is introduced by $\kappa\rho c$ and $\beta_x \rho c$ only manifests if the specific discharges of the two tests are not similar and the effect of thermal dispersion cannot be neglected with respect to the effect of thermal conduction (Section 4.6.2). Equation 5.9 may be solved explicitly with Equations 5.3, 5.4, and 5.7 using literature values for $\kappa\rho c$ and $\beta_x \rho c$.

Table 5.1: Location of the wells.

| Name | Description | X m+RDS | Y m+RDS | SL m+NAP | Top filter m+SL | Bottom filter m+SL |
|---|---|---|---|---|---|---|
| PW | Pumping well | 51135 | 416641 | -1.55 | -15.3 | -26.7 |
| IW1 | Infiltration well 1 | 51061 | 416751 | -1.38 | -16.5 | -29.5 |
| IW2 | Infiltration well 2 | 51170 | 416561 | -1.48 | -15.5 | -28.5 |
| IW3 | Infiltration well 3 | 51012 | 416691 | -0.96 | -16.5 | -29.5 |
| IW4 | Infiltration well 4 | 51220 | 416628 | -1.32 | -16.0 | -30.0 |

SL: Surface Level
RDS: Rijksdriehoekenstelsel (map projection, EPSG: 28992 (Amersfoort / RD New))
NAP: Amsterdam Ordnance Datum (vertical datum)

## 5.4 Study site

In this section, the methods that were introduced in Sections 5.2 and 5.3 are demonstrated with heat tracer tests performed during an extensive pumping test. The pumping test was performed in a confined aquifer. During the test, which lasted for over 3 months, water from the pumping well was circulated back to four infiltration wells. Heating cables and fiber-optic cables were installed at 8 locations to do 8 independent active heat tracer tests simultaneously. The locations varied in distance from the well, so that a wide range of flows could be measured. Active heat tracer tests were performed at two different pumping rates, with expected specific discharge measurements between 0.11 and 2.1 m/day. The driving point was modified to make use of loopback connectors to simplify the manufacturing. Unexpectedly, the loopback connectors negatively affected the DTS measurements, which made the heat tracer results unusable for 5 out of the 8 locations. The DTS calibration was modified to partially deal with the negative effects of the loopback connectors by making use of fiber sections that share the same temperature.



### 5.4.1 Study site overview

The study site is located on the island of Schouwen-Duiveland, the Netherlands. It consists of 1 extraction well, 4 injection wells, and 18 monitoring wells, placed in a field of 70 m by 205 m that is normally used for agriculture, and is shown in Figure 5.1. The measurements from the monitoring wells are excluded from the analysis of this chapter. The coordinates of the extraction well and injection wells and their filter depths are shown in Table 5.1, where RDS is the map projection used in the Netherlands. An intensive geotechnical measurement campaign was conducted that included 13 cone penetration tests, 10 sonic drillings, and 7 pulse drillings. The following characterization of layering of the subsurface is interpreted from the pulse drillings performed at the pumping well and

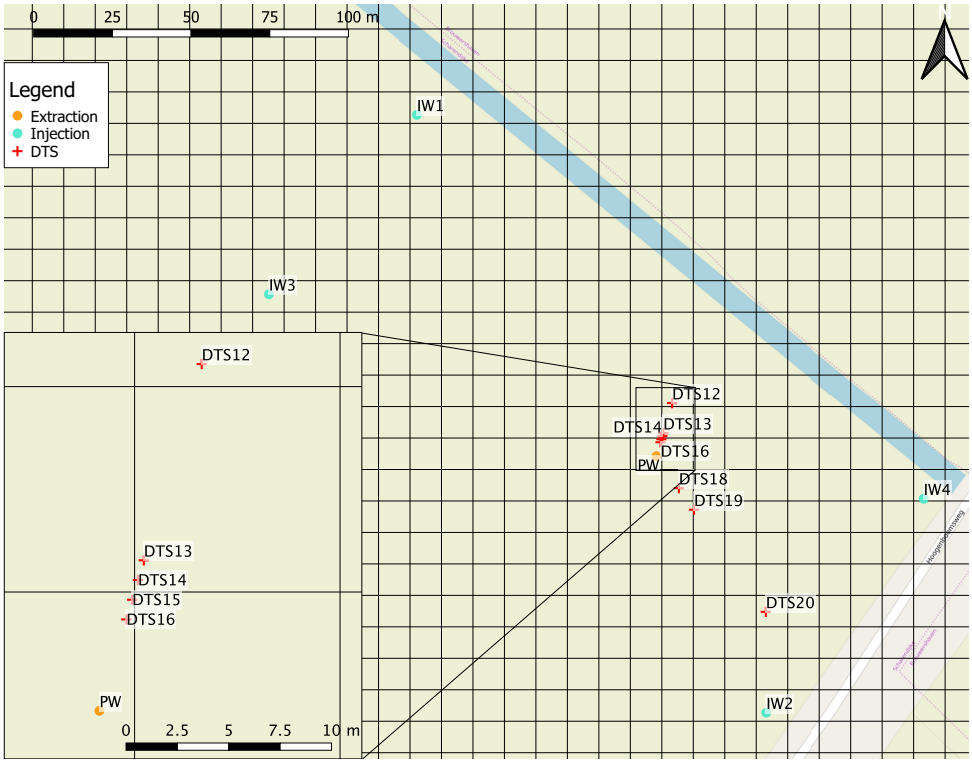


Figure 5.1: Map of the study site on the island of Schouwen-Duiveland, the Netherlands.

Table 5.2: Average extraction rates during heat tracer tests.

| Name | Rate during test 1 ($m^3/h$) | Rate during test 2 ($m^3/h$) |
|---|---|---|
| PW | 28.69 | 18.68 |
| IW1 | -9.06 | -6.18 |
| IW2 | -4.86 | -3.30 |
| IW3 | -9.35 | -5.96 |
| IW4 | -5.57 | -3.24 |

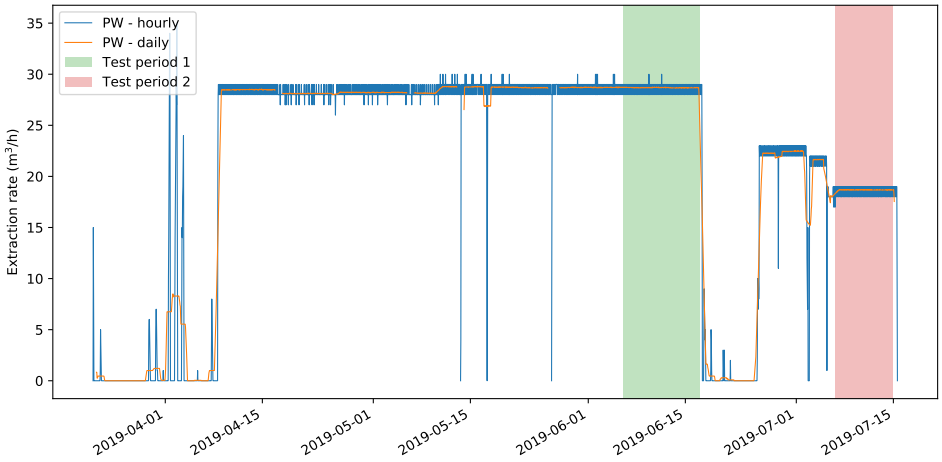


Figure 5.2: Extraction rate of the pumping well.



two meters south of the pumping well. The first 4.80 m is clay. Between 4.80 m and 12.20 m below the surface, the soil consists of sand with thin clay layers. The soil between 12.20 m and 15.35 m below the surface consists of clay and peat. Under this clay layer, the sand layer starts in which the well filter is located. This sand layer is 11.25 m thick near the pumping well, but is much thicker near Infiltration Well 1 and 3. Very coarse sand was identified in the bottom half of the sand layer (23.00 to 26.70 m below surface level) in samples from one of the two drillings. The bottom of the sand layer is a confining clay layer.

The water extracted from the extraction well is distributed over the four injection wells. Additionally, there is an overflow pipe that leads to the surface water, which was only used during the installation of the wells. The hourly extraction rate (with a precision of 0.1 $m^3/h$, shown in blue) and the centered moving daily-average of the extraction rate (shown in orange) are shown in Figure 5.2. During the first test, the average extraction rate was 28.69 $m^3/h$ and during the second test the average extraction rate was 18.68 $m^3/h$.

### 5.4.2 DTS setup

Fiber-optic cables were inserted 40 meters deep with direct-push equipment at 8 locations using the method presented in Section 4.5.2. The coordinates of the fiber-optic cables are listed in Table 5.3, and are shown in Figure 5.1. The specific discharges $q_1$ and $q_2$ listed in Table 5.3 are discussed in Section 5.4.3.

The drive point differs from the ones used in Bakker et al. (2015) and Section 4.5.2. The drive point used in the former study made use of a looped fiber-optic cable, such that three cables were laced through the push rods during installation (a heating cable and a looped fiber-optic cable). The goal of the latter

Table 5.3: Location of the inserted fiber-optic cables and specific discharges estimated from the groundwater model.

| Name | X (m+RDS) | Y (m+RDS) | $q_1$ (m/day) | $q_2$ (m/day) | $f = q_2/q_1$ |
|---|---|---|---|---|---|
| DTS12 | 51140.08 | 416658.38 | 0.55 | 0.36 | 0.65 |
| DTS13 | 51137.26 | 416648.83 | 1.27 | 0.83 | 0.65 |
| DTS14 | 51136.98 | 416647.87 | 1.47 | 0.95 | 0.65 |
| DTS15 | 51136.70 | 416646.91 | 1.73 | 1.12 | 0.65 |
| DTS16 | 51136.41 | 416645.95 | 2.10 | 1.37 | 0.65 |
| DTS18 | 51142.23 | 416631.36 | 0.78 | 0.51 | 0.65 |
| DTS19 | 51147.05 | 416624.50 | 0.47 | 0.30 | 0.65 |
| DTS20 | 51169.86 | 416592.05 | 0.17 | 0.11 | 0.66 |

RDS: Rijksdriehoekenstelsel (map projection)

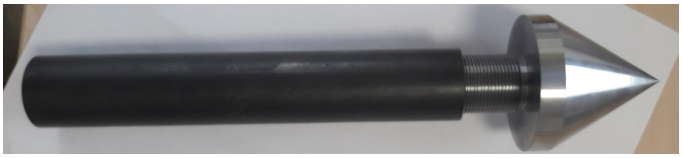

Figure 5.3: Newly developed drive point for inserting fiber-optic cables with cone penetration test equipment. Picture taken by Rolf Rekers, Wiertsema.

study was to reach deeper by using thinner push rods. The thinner rods can accommodate only two cables: a heating cable and a fiber-optic cable. The fiber-optic cable contained two fibers that were connected with welds in the drive point. The setup of this study is also designed to fit the thinner rods. However, during the installation the push rods buckled and the installation of the cables continued with thicker push rods, which have a greater resistance against buckling. It is complicated and labor intensive to weld the fiber ends while removing as little as possible of the reinforcement of the optical-fiber cable. The weld is replaced by a loopback connector (LC/UPC Duplex PVC OM4 50/125 Multimode Fiber Loopback Module, by FS.com). The conus and hollow cylinder of the new drive point are custom-made from hardened steel, and is shown in Figure 5.3. It has an internal length of 175 mm and an internal diameter of 25 mm. The internal space is used to house a fiber-loopback connector, ∼50 cm of fiber-optic cable, and the ending of a heating cable. Epoxy is used to fixate the loopback connector and fiber-optic cable. Heating cables that can produce up to 30 W/m were used at the 3 locations closest to the extraction well, and heating cables that can produce up to 20 W/m were used at the 5 other locations. The heating cables were shortened and lengthened during the installation. The final length of the heating cables changed and therefore also their heat production, thus the heat production of each cable is not exactly known.

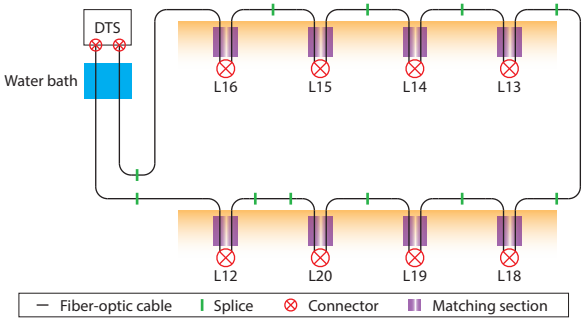


Figure 5.4: Schematization of the DTS setup

The fibers of the 8 locations are spliced together to create a single fiber to measure from both ends. The schematic layout of the fiber is shown in Figure 5.4. A coil of fiber was placed in a cooler box filled with water to calibrate Stokes and anti-Stokes intensity measurements to temperature using the double-ended calibration procedure of Chapter 2 with the modifications suggested in Section 5.5 and Appendices E and F. The acquisition time was set to 30 seconds for the forward and backward directions. Prior to the calibration, a preliminary calibration was performed with a subset of the measurements to estimate parameters that are considered constant over the measurement period. Here, 500 measurements evenly spread throughout the measurement period were used to estimate $\gamma$ and $\Delta\alpha$. The other parameters are transient and estimated for every time step. This approach allows for calibration in chunks, e.g., per 1000 time steps.

### 5.4.3 Groundwater model

During the pumping test, water is extracted from the pumping well and injected in the four injection wells. The aquifer from which is pumped is located between 15.35 and 26.60 m below surface level. A groundwater model is constructed of the specific discharge in the aquifer at the study site to provide an estimate of the specific discharge at the locations where the heat tracer tests are performed. The aquifer is modeled as homogeneous and infinite with a hydraulic conductivity of 10 m/day. It is semi-confined between two clay layers with an average resistance of 500 days. The 5 wells are modeled as fully penetrating and are pumped at steady rates that are listed in Table 5.2. The heads in the aquifer are modeled with the Hantush function, and the specific discharge is computed with the hydraulic conductivity times the spatial derivative of the heads in the aquifer.

The specific discharge estimates at the locations where a heat tracer test is performed are shown in Table 5.3. Based on the direct-push measurements, some variation of the aquifer thickness can be expected and thus in the specific discharge. The analysis of the heat tracer tests assume a constant specific discharge during the test. Using a specific storage of 0.002, the time it takes between the start of pumping and when 95% of the steady-state specific discharge is reached in 3.0 days at all locations. The time at which 95% of the steady state is reached scales proportional to the specific storage; since the specific storage is a rough estimate, the uncertainty of this time is large.

The pumping rate was roughly constant for 58 days before the start of the first heat tracer test, so that it was reasonable to approximate the specific discharge as steady during the first test (Figure 5.2). However, the pumping rate before to the second heat tracer test was lowered from 21.50 $m^3/h$ to 18.68 $m^3/h$ one day before the start of the test, which may adversely affect the results. The ratio between the steady-state specific discharges during the two tests is given in the last column of Table 5.3, which is insensitive to changes in aquifer thickness and resistance of the confining clay layers.



## 5.5 DTS calibration subject to artifacts from connectors

In double-ended setups, the fiber is measured from both ends to estimate the differential attenuation and differentiate it from the temperature effects. This type of setup has several advantages over single-ended setups, which are discussed in Section 2.3.2 and Section 2.10.1. However, the calibration procedure for double-ended setups assumes that the differential attenuation is independent of the direction of propagation. Furthermore, the measurements need to be free from artifacts in the measurements in both directions. In this section, modifications to the double-ended calibration procedure are presented for cases where the assumptions are not valid.

### 5.5.1 Time-variant directional attenuation of the forward and backward measurements

Measurements from both ends of the fiber are used to estimate the integrated differential attenuation along the fiber following the steps from Section 2.3.2. Equations 2.15–2.19 implicitly assume that the differential attenuation is independent of the direction of propagation. However, this approximation does not always hold (e.g., Hartog, 2017, p.143). Differential attenuation that is dependent on the direction of propagation results in an undesired shift in estimated

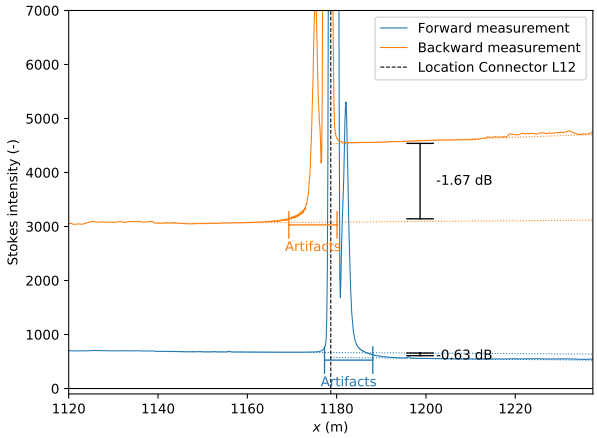


Figure 5.5: Example of directional attenuation and artifacts introduced by Connector L12. The Stokes intensity recorded by the DTS instrument has arbitrary units that are linearly related to the power of the scattered signals.



temperature when not accounted for. Sections of fiber that can introduce directional attenuation include coil-wrapped sections with a small bend radius (Hilgersom et al., 2016), connectors, and poorly spliced fibers. First, it is shown with an example that the attenuation of the Stokes intensity can be directional. Next, it is shown that the differential attenuation can also be directional and can thus affect the temperature estimation. This section ends with modifications to the DTS calibration procedure to account for directional differential attenuation.

The setup contains 8 connectors that can introduce directional attenuation (Figure 5.4). An example of directional attenuation caused by Connector L12 is shown in Figure 5.5 with the Stokes intensity measurements of the forward and backward channels shown in blue and orange, respectively. Note that the backward channel measures in the negative $x$-direction. The step loss (disregarding the peak) over the connector for the forward channel Stokes intensity measurements is a loss of 0.63 dB (14% of the measured intensity is lost), while the step loss over the connector for the backward channel Stokes intensity measurements is a loss of 1.67 dB (32% of the measured intensity is lost). In the case the attenuation is non-directional, the loss would be the same for both measurement channels. The peaks and artifacts in the shadow of the connector are discussed in Section 5.5.2.

The differential attenuation integrated across a connector can be estimated for the forward and backward directions using fiber sections that have the same temperature. The cables that are used in the setup contain multiple fibers. This

setup contains 8 sections where 2 fibers share the same temperature (Figure 5.4), like the one schematized in Figure 5.6. These matching fiber sections share the same cable casing so that they have the same temperature.

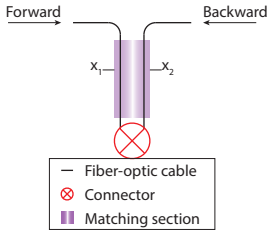


Figure 5.6: Schematization of a section where the temperature of two fibers matches.

Consider locations $x_1$ and $x_2$ along the fiber that have the same temperature (see Figure 5.6). The temperature estimated from forward Stokes and anti-Stokes intensity measurements at $x_1$ and $x_2$ are equal and can be combined with Equation 2.13 as:

$$I_{\mathrm{F}}(x_1,t)+\int_0^{x_1}\Delta\alpha_{\mathrm{F}}(x',t)\,\mathrm{d}x' = I_{\mathrm{F}}(x_2,t)+\int_0^{x_2}\Delta\alpha_{\mathrm{F}}(x',t)\,\mathrm{d}x' \tag{5.10}$$

which gives

$$\int_{x_1}^{x_2}\Delta\alpha_{\mathrm{F}}(x',t)\,\mathrm{d}x' = I_{\mathrm{F}}(x_1,t)-I_{\mathrm{F}}(x_2,t) \tag{5.11}$$

where $\Delta\alpha_{\mathrm{F}}$ is the differential attenuation of the forward measurements. The same holds for the backward measurements at $x_1$ and $x_2$, using Equation 2.14:

$$I_{\mathrm{B}}(x_1,t)+\int_{x_1}^{L}\Delta\alpha_{\mathrm{B}}(x',t)\,\mathrm{d}x' = I_{\mathrm{B}}(x_2,t)+\int_{x_2}^{L}\Delta\alpha_{\mathrm{B}}(x',t)\,\mathrm{d}x' \tag{5.12}$$

which gives

$$\int_{x_1}^{x_2}\Delta\alpha_{\mathrm{B}}(x',t)\,\mathrm{d}x' = I_{\mathrm{B}}(x_2,t)-I_{\mathrm{B}}(x_1,t) \tag{5.13}$$

where $\Delta\alpha_{\mathrm{B}}$ is the differential attenuation of the backward measurements. The difference between the integrated differential attenuation obtained for the forward channel (Equation 5.11) and backward channel (Equation 5.13) is the result of directional differential attenuation between $x_1$ and $x_2$. Time series of

Equations 5.11 and 5.13 are computed for 144 locations of the section with matching temperature on either side of Connector L12. The time series at each location are rather noisy but show a similar trend. The average values of all 144 locations for Equation 5.11 (blue) and Equation 5.13 (orange) are shown in Figure 5.7. When the integrated differential attenuation across the connector does

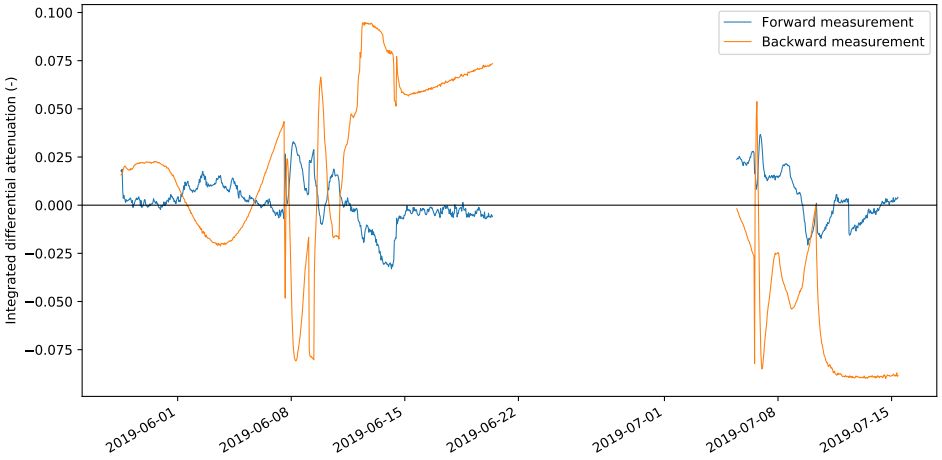


Figure 5.7: Example of directional differential attenuation integrated across Connector L12.

not depend on the direction of propagation, the two lines in Figure 5.7 would be horizontal and the same for the forward and backward direction. To put the magnitude of the variation of the integrated differential attenuation across the connector in perspective, the differential attenuation integrated over the entire length of the fiber (1300 m) without connectors is approximately 0.09.

The directional integrated differential attenuation introduces two additional unknowns per connector per time step that need to be solved for during the calibration. Equations 5.11 and 5.13 introduce enough additional information to solve for the unknown parameters. The required changes to the single-ended and double-ended calibration procedures are discussed in Appendices E and F.

### 5.5.2 Ringing in the shadow of connectors

The loopback connectors in the drive points introduce an additional problem with respect to measuring Stokes and anti-Stokes intensity. The loopback connectors are made of approximately 8 cm of flexible fiber and two LC connectors with an Ultra Physical Contact (UPC) ending. The UPC endings are flat and introduce additional backscatter for measurements in the shadow of the

connector, opposed to Angled Physical Contact (APC) endings that divert the additional backscatter to the sides of the fiber.

The forward channel Stokes intensity measurements that are shown in Figure 5.5, show a large peak at the location of Connector 12 that decays in approximately 8 m (annotated with 'Artifacts'). The backward channel Stokes intensity measurements show a similar behavior. These peaks are caused by the connector and make it impossible to estimate the integrated differential attenuation and the parameter $A$ of the section between 8 m before the connector to 8 m after the connector using the procedure presented in Section 2.6. An alternative approach to estimate the integrated differential attenuation and parameter $A$ are presented in the following.

To estimate the parameter $A$ for the sections around the connector, the parameter $A$ along the entire fiber, defined in Equation 2.15, is approximated to be linear with (Equation 2.11):

$$A(x) = \int_{x_1}^{x} \Delta\alpha(x')\,\mathrm{d}x' \approx \Delta\alpha(x - x_1) \tag{5.14}$$

where $\Delta\alpha$ is approximated with the spatial derivative of $A$ (Equation 2.41)

$$\Delta\alpha \approx \frac{\mathrm{d}A}{\mathrm{d}x} = \frac{\mathrm{d}}{\mathrm{d}x}\left(\frac{I_\mathrm{B}(x,t) - I_\mathrm{F}(x,t)}{2} + \frac{D_\mathrm{B}(t) - D_\mathrm{F}(t)}{2}\right) \tag{5.15}$$

The value of $\Delta\alpha$ is computed with Equation 5.14 using a finite difference scheme and using measurements from all locations that are part of the reference sections ($M$) and of all time steps ($N$)

$$\Delta\alpha \approx \frac{1}{(M-1)\,N} \sum_{m=1}^{M-1} \sum_{n=1}^{N} \frac{1}{\Delta x}\left(\frac{I_{\mathrm{B},m+1,n} - I_{\mathrm{F},m+1,n}}{2} - \frac{I_{\mathrm{B},m,n} - I_{\mathrm{F},m,n}}{2}\right) \tag{5.16}$$

where $\Delta x$ is the distance between measurement locations, which is constant in the case study. Parameters $A$ are approximated with Equation 5.14 used as fixed values along the entire fiber and are excluded from the calibration procedure. It is emphasized that the directional differential attenuation integrated across a connector is accounted for using the calibration procedure adjustments suggested in Section 5.5 and Appendices E and F.

### 5.5.3 DTS calibration results

The presented modifications to the DTS calibration were useful to a limited extent. Part of the double-ended calibration routine is to average the temperature

Table 5.4: Overview of results of improved DTS calibration and usefulness for estimation of specific discharge

| Name | Usefulness | Fluctuation | Comments |
|---|---|---|---|
| L12 | Useful | Daily fluctuation < 0.1 °C | - |
| L13 | Not useful | Similar noise as L14 and daily fluctuation of 0.3 °C | Additional thermal plume during second test. |
| L14 | Not useful | Similar noise as L13 and daily fluctuation of 0.4 °C | Large artifact during the second test. |
| L15 | Not useful | More noise than L12 and daily fluctuation of 0.3 °C | - |
| L16 | Useful | Daily fluctuation < 0.1 °C | - |
| L18 | Not useful | More noise than L14 and daily fluctuation of 0.4 °C | Large artifact during second test. |
| L19 | Not useful | More noise than L16 and daily fluctuation of 0.5 °C | Small artifact during first test. |
| L20 | Useful | Daily fluctuation of 0.15 °C | - |



estimates from the forward and backward measurements. Each of the eight locations has four temperature profiles: forward and backward channel measurements of the fiber section from the surface to the connector, and from the connector to the surface. Here, at most locations either the temperature estimated from the forward measurements or the temperature estimated from the backward measurements showed artifacts, therefore the two temperature estimates were not averaged anywhere. The temperature profiles for each of the eight locations in Figure 5.4 were analyzed for their usefulness to estimate the specific discharge from two tests, as summarized in Table 5.4.

Only the temperature measurements from Locations 12, 16, and 20 can be used to estimate the specific discharge. The estimated temperature at the locations at the outer ends of the fiber (12 and 16) do not show artifacts, which confirms the successful calibration of $\gamma$, $D_{\mathrm{F}}$, and $D_{\mathrm{B}}$. Artifacts in the estimated temperature at Locations 13–15, 18, and 19 are likely due to time-variant directional differential attenuation that are not accounted for in the calibration. The raw measurements, estimated temperature at the eight locations, and plots of the estimated temperature are stored at Tombe (2020).

## 5.6 Results

The results of the active heat tracer experiment described in Section 5.4 are presented. Only the measurements at Locations 12, 16, and 20 could be analyzed, as explained in Section 5.5.3. The results are first analyzed to estimate the thermal dispersion term $\beta_x \rho c$ using the known ratio of the two specific discharge

values. Next, the ratio of the specific discharges is considered unknown and is estimated from the active heat tracer experiment.

### 5.6.1 Improved estimation of the specific discharge from two tests

Values for $\beta_x \rho c$ are estimated with the procedure presented in Section 5.2 from heat tracer tests 1 and 2 performed at Locations 12, 16, an 20. The parameters $A$ and $r/B$ are estimated at each depth for each heat tracer test using the curve-fitting procedure presented in Section 4.4. Estimation of $\beta_x \rho c$ using the steps outlined in Section 5.2 requires an estimate of $\kappa \rho c$, which is obtained from Table 4.1, and an estimate of the ratio of the specific discharges $f$ which is obtained from the groundwater model (Table 5.3). The resulting estimated values of $\beta_x \rho c$ are shown on the lower horizontal axis of the left subplots of Figures 5.8, 5.9, and 5.10. Estimates of $\beta_x$ are shown on the upper horizontal axis of the same subplot and are computed with $\rho c = 2.730\,\mathrm{MJm^{-1}{}^{\circ}C^{-1}}$ (Table 4.2), assuming the uncertainty in $\rho c$ can be neglected with respect to the uncertainty in $\beta_x$.



Estimation of $\beta_x \rho c$ requires significant flow such that thermal dispersion cannot be neglected with respect to thermal conduction in at least one of the two heat tracer tests. In addition, an accurate estimate of the parameters $A$ and $r/B$ is required for both heat tracer tests. In the three figures, the estimated values of $\beta_x \rho c$ and their 95% confidence intervals are only shown where the estimated value was larger than its standard uncertainty (orange). At other depths, the distribution of $\beta_x \rho c$ that is listed in Table 4.1 is used (blue). For Location 12, values for $\beta_x \rho c$ could be estimated between 22.5 m and 27 m below surface level. The values show a large variation with depth with a maximum at 25 m below surface level. Location 16 is located closer to the extraction well, with larger flows. The effects of dispersion are expected to be more dominant at Location 16 than at Location 12, as Location 16 has more favorable conditions for the estimation of $\beta_x \rho c$. Values for $\beta_x \rho c$ at Location 16 could be estimated between 19.5 and 27.5 m below surface level with a few gaps. The specific discharge at Location 20 was too small to estimate $\beta_x \rho c$.

The probability density function of $\beta_x \rho c$ (lower axis) and $\beta_x$ (upper axis) are approximated with a log-Normal distribution for Location 12, Location 16, and Locations 12 and 16 together, and shown in Figure 5.11. The fitted distributions and their 95% confidence intervals are listed in Tables 5.5 and 5.6. The mean of the fitted distributions is similar to the distribution of Table 4.1 and the uncertainty is larger.

The two subplots in the center of Figures 5.8, 5.9, and 5.10 show the specific discharge of the first and second heat tracer test, respectively. The specific discharge is estimated from the estimated values for $\beta_x \rho c$ and values for $\rho_w c_w$ and

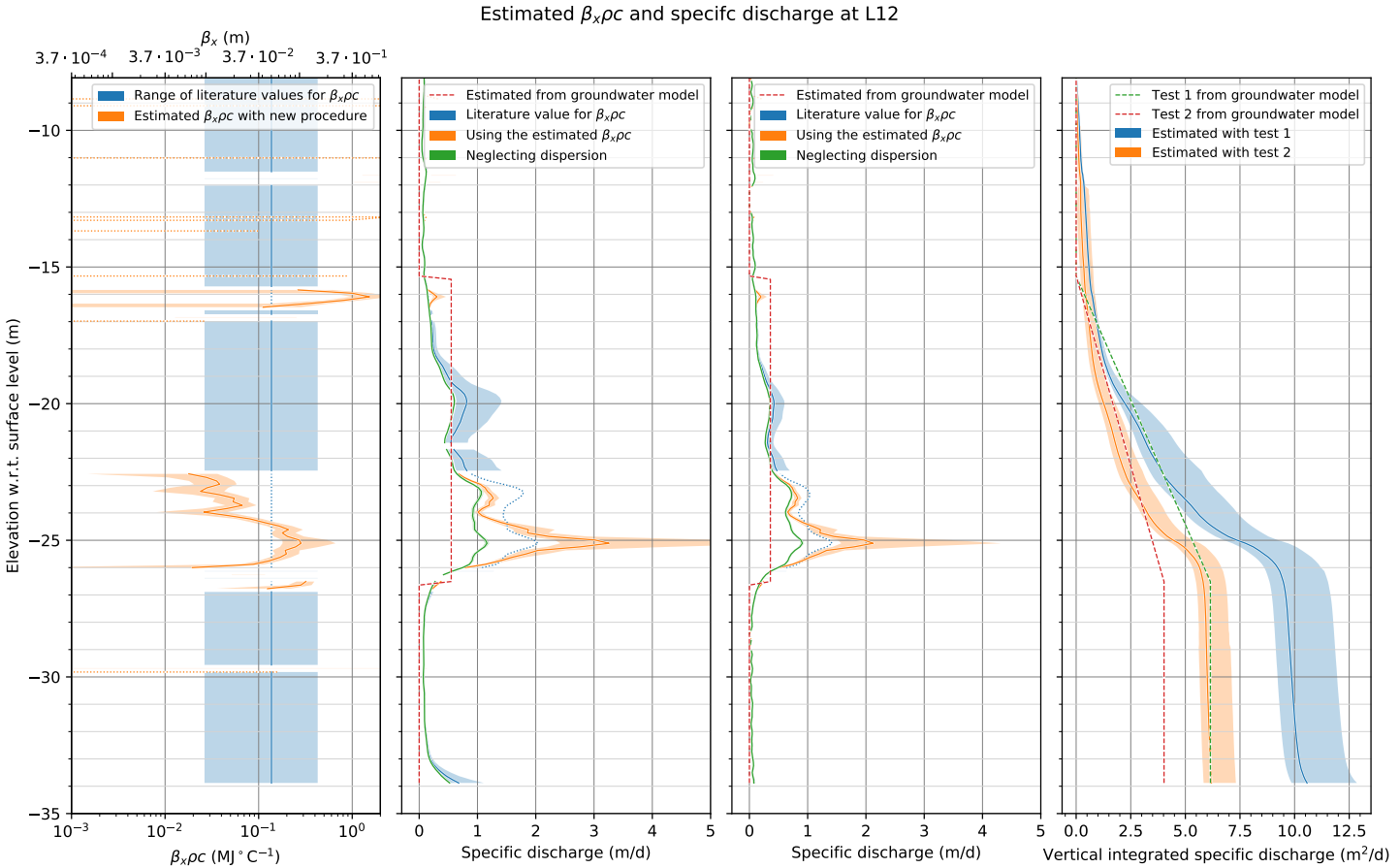


Figure 5.8: Left: Estimated values and 95% confidence interval for $\beta_x\rho c$ at Location 12 and the distribution from Table 4.1 at depths where the estimation was not successful. Center two graphs: Estimated specific discharge at Location 12 for heat tracer test 1 and 2, respectively. Right: Modeled and estimated specific discharge integrated from the surface level downwards Location 12 for heat tracer test 1 and 2.

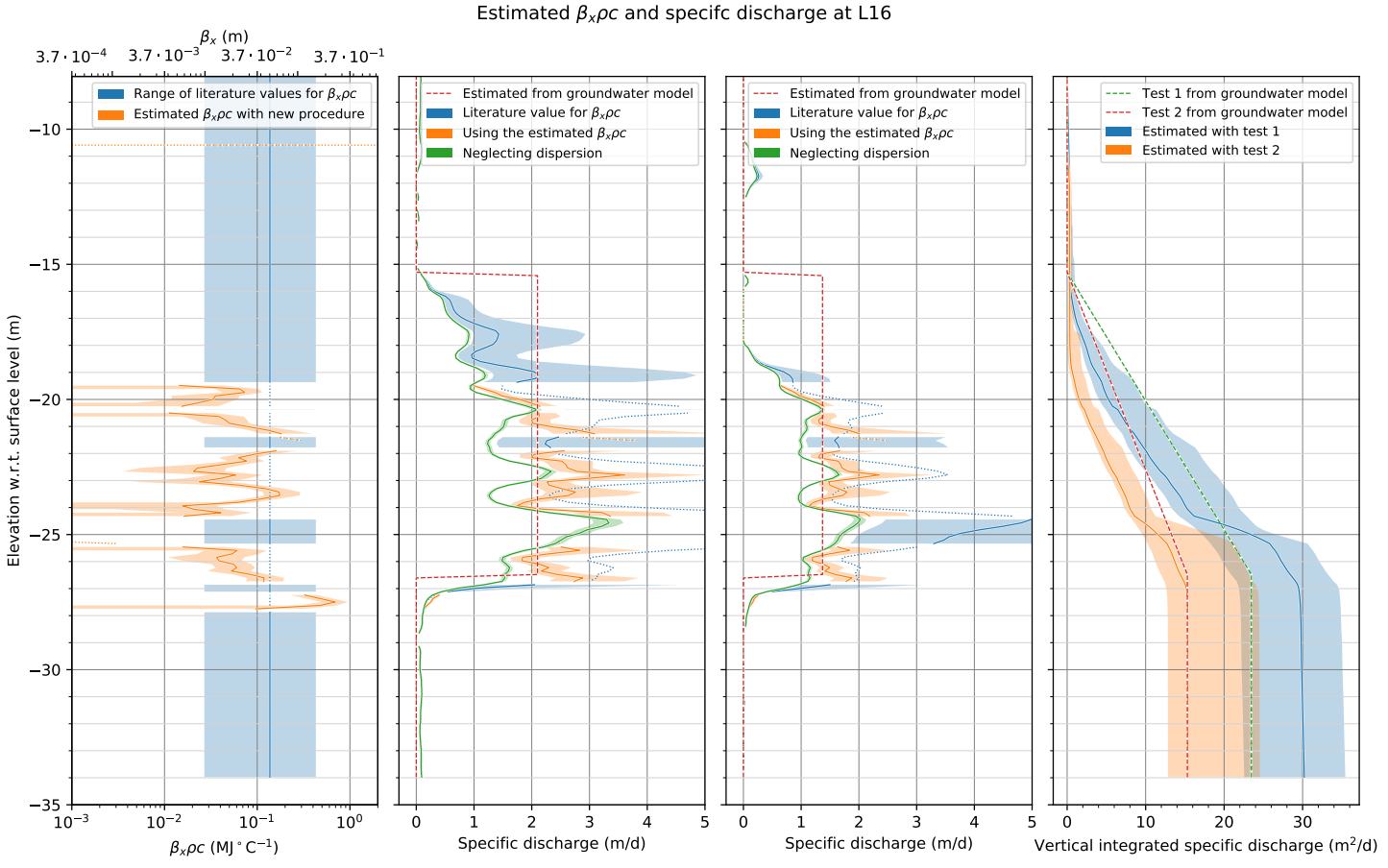


Figure 5.9: Left: Estimated values and 95% confidence interval for $\beta_x\rho c$ at Location 16 and the distribution from Table 4.1 at depths where the estimation was not successful. Center and right: Estimated specific discharge at Location 16 for heat tracer test 1 and 2, respectively. Right: Modeled and estimated specific discharge integrated from the surface level downwards Location 16 for heat tracer test 1 and 2.

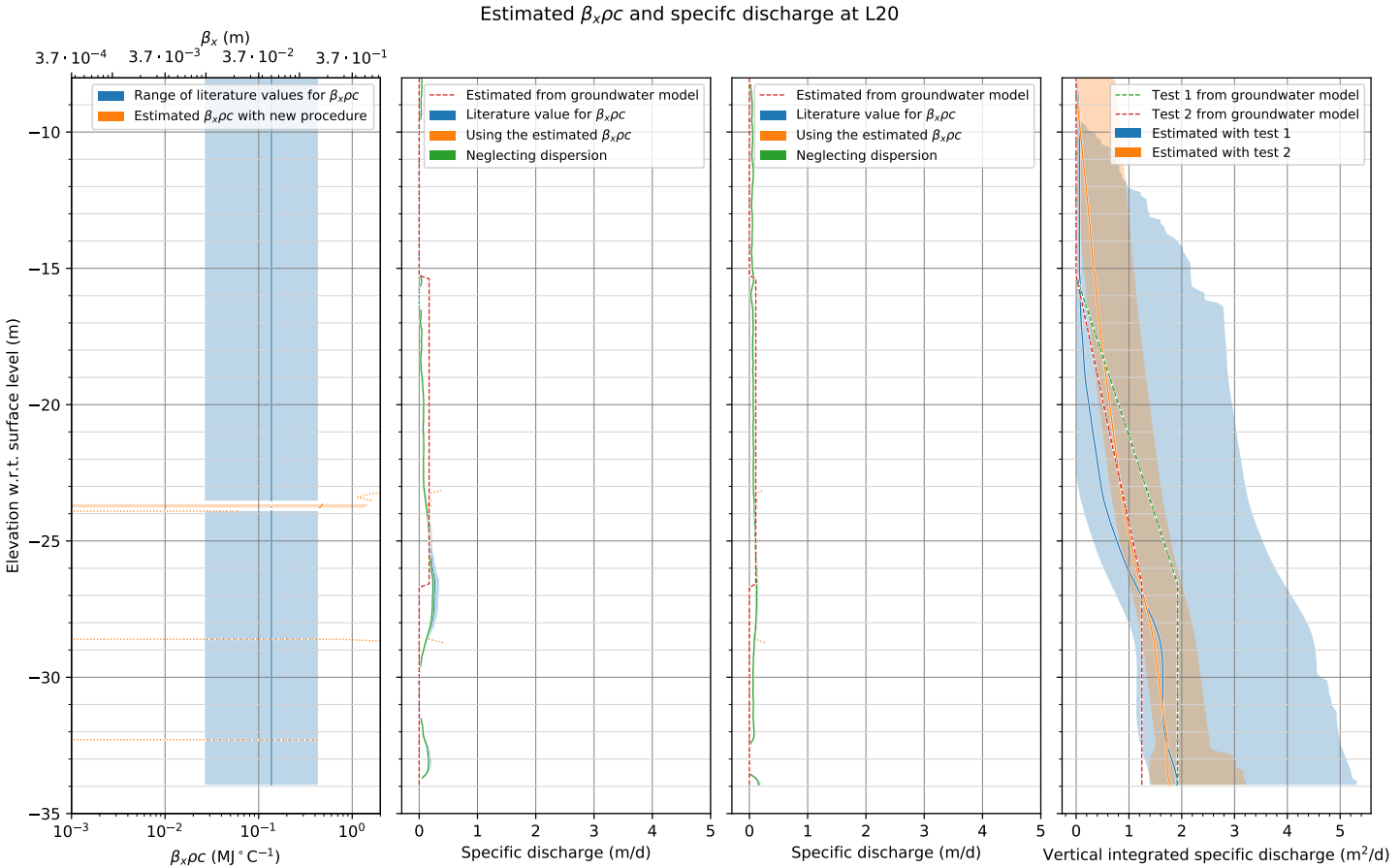


Figure 5.10: Left: Estimated values and 95% confidence interval for $\beta_x \rho c$ at Location 20 and the distribution from Table 4.1 at depths where the estimation was not successful. Center and right: Estimated specific discharge at Location 20 for heat tracer test 1 and 2, respectively. Right: Modeled and estimated specific discharge integrated from the surface level downwards Location 20 for heat tracer test 1 and 2.

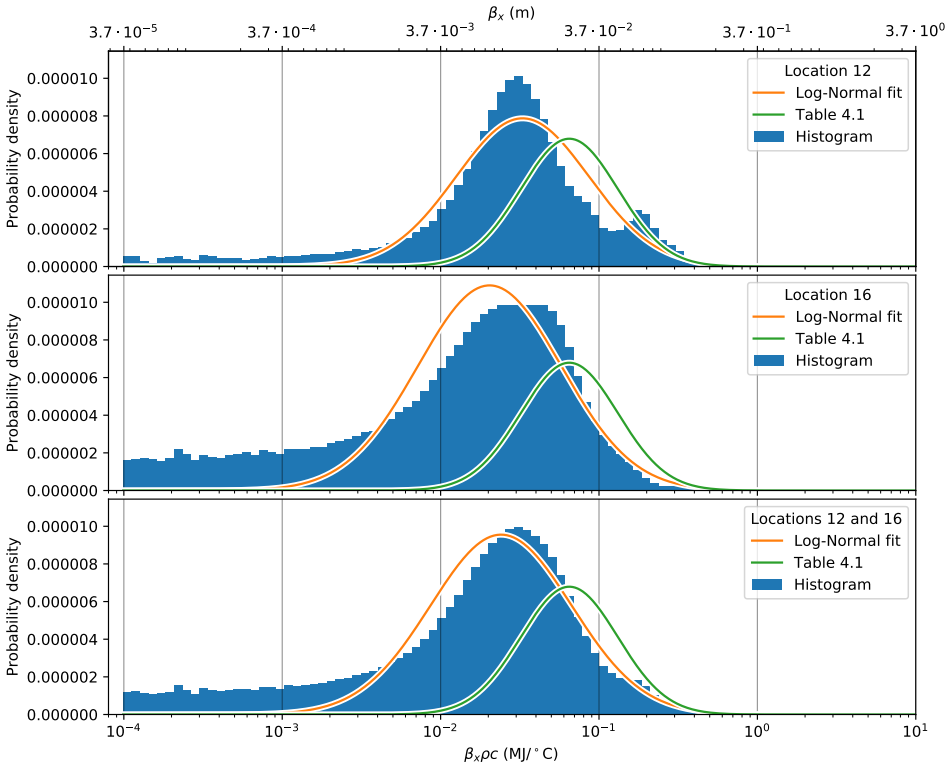


Figure 5.11: Histograms of the estimated $\beta_x \rho c$ and $\beta_x$ at Location 12 (top), 16 (center), and 12+16 (bottom), and the fitted log-Normal probability density distributions. The log-Normal probability density distribution of Table 4.1 is plotted for reference. The units of the probability density distributions of $\beta_x \rho c$ are °C/MJ, and the units of the probability density distributions of $\beta_x$ are 1/m.

Table 5.5: Estimated probability density function of $\beta_x \rho c$ (MJ°C$^{-1}$)

| Location(s) | Probability density function | 2.5% | 97.5% |
|---|---|---|---|
| 12 | LogN($\mu$=0.133, $\sigma$=0.166) | 0.013 | 0.555 |
| 16 | LogN($\mu$=0.104, $\sigma$=0.146) | 0.008 | 0.467 |
| 12 and 16 | LogN($\mu$=0.116, $\sigma$=0.159) | 0.009 | 0.514 |

Table 5.6: Estimated probability density function of $\beta_x$ (m)

| Location(s) | Probability density function | 2.5% | 97.5% |
|---|---|---|---|
| 12 | LogN($\mu$=0.049, $\sigma$=0.061) | 0.005 | 0.203 |
| 16 | LogN($\mu$=0.038, $\sigma$=0.054) | 0.003 | 0.171 |
| 12 and 16 | LogN($\mu$=0.043, $\sigma$=0.058) | 0.003 | 0.188 |

$\kappa\rho c$ from Table 4.1 (orange). At depths where no value for $\beta_x\rho c$ could be estimated, the values from Table 4.1 were used (blue). For comparison, the specific discharge is also estimated without accounting for the effects of thermal dispersion ($\beta_x\rho c = 0$) and is shown in green. The 95% confidence interval of this latter estimate is narrow for all depths, much narrower than the confidence intervals for the estimates that take thermal dispersion into account. These graphs confirm that the uncertainty in $\beta_x\rho c$ is the dominant contributor to the uncertainty of the estimated specific discharge for high flows. For low flows, the influence of the value for $\beta_x\rho c$ on the estimated specific discharge and the associated confidence interval is low (Figure 5.10).

The right subplots of Figures 5.8, 5.9, and 5.10 show the specific discharge that is integrated from 8 m to 34 m below surface level, which is compared to the estimates from the groundwater model. It is emphasized that the horizontal axis of these latter subplots have different limits. The values for $\beta_x\rho c$ obtained from the heat tracer tests were used to compute the vertically integrated specific discharge at depths where they were available. At other depths the literature value of Table 4.1 was used. For depths where $A$ and $r/B$ could not be estimated, the specific discharge was estimated by linearly interpolating between the nearest values. At Locations 16 and 20, the estimates from the groundwater model fall within the 95% confidence interval of the estimates from the heat tracer tests. At Location 12, the estimated vertically integrated specific discharge from the groundwater model is significantly smaller than the estimates from the heat tracer test.



### 5.6.2 Estimation of the ratio of the specific discharge of two tests

The ratio $f$ of the specific discharge of the first test (low flow) over the specific discharge of the second test (high flow) for Locations 12 (left) and 16 (right) is computed using Equation 5.9 and is shown in Figure 5.12. The ratio that is estimated from the groundwater model is show with a black dashed line. The uncertainty distribution is approximated using Monte Carlo sampling by computing $f$ 10.000 times with values of $\kappa\rho c$ and $\beta_x\rho c$ drawn from the uncertainty distribution listed in Table 4.1.

Most of the uncertainty introduced by the uncertainty in the lumped thermal parameters cancels out, which strongly reduces the uncertainty in the estimate of $f$. The value for $f$ is estimated accurately for both locations. The results are close to the value of 0.65 that was expected from the ratio of the pumping rates (Section 5.4.3).

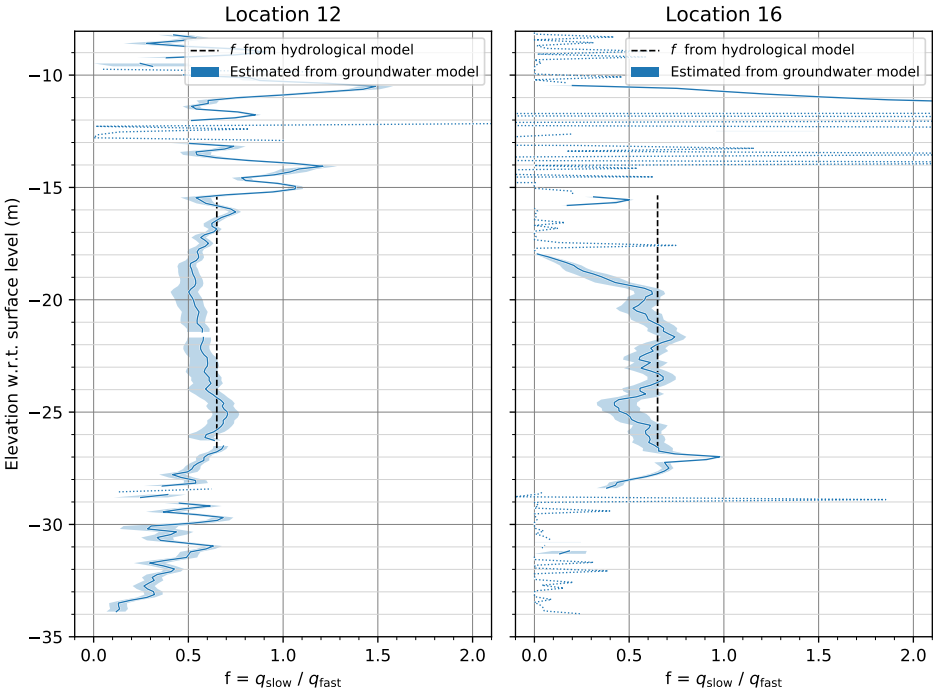


Figure 5.12: Estimation of the ratio of the specific discharge of the second test over the specific discharge of the first test.

## 5.7 Conclusion

For high flows, the uncertainty in the specific discharge estimate is dominated by the uncertainty in $\beta_x \rho c$. Better estimates of $\beta_x \rho c$ improve the estimated specific discharge and increase the applicability of the method by supporting a wider range of flows. In cases such as monitoring the clogging of well filters or estimating the effect of dike reinforcement, the variation of the specific discharge over time may be of more interest than the specific discharge estimates themselves. The ratio of the specific discharge of two heat tracer tests can be accurately estimated for low and high flows with little uncertainty from the estimates of the thermal parameters. A case study is presented in which both approaches are tested. Both methods are demonstrated with heat tracer tests performed during an extensive pumping test.

Fiber-optic cables and heating cables were installed at eight locations near a pumping well, to do eight independent active heat-tracer tests. The pumping test was performed with two different extraction rates, such that the ratio of the specific discharges at each location was known. The changes that were made to the driving point used here compared to the driving points used in Chapters 3 and 4 are not recommended for future applications. The loopback connector was introduced to simplify the construction of the driving point, but it introduced two types of artifacts in the Stokes and anti-Stokes intensity measurements.



First, the loopback connectors introduced differential attenuation that depends on the direction of propagation, which translates to a shift in temperature when not accounted for. The differential attenuation in double-ended setups was previously assumed to be independent of the direction of propagation. In single-ended setups, each section between two connectors had to be calibrated separately. The single-ended and double-ended calibration procedures are modified to account for differential attenuation that is directional. Estimation of the directional differential-attenuation across a connector requires two fiber sections with matching temperatures on either side of the connector, or an additional fiber section that is submerged in a water bath of a known temperature. These modifications are implemented in the Python package dtscalibration.

Second, the loopback connectors introduce a sharp peak in the Stokes and anti-Stokes intensity measurements that decays in approximately 8 m in the shadow of the connector. As a result, it was not possible to estimate the integrated differential attenuation 8 m before and after the connector of this double-ended setups. Instead, the integrated differential attenuation, excluding the effects of the loopback connectors, was approximated to be linear, similar to the

approximation that is made in single-ended setups. However, some artifacts remained, which made five out of eight heat tracer test locations unusable.

Estimation of $\beta_x \rho c$ from two heat tracer tests requires the ratio between the two specific discharges, which is measured during a pumping test or can be obtained from a groundwater model. For the presented case study, an estimate of $\beta_x \rho c$ was obtained at depths where during one of the two heat tracer tests a specific discharge of at least 1 m/day was estimated. At those depths, $\beta_x \rho c$ was estimated with little uncertainty compared to the range of values found by other researchers, which improved the estimate of the specific discharge significantly.

Based on the drilling at the location of the well, not much variability in subsurface layering was expected in the aquifer, but the estimated values for $\beta_x \rho c$ strongly vary with depth. It is therefore not recommended to use the estimates at other depths and locations. The distribution of the estimates of $\beta_x$ and $\beta_x \rho c$ are estimated by combining the estimated values at all depths. The distributions are similar to the distributions that were used in Chapter 4 but have lower mean value and a wider 95% confidence interval.



The lack in knowledge of $\beta_x \rho c$ limits the applicability of heat tracer tests at high flows. More experiments and applications of the method presented here to estimate $\beta_x \rho c$ are needed to obtain a better understanding of its variability, and thereby improve the estimates of the specific discharge for high flows. Further research is envisioned to compare the solute dispersivity with the thermal dispersivity. The solute dispersivity would have to be estimated in situ, given the large variability of the thermal dipersivity. Apart from estimates of the specific discharge, the ratio of the specific discharges can be estimated with relative narrow confidence intervals, even if $\beta_x \rho c$ is unknown.

# 6 Conclusions and Discussion

The installation of optical fibers and heating cables with direct push introduces new possibilities for measuring temperature in unconsolidated aquifers and performing heat tracer tests. The studies in this dissertation contribute to the the measurement of groundwater flow in the first tens of meters of an aquifer with distributed temperature sensing (DTS). This includes: improvements to the cable installation procedure, a new calibration procedure to estimate temperature from DTS measurements, and a new approach to estimate groundwater flow with active heat tracer tests. In addition, insight is obtained in the seasonality of the residence time in bank filtration systems with a passive heat tracer test.



The procedure of installing fiber-optic cables and heating cables with direct-push equipment, introduced by Bakker et al. (2015), was improved for the case studies of Chapters 4 and 5. To simplify the installation procedure, the looped fiber-optic cable was changed to a single cable containing two fibers with their ends connected in the drive point so that thinner push rods could be used to reach greater depth. The fiber ends in the drive point were welded together for the case study of Chapter 4, which was tedious work. In an attempt to simplify the manufacturing of the drive point, loopback connectors were used in the drive points of Chapter 5. The use of loopback connectors is not recommended for future applications because they introduce artifacts in the DTS measurements.

A new calibration procedure was presented to estimate the temperature and its associated uncertainty from DTS measurements. The procedure leads to more accurate temperature and uncertainty estimates compared to existing procedures. Two factors contribute to the predicted uncertainty of the DTS measurement: noise from the detectors that measure Stokes and anti-Stokes scattering, and uncertainty in the calibrated parameters that relate Stokes and anti-

Stokes intensity measurements to temperature. The calibration to reference sections is performed through linear regression where Stokes and anti-Stokes intensity measurements are weighted by their noise, so that the parameter estimation is affected less by noise along reference sections with a low signal strength, i.e., at the end of the fiber. The uncertainty from the noise and the parameter estimation are propagated with Monte Carlo sampling to estimate the uncertainty of the DTS measurement. Measurements with double-ended setups strongly benefit from estimates of the uncertainty. In double-ended setups, the laser is fired from opposite ends of the fiber, resulting in a large difference in uncertainty in the temperature estimated from both ends. The inverse-variance-weighted average of the temperature estimated from both ends of the fiber results in a better temperature estimate than the arithmetic average. The uncertainty of the estimated temperature should be communicated with the temperature estimates for use in heat tracer tests because the uncertainty in the estimated temperature varies in space and time.

In double-ended setups, it was previously assumed that the differential attenuation is independent of the direction of propagation. However, it was shown that (loopback-) connectors along the fiber can introduce differential attenuation that is directional. Changes were made to the DTS calibration routine to support directional differential attenuation for single-ended and double-ended setups. Matching temperature sections introduce the additional constraints that are required to estimate the magnitude of the directional differential attenuation. The DTS calibration procedure is implemented in “dtscalibration”, an open-source Python package that is freely available under the BSD 3-or-later license from `https://github.com/dtscalibration/python-dts-calibration`.

Accurate estimates of the specific discharge ranging from 0.05 to 2.50 meter per day are obtained in a matter of days with active heat tracer tests. The magnitude of the specific discharge can be estimated independent of the position of the fiber-optic cable relative to the heating cable; the direction of flow was not measured. The temperature response at each depth is fitted with three lumped parameters from which the specific discharge is computed with estimates of a conduction term and a dispersion term. For small flows, the effects of thermal dispersion can be neglected and the specific discharge is estimated accurately. For high flows, the uncertainty in the estimated specific discharge is primarily due to the uncertainty in the dispersion term. Heat transfer between the layers is neglected in the presented analysis, which results in vertical profiles of horizontal groundwater flow that are too smooth near jumps in the specific discharge. The specific discharge in layers that are thinner than 1.71 m is not fully captured.

The uncertainty in the estimated specific discharge at high flows can be reduced by combining results from two active heat tracer tests performed at the same location. The measurements from the two tests can be used to obtain an estimate of the dispersion term. The dispersion term can only be estimated if the ratio of the two specific discharges is known independently, e.g., from pumping rates or from a geohydrological model. A case study was performed with active heat tracer tests during two consecutive pumping tests. The dispersion term was accurately estimated at depths where the specific discharge was larger than 1 m/day during at least one of the two tests. The accuracy of the estimated specific discharge greatly improved with these estimates.

In passive heat tracer tests, naturally occurring temperature variations are traced through an aquifer. This type of test can be used to trace seasonal temperature variations through shallow aquifers; variations with a smaller period dampen too fast. Groundwater flow can be estimated from a model for groundwater flow and heat transport coupled via viscosity. Such a model requires boundary conditions for heat transport in addition to boundary conditions for groundwater flow. A passive heat tracer test was conducted at a bank filtration system that is operated to produce drinking water. The travel time distribution is a critical design parameter and was estimated using a model that was calibrated with DTS measurements. The variation of the travel time distribution was primarily the result of the variation of the pumping rate. A second model was built with a constant pumping rate. The changes in viscosity and corresponding hydraulic conductivity caused by the temperature changes resulted in a significant temporal variation of the travel time distribution. In the winter, a larger portion of the water flows through the deeper and less permeable part of the aquifer, when the water in that layer is warmer as compared to the water in the upper part of the aquifer. The reverse happens in the summer, when a larger portion of the water flows through the upper part of the aquifer, and the travel time of the fastest 10% of the extracted water reduces from 49 to 42 days. Therefore, operators need to be aware that the risk of pathogen contamination increases in the summer months, which may warrant lower pumping rates.



Three future research directions are envisioned to improve active heat tracer tests. Vertical conduction and vertical groundwater flow are neglected in the presented analysis and are not accounted for in the uncertainty in the specific discharge estimate. Estimated specific discharge profiles are smoother than in reality because vertical conduction is neglected. Accounting for vertical conduction and vertical groundwater flow may improve the representation of the vertical variation of the specific discharge, and the detection of thin layers with a different flow.

Groundwater flow profiles and their uncertainty can be estimated from active heat tracer tests independent of hydraulic properties and therefore have a great added value for the calibration of geohydrological models. However, active heat tracer tests assume that the background temperature is constant. If this assumption cannot be made, the background temperature can be measured with an additional fiber-optic cable that is inserted with direct-push equipment near the cable pair that is used for the active heat tracer test. The position of the additional fiber-optic cable should be chosen such that the interference from the heating cable is minimal.

The upper limit of the specific discharge that can be estimated from active heat tracer tests is given by the uncertainty in the dispersion term, but the lower limit was not fully investigated. The lower limit is given by the accuracy of the DTS measurements, and the duration of the test. The temperature differences between the thermal responses measured with DTS and the fitted thermal responses of all presented case studies are correlated in time with a daily trend, which affects the parameter estimation. Most likely, these differences are the result of a non-uniform temperature of the water baths that are used for calibration of DTS measurements, which leads to a difference between the temperature of fiber reference sections and the temperature of external sensors. New methods must be developed to remove the correlated errors in the temperature measurements so that a lower specific discharge can be estimated from active heat tracer tests.

# Acknowledgements

I thank Artesia, Wiertsema en partners, PWN, and Waternet for their active participation and investment in the project.

I thank my supervisor Mark Bakker for his countless contributions to the work presented here. He engaged me as a researcher by challenging newly developed solution approaches. His skill set is unique and I feel fortunate to have had Mark as my supervisor. In addition, his work with numerical computing using open-source software is admirable. Furthermore, I thank him for his help in translating rough ideas, which were often clouded by my confusion, to functional solutions fit for publication. I couldn't imagine someone being more capable of doing so.

Frans Schaars was invaluable to the work presented here. His comments increased the relevance of this work. He ensured that the solutions presented here matched the questions of waterboards, drinking-water production companies, and other parties outside of academia. I also thank Kees-Jan van der Made. Translating ideas that were thought off in a safe office environment to solutions that can be employed in the field is not easy. His positive mindset and thinking in solutions have led to the large number of test cases presented here and their success.

It were Marloes van Ginkel and Theo Olsthoorn who first got me interested in the topic of groundwater. The time spent with them felt like a journey, in which I started as a mediocre student who was about to leave university without a bachelor degree and ended with me being a driven and passionate researcher. Marloes, who was working on her PhD at the time under the supervision of Theo, introduced her topic with a presentation during the bachelors to attract new students. I was directly interested and we did two amazing projects together. In the first project, we performed lab experiments with the storage and recovery of fresh water in saline aquifers, and simulated the measurements with numerical modeling. We celebrated the results with a presentation at the Salt Water Intrusion Meeting in Búzios, Brazil. Apart from the science presented at

the conference, the dance lesson with all the attendees and the cocktails were memorable. In the second project, we attempted to come up with solutions to prevent salinization of small rice paddies in the Mekong Delta, Vietnam, from well-organized shrimp farms that were irrigated with salt water. The result was a valuable lesson; the rice farmers were doomed if the government would not interfere. Theo inspired me with his raw enthusiasm and endless curiosity for groundwater modeling. It were his stories of case studies and smart solutions that triggered me to follow a similar path. He introduced me to programming, by the time in MATLAB, and we could spend hours talking about new tools we developed. I will treasure those lessons learned.

There are many from the department whom I would like to thank. First of all, I thank Boran Ekin Aydin and Juan Pablo Aguilar-López for their friendship and after-working-hours distractions. I thank *het loopgroepje* for the great company during the lunch walks. Its composition varied over the years, but included at least: Lydia de Hoog, Erik Mostert, Tamara Auperle, Remco Nijzink, Gaby Gruendemann, Laurène Bouaziz, Miriam Coenders-Gerrits, Edo Abraham, Paul Vermunt, Jerom Aerts, and Chelsea Kaandorp. I greatly appreciate the in-depth discussions with Bart Schilperoort, who shared his talent of clearly explaining difficult topics in fine detail. Willem Jan Zaadnoordijk and I faced many difficulties during the setup of the study site described in Section 5.4. I am glad we solved them together. You were a great partner, and I hope that one day we will collaborate again. Dear Frank Smits, thank you for your advice during the PhD. The most valuable lesson I learned from you was the importance of good relations with everyone involved in the project, including the ones living next to the study site and the ones from the storage facilities. I hope that we will continue to reach out to each other. In addition, I thank my office mates Raoul Collenteur, Teije van der Horst, Paul Vermunt, and Ties van der Heijden, for their lively talks, coffees in the morning, and beers in the evening. And Martin Bloemendal, like the several students we supervised together, I learned a lot from you. It gives me great comfort knowing that you are working on thermal storage to ensure a sustainable future for all of us.

There is no focus during the working hours without the after-hours distractions. Therefore I thank my former roommates: Marij, Nicas, Marianne, Daan, Douwe, Franny, Merel, Redmer, Wout, Freke, Isabel, Sylvain, Suus, Mischa, Sanne, Olav, Storm, Daan, Bob, Tluk, Kano, Rijk, Sjon, and Inge. Thank you all so much for the quality time we have spent together. You all made living in Delft a treat! I thank Anouk, Freek, Emma, Koen and Luuk from my jaarclub Boldt for their friendship, for the regular nights out, and for the amazing holidays. Furthermore, I thank Abel for showing me how to combine hard work with extracurricular joy. Eva, thank you so much for the beautiful thesis cover.

I am looking forward to continue to enjoy your talents in your future works. As I moved back to Amsterdam, I was fortunate and still am, that I have Tom and Wouter in my life. Know that I will always hold you two dear.

I thank my family for their unconditional support. My love and gratitude to Thijs, Sander, Sophie, Josée, Willem, Monica, and Pau. I am incredibly lucky to celebrate this with you.

# References


Abramowitz, M. and I. A. Stegun (1964). *Handbook of Mathematical Functions with Formulas, Graphs, and Mathematical Tables*. New York: Dover Publications. ISBN: 0-486-61272-4.

Anderson, M. P. (2005). "Heat as a Ground Water Tracer." In: *Groundwater* 43.6, pp. 951–968. ISSN: 0017467X. DOI: 10.1111/j.1745-6584.2005.00052.x.

Bakker, M., V. Post, C. D. Langevin, J. D. Hughes, J. T. White, J. J. Starn, and M. N. Fienen (2016). "Scripting MODFLOW Model Development Using Python and FloPy." In: *Groundwater*. ISSN: 17456584. DOI: 10.1111/gwat.12413.

Bakker, M., R. Caljé, F. Schaars, K.-J. van der Made, and S. de Haas (2015). "An active heat tracer experiment to determine groundwater velocities using fiber optic cables installed with direct push equipment." In: *Water Resources Research* 51.4, pp. 2760–2772. ISSN: 00431397. DOI: 10.1002/2014WR016632.

Banks, E. W., M. A. Shanafield, S. Noorduijn, J. McCallum, J. Lewandowski, and O. Batelaan (2018). "Active heat pulse sensing of 3-D-flow fields in streambeds." In: *Hydrology and Earth System Sciences* 22.3, pp. 1917–1929. ISSN: 16077938. DOI: 10.5194/hess-22-1917-2018.

Becker, M. W., B. Bauer, and A. Hutchinson (2013). "Measuring Artificial Recharge with Fiber Optic Distributed Temperature Sensing." In: *Groundwater* 51.5, pp. 670–678. ISSN: 1745-6584. DOI: 10.1111/j.1745-6584.2012.01006.x.

Bense, V. F., T. Read, O. Bour, T. Le Borgne, T. Coleman, S. Krause, A. Chalari, M. Mondanos, F. Ciocca, and J. S. Selker (2016). "Distributed Temperature Sensing as a downhole tool in hydrogeology." In: *Water Resources Research* 52.12, pp. 9259–9273. ISSN: 1944-7973. DOI: 10.1002/2016WR018869.

Bolognini, G. and A. Hartog (2013). "Raman-based fibre sensors: Trends and applications." In: *Optical Fiber Technology* 19.6, Part B. Optical Fiber Sensors, pp. 678–688. ISSN: 1068-5200. DOI: https://doi.org/10.1016/j.yofte.2013.08.003.

Bredehoeft, J. D. and I. S. Papaopulos (1965). "Rates of vertical groundwater movement estimated from the Earth's thermal profile." In: *Water Resources Research* 1.2, pp. 325–328. ISSN: 1944-7973. DOI: 10.1029/WR001i002p00325.

Bruggeman, D. A. G. (1935). “Berechnung verschiedener physikalischer Konstanten von heterogenen Substanzen. I. Dielektrizitätskonstanten und Leitfähigkeiten der Mischkörper aus isotropen Substanzen.” In: *Annalen der Physik* 416.7, pp. 636–664. ISSN: 1521-3889. DOI: 10.1002/andp.19354160705.

Campbell, G. S. (1985). “Chapter 4 Soil Temperature and Heat Flow.” In: *Soil physics with Basic*. Vol. 14. Developments in Soil Science. Elsevier, pp. 26–39. DOI: 10.1016/S0166-2481(08)70134-X.

Cartwright, K. (1970). “Groundwater Discharge in the Illinois Basin as Suggested by Temperature Anomalies.” In: *Water Resources Research* 6.3, pp. 912–918. ISSN: 1944-7973. DOI: 10.1029/WR006i003p00912.

Chiasson, A., S. Rees, and J. Spitler (2000). “A preliminary assessment of the effects of groundwater flow on closed-loop ground source heat pump systems.” In: *ASHRAE Transactions* 106.1, pp. 380–393. ISSN: 00012505.

Coleman, T. I., B. L. Parker, C. H. Maldaner, and M. J. Mondanos (2015). “Groundwater flow characterization in a fractured bedrock aquifer using active DTS tests in sealed boreholes.” In: *Journal of Hydrology* 528, pp. 449–462. ISSN: 0022-1694. DOI: https://doi.org/10.1016/j.jhydrol.2015.06.061.

Constantz, J. (2008). “Heat as a tracer to determine streambed water exchanges.” In: *Water Resources Research* 44.4. ISSN: 1944-7973. DOI: 10.1029/2008WR006996.

Dask Development Team (2016). *Dask: Library for dynamic task scheduling*.

Davey, S., D. Williams, B. Ainslie, W. Rothwell, and B. Wakefield (1989). “Optical gain spectrum of GeO2-SiO2 Raman fibre amplifiers.” In: *IEE Proceedings J (Optoelectronics)* 136.6, pp. 301–306.

Diao, N., Q. Li, and Z. Fang (2004). “Heat transfer in ground heat exchangers with groundwater advection.” In: *International Journal of Thermal Sciences* 43.12, pp. 1203–1211. ISSN: 1290-0729. DOI: https://doi.org/10.1016/j.ijthermalsci.2004.04.009.

Doherty, J. (2016). *PEST, Model-Independent Parameter Estimation – User Manual*. Sixth. Watermark Numerical Computing. Brisbane, Australia.

Domenico, P. and V. Palciauskas (1973). “Theoretical analysis of forced convective heat transfer in regional ground-water flow.” In: *Geological Society of America Bulletin* 84.12, pp. 3803–3814. ISSN: 0016-7606.

Dreuzy, J.-R. de and T. Ginn (2016). “Residence times in subsurface hydrological systems, introduction to the Special Issue.” In: *Journal of Hydrology* 543, Part A, pp. 1–6. ISSN: 0022-1694. DOI: http://dx.doi.org/10.1016/j.jhydrol.2016.11.046.

Drost, W., D. Klotz, A. Koch, H. Moser, F. Neumaier, and W. Rauert (1968). “Point dilution methods of investigating ground water flow by means of radioisotopes.” In: *Water Resources Research* 4.1, pp. 125–146. ISSN: 1944-7973. DOI: 10.1029/WR004i001p00125.

Drury, M., A. Jessop, and T. Lewis (1984). "The detection of groundwater flow by precise temperature measurements in boreholes." In: *Geothermics* 13.3, pp. 163–174. ISSN: 0375-6505. DOI: https://doi.org/10.1016/0375-6505(84)90013-0.

Eriksrud, M. and A. Mickelson (1982). "Application of the backscattering technique to the determination of parameter fluctuations in multimode optical fibers." In: *IEEE Journal of Quantum Electronics* 18.10, pp. 1478–1483. ISSN: 0018-9197. DOI: 10.1109/JQE.1982.1071411.

Euser, T., W. M. J. Luxemburg, C. S. Everson, M. G. Mengistu, A. D. Clulow, and W. G. M. Bastiaanssen (2014). "A new method to measure Bowen ratios using high-resolution vertical dry and wet bulb temperature profiles." In: *Hydrology and Earth System Sciences* 18.6, pp. 2021–2032. DOI: 10.5194/hess-18-2021-2014.

Förster, A., F. Andrea, J. Schrötter, D. F. Merriam, and D. D. Blackwell (1997). "Application of optical fiber temperature logging: An example in a sedimentary environment." In: *GEOPHYSICS* 62.4, pp. 1107–1113. DOI: 10.1190/1.1444211.

Fukuzawa, T., H. Shida, K. Oishi, N. Takeuchi, and S. Adachi (2013). "Performance improvements in Raman distributed temperature sensor." In: *Photonic Sensors* 3.4, pp. 314–319. ISSN: 2190-7439. DOI: 10.1007/s13320-013-0128-1.

Genuchten, M. T. van (1980). "A Closed-form Equation for Predicting the Hydraulic Conductivity of Unsaturated Soils1." In: *Soil Science Society of America Journal* 44.5, p. 892. ISSN: 0361-5995. DOI: 10.2136/sssaj1980.03615995004400050002x.

Giesen, N. van de, S. C. Steele-Dunne, J. Jansen, O. Hoes, M. B. Hausner, S. Tyler, and J. Selker (2012). "Double-ended calibration of fiber-optic raman spectra distributed temperature sensing data." In: *Sensors* 12.5, pp. 5471–5485. ISSN: 14248220. DOI: 10.3390/s120505471.

Greswell, R. B., M. S. Riley, P. F. Alves, and J. H. Tellam (2009). "A heat perturbation flow meter for application in soft sediments." In: *Journal of Hydrology* 370.1-4, pp. 73–82. ISSN: 0022-1694. DOI: 10.1016/J.JHYDROL.2009.02.054.

Hantush, M. S. (1956). "Analysis of data from pumping tests in leaky aquifers." In: *Eos, Transactions American Geophysical Union* 37.6, pp. 702–714. ISSN: 2324-9250. DOI: 10.1029/TR037i006p00702.

Hartog, A. H. (2017). *An introduction to distributed optical fibre sensors*. CRC Press. ISBN: 978-1-4822-5957-5.

Hashin, Z. and S. Shtrikman (1962). "A Variational approach to the theory of the effective magnetic permeability of multiphase materials." In: *Journal of Applied Physics* 33.10, pp. 3125–3131. ISSN: 00218979. DOI: 10.1063/1.1728579.

Hausner, M. B., F. Suárez, K. E. Glander, N. v. d. Giesen, J. S. Selker, and S. W. Tyler (2011). "Calibrating Single-Ended Fiber-Optic Raman Spectra Distributed Temperature Sensing Data." In: *Sensors* 11.11, pp. 10859–10879. ISSN: 1424-8220. DOI: 10.3390/s111110859.

Hausner, M. B. and S. Kobs (2016). "Identifying and correcting step losses in single-ended fiber-optic distributed temperature sensing data." In: *Journal of Sensors* 2016. DOI: 10.1155/2016/7073619.

Henninges, J., G. Zimmermann, G. Büttner, J. Schrötter, K. Erbas, and E. Huenges (2005). "Wireline Distributed Temperature Measurements and Permanent Installations Behind Casing." In: *World Geothermal Congress 2005*. Antalya, Turkey, pp. 1–5.

Hilgersom, K., T. van Emmerik, A. Solcerova, W. Berghuijs, J. Selker, and N. van de Giesen (2016). "Practical considerations for enhanced-resolution coil-wrapped distributed temperature sensing." In: *Geoscientific Instrumentation, Methods and Data Systems* 5.1, pp. 151–162. ISSN: 2193-0856. DOI: 10.5194/gi-5-151-2016.

Hoehn, E. and O. A. Cirpka (2006). "Assessing residence times of hyporheic ground water in two alluvial flood plains of the Southern Alps using water temperature and tracers." In: *Hydrology and Earth System Sciences* 10.4, pp. 553–563. DOI: 10.5194/hess-10-553-2006.

Hopmans, J. W., J. Šimunek, and K. L. Bristow (2002). "Indirect estimation of soil thermal properties and water flux using heat pulse probe measurements: Geometry and dispersion effects." In: *Water Resources Research* 38.1, pp. 7.1–7.14. ISSN: 1944-7973. DOI: 10.1029/2000WR000071.

Hoyer, S. and J. Hamman (2017). "xarray: ND labeled Arrays and Datasets in Python." In: *Journal of Open Research Software* 5.1. DOI: 10.5334/jors.148.

Huelshoff, I., J. Greskowiak, and G. Gruetzmacher (2009). "Analysis of the vulnerability of bank filtration systems to climate change by comparing their effectiveness under varying environmental conditions." In: *Combination of MAR and adjusted conventional treatment processes for an Integrated Water Resources Management*. Ed. by Y. M. LeGolvan, J. Burgschweiger, and P. Stuyvzand. TECHNEAU. Chap. 5.2.3.

Hunt, B. (1983). *Mathematical Analysis of Groundwater Resources*. Butterworth-Heinemann, pp. 124–152. ISBN: 978-0-408-01399-4. DOI: https://doi.org/10.1016/B978-0-408-01399-4.50009-3.

Hurtig, E., J. Schrötter, S. Großwig, K. Kühn, B. Harjes, W. Wieferig, and R. Orrell (1993). "Borehole Temperature Measurements Using Distributed Fibre Optic Sensing." In: *Scientific Drilling* 3.6, pp. 283–286.

Johansen, O. (1977). "Thermal Conductivity of Soils." PhD Thesis. University of Trondheim, p. 291. DOI: 10.1063/1.1699752.

Joint Committee for Guides in Metrology (2008a). *JCGM 100: Evaluation of measurement data—Guide for the expression of uncertainty in measurement (GUM)*. JCGM 100:2008. JCGM.

Joint Committee for Guides in Metrology (2008b). *JCGM 101: Evaluation of measurement data—Supplement 1 to the "Guide to the expression of uncertainty in measurement (GUM)"—Propagation of distributions using a Monte Carlo method*. JCGM 101:2008. JCGM.

Kluitenberg, G. J., K. L. Bristow, and B. S. Das (1995). "Error Analysis of Heat Pulse Method for Measuring Soil Heat Capacity, Diffusivity, and Conductivity." In: *Soil Science Society of America* 59.January, pp. 719–726. ISSN: 0361-5995. DOI: 10.2136/sssaj1995.03615995005900030013x.

Knight, J. H., W. Jin, and G. J. Kluitenberg (2007). "Sensitivity of the dual-probe heat-pulse method to spatial variations in heat capacity and water content." In: *Vadose Zone Journal* 6.4, pp. 746–758. ISSN: 1539-1663. DOI: 10.2136/vzj2006.0170.

Krause, S. and T. Blume (2013). "Impact of seasonal variability and monitoring mode on the adequacy of fiber-optic distributed temperature sensing at aquifer-river interfaces." In: *Water Resources Research* 49.5, pp. 2408–2423. DOI: 10.1002/wrcr.20232.

Ku, H. H. et al. (1966). "Notes on the use of propagation of error formulas." In: *Journal of Research of the National Bureau of Standards* 70.4, pp. 263–273.

Langevin, C. D., D. T. Thorne Jr., A. M. Dausman, M. C. Sukop, and W. Guo (2007). "SEAWAT Version 4: A Computer Program for Simulation of Multi-Species Solute and Heat Transport." In: *U.S. Geological Survey Techniques and Methods Book 6*. U.S. Geological Survey. Chap. A22, p. 39. ISBN: Techniques and Methods Book 6, Chapter A22.

Leaf, A. T., D. J. Hart, and J. M. Bahr (2012). "Active Thermal Tracer Tests for Improved Hydrostratigraphic Characterization." In: *Ground Water* 50.5, pp. 726–735. ISSN: 1745-6584. DOI: 10.1111/j.1745-6584.2012.00913.x.

Lowry, C. S., J. F. Walker, R. J. Hunt, and M. P. Anderson (2007). "Identifying spatial variability of groundwater discharge in a wetland stream using a distributed temperature sensor." In: *Water Resources Research* 43.10. DOI: 10.1029/2007WR006145.

Lu, X.-r., Y. Sun, G.-s. Chen, Y. Qin, Y.-f. Bai, X.-j. Li, and X.-j. Mou (2018). "Influences of thermal dispersion on soil water flux estimates using heat pulse technique in saturated soils." In: *CATENA* 167, pp. 228–235. ISSN: 0341-8162. DOI: 10.1016/J.CATENA.2018.04.041.

Ma, R., C. Zheng, J. M. Zachara, and M. Tonkin (2012). "Utility of bromide and heat tracers for aquifer characterization affected by highly transient flow conditions." In: *Water Resources Research* 48.June, pp. 1–18. DOI: 10.1029/2011WR011281.

Maliva, R. G. and T. M. Missimer (2012). "Arid Lands Water Evaluation and Management." In: *Environmental Science and Engineering*. Ed. by R. Allan, U. Förstner, and W. Salomons. Vol. 3. Environmental Science and Engineering. Springer Berlin Heidelberg. Chap. Managed Aq, p. 806. ISBN: 9783642291043. DOI: 10.1007/978-3-540-88258-9.

Marquardt, D. W. (1963). "An Algorithm for Least-Squares Estimation of Nonlinear Parameters." In: *Journal of the Society for Industrial and Applied Mathematics* 11.2, pp. 431–441. DOI: 10.1137/0111030.

Marsily, G. de (1986). *Quantitative hydrogeology: groundwater hydrology for engineers*. Academic Press. ISBN: 9780122089169.

McDaniel, A., J. M. Tinjum, D. J. Hart, and D. Fratta (2018). "Dynamic Calibration for Permanent Distributed Temperature Sensing Networks." In: *IEEE Sensors Journal* 18.6, pp. 2342–2352. ISSN: 1530-437X. DOI: 10.1109/JSEN.2018.2795240.

Molina-Giraldo, N., P. Bayer, and P. Blum (2011a). "Evaluating the influence of thermal dispersion on temperature plumes from geothermal systems using analytical solutions." In: *International Journal of Thermal Sciences* 50.7, pp. 1223–1231. ISSN: 1290-0729. DOI: https://doi.org/10.1016/j.ijthermalsci.2011.02.004.

Molina-Giraldo, N., P. Bayer, P. Blum, and O. A. Cirpka (2011b). "Propagation of seasonal temperature signals into an aquifer upon bank infiltration." In: *Ground Water* 49.4, pp. 491–502. ISSN: 0017467X. DOI: 10.1111/j.1745-6584.2010.00745.x.

Moscoso Lembcke, L. G., D. Roubinet, F. Gidel, J. Irving, P. Pehme, and B. L. Parker (2015). "Analytical analysis of borehole experiments for the estimation of subsurface thermal properties." In: *Advances in Water Resources* 91, pp. 88–103. ISSN: 03091708. DOI: 10.1016/j.advwatres.2016.02.011.

Newville, M., T. Stensitzki, D. B. Allen, and A. Ingargiola (2014). *LMFIT: Non-Linear Least-Square Minimization and Curve-Fitting for Python¶*. DOI: 10.5281/zenodo.11813.

Nield, D. A. and A. Bejan (2006). *Convection in Porous Media*. Springer, p. 654. ISBN: 9780387290966.

Oliver, D. S. (1993). "The influence of nonuniform transmissivity and storativity on drawdown." In: *Water Resources Research* 29.1, pp. 169–178. ISSN: 00431397. DOI: 10.1029/92WR02061.

Pehme, P., B. Parker, J. Cherry, and J. Greenhouse (2010). "Improved Resolution of Ambient Flow through Fractured Rock with Temperature Logs." In: *Ground Water* 48.2, pp. 191–205. ISSN: 1745-6584. DOI: 10.1111/j.1745-6584.2009.00639.x.

Pehme, P. E., J. P. Greenhouse, and B. L. Parker (2007a). "The Active Line Source Temperature Logging Technique and its Application in Fractured Rock Hydrogeology." In: *Journal of Environmental and Engineering Geophysics* 12.4, pp. 307–322. DOI: 10.2113/JEEG12.4.307.

Pehme, P., B. Parker, J. A. Cherry, and J. P. Greenhouse (2007b). "The potential for compromised interpretations when based on open borehole geophysical data in fractured rock." In: *Proc. EPA/NGWA Fractured Rock Conference: State of the Science and Measuring Success in Remediation*. Portland, Maine, pp. 24–26.

Pollock, D. W. (2012). "User Guide for MODPATH Version 6 | A Particle-Tracking Model for MODFLOW." In: *Techniques and Methods*. Vol. 6. U.S. Geological Survey. Chap. A41, p. 58.

Ramshorst, J. G. V. van, M. Coenders-Gerrits, B. Schilperoort, B. J. H. van de Wiel, J. G. Izett, J. S. Selker, C. W. Higgins, H. H. G. Savenije, and N. C. van de Giesen (2019). "Wind speed measurements using distributed fiber optics: a windtunnel study." In: *Atmospheric Measurement Techniques Discussions* 2019, pp. 1–21. DOI: 10.5194/amt-2019-63.

Rau, G. C., M. S. Andersen, and R. I. Acworth (2012). "Experimental investigation of the thermal dispersivity term and its significance in the heat transport equation for flow in sediments." In: *Water Resources Research* 48.3, W03511. W03511. DOI: 10.1029/2011WR011038.

Ray, C., J. Schubert, R. B. Linsky, and G. Melin (2003). "Introduction." In: *Riverbank Filtration: Improving Source-Water Quality*. Ed. by C. Ray, G. Melin, and R. B. Linsky. Dordrecht, NL: Kluwer Academic Publishers, pp. 1–15. ISBN: 978-0-306-48154-3. DOI: 10.1007/0-306-48154-5{_}1.

Read, T., O. Bour, J. S. Selker, V. F. Bense, T. L. Borgne, R. Hochreutener, and N. Lavenant (2014). "Active-distributed temperature sensing to continuously quantify vertical flow in boreholes." In: *Water Resources Research* 50.5, pp. 3706–3713. ISSN: 00431397. DOI: 10.1002/2014WR015273.

Read, T., O. Bour, V. Bense, T. L. Borgne, P. Goderniaux, M. V. Klepikova, R. Hochreutener, N. Lavenant, and V. Boschero (2013). "Characterizing groundwater flow and heat transport in fractured rock using fiber-optic distributed temperature sensing." In: *Geophysical Research Letters* 40.10, pp. 2055–2059. DOI: 10.1002/grl.50397.

Reiter, M. (2001). "Using precision temperature logs to estimate horizontal and vertical groundwater flow components." In: *Water Resources Research* 37.3, pp. 663–674. DOI: 10.1029/2000WR900302.

Remouche, M., F. Georges, and P. Meyrueis (2012). "Flexible Optical Waveguide Bent Loss Attenuation Effects Analysis and Modeling Application to an Intrinsic Optical Fiber Temperature Sensor." In: *Optics and Photonics Journal* 2, pp. 1–7. DOI: 10.4236/opj.2012.21001.

Ren, T., G. Kluitenberg, and R. Horton (2000). "Determining Soil Water Flux and Pore Water Velocity by a Heat Pulse Technique." In: *Soil Science Society of America Journal* 64.2, p. 552. ISSN: 1435-0661. DOI: 10.2136/sssaj2000.642552x.

Ren, T., K. Noborio, and R. Horton (1999). "Measuring Soil Water Content, Electrical Conductivity, and Thermal Properties with a Thermo-Time Domain Reflectometry Probe." In: *Soil Science Society of America Journal* 63.3, p. 450. ISSN: 0361-5995. DOI: 10.2136/sssaj1999.03615995006300030005x.

Richter, P. (1995). "Estimating Errors in Least-Squares Fitting." In: *The Telecommunications and Data Acquisition Progress Report 42-122*, p. 107.

Saar, M. O. (2011). "Review: Geothermal heat as a tracer of large-scale groundwater flow and as a means to determine permeability fields." In: *Hydrogeology Journal* 19.1, pp. 31–52. ISSN: 14312174. DOI: 10.1007/s10040-010-0657-2.

Sayde, C., C. K. Thomas, J. Wagner, and J. Selker (2015). "High-resolution wind speed measurements using actively heated fiber optics." In: *Geophysical Research Letters* 42.22, pp. 10, 064–10, 073. DOI: 10.1002/2015GL066729.

Schijven, J., P. Berger, and I. Miettinen (2003). "Removal of Pathogens, Surrogates, Indicators, and Toxins Using Riverbank Filtration." In: Dordrecht: Springer Netherlands, pp. 73–116. ISBN: 978-0-306-48154-3.

Schilperoort, B., M. Coenders-Gerrits, W. Luxemburg, C. Jiménez Rodríguez, C. Cisneros Vaca, and H. Savenije (2018). "Technical note: Using distributed temperature sensing for Bowen ratio evaporation measurements." In: *Hydrology and Earth System Sciences* 22.1, pp. 819–830. DOI: 10.5194/hess-22-819-2018.

Schilperoort, B., K. Lapo, A. Freundorfer, and B. F. des Tombe (2020). "Untangling fiber optic Distributed Temperature Sensing: Getting the right temperature and getting there smoothly." In: *EGU General Assembly 2020*. Online, 4-8 May 2020. DOI: 10.5194/egusphere-egu2020-7821.

Seabold, S. and J. Perktold (2010). "Statsmodels: Econometric and statistical modeling with python." In: *9th Python in Science Conference*.

Selker, F. and J. S. Selker (2018). "Investigating Water Movement Within and Near Wells Using Active Point Heating and Fiber Optic Distributed Temperature Sensing." In: *Sensors* 18.4, p. 1023.

Selker, J. S., L. Thévenaz, H. Huwald, A. Mallet, W. Luxemburg, N. van de Giesen, M. Stejskal, J. Zeman, M. Westhoff, and M. B. Parlange (2006). "Distributed fiber-optic temperature sensing for hydrologic systems." In: *Water Resources Research* 42.12, W12202. W12202. ISSN: 1944-7973. DOI: 10.1029/2006WR005326.

Simon, N., O. Bour, N. Lavenant, G. Porel, B. Nauleau, B. Pouladi, and L. Longuevergne (2020). "A Comparison of Different Methods to Estimate the Effective Spatial Resolution of FO-DTS Measurements Achieved during Sandbox Experiments." In: *Sensors* 20.2, p. 570. ISSN: 1424-8220. DOI: 10.3390/s20020570.

Smith, L. and D. S. Chapman (1983). "On the thermal effects of groundwater flow: 1. Regional scale systems." In: *Journal of Geophysical Research: Solid Earth* 88.B1, pp. 593–608. ISSN: 2156-2202. DOI: 10.1029/JB088iB01p00593.

Somogyvári, M. and P. Bayer (2017). "Field validation of thermal tracer tomography for reconstruction of aquifer heterogeneity." In: *Water Resources Research* 53.6, pp. 5070–5084. DOI: 10.1002/2017WR020543.

Stallman, R. W. (1965). "Steady one-dimensional fluid flow in a semi-infinite porous medium with sinusoidal surface temperature." In: *Journal of Geophysical Research* 70.12, pp. 2821–2827. ISSN: 2156-2202. DOI: 10.1029/JZ070i012p02821.

Steele-Dunne, S. C., M. M. Rutten, D. M. Krzeminska, M. Hausner, S. W. Tyler, J. Selker, T. A. Bogaard, and N. C. van de Giesen (2010). "Feasibility of soil moisture estimation using passive distributed temperature sensing." In: *Water Resources Research* 46.3. W03534. ISSN: 1944-7973. DOI: 10.1029/2009WR008272.

Suzuki, S. (1960). "Percolation measurements based on heat flow through soil with special reference to paddy fields." In: *Journal of Geophysical Research* 65.9, pp. 2883–2885. ISSN: 2156-2202. DOI: 10.1029/JZ065i009p02883.

Thorne, D., C. D. Langevin, and M. C. Sukop (2006). "Addition of simultaneous heat and solute transport and variable fluid viscosity to SEAWAT." In: *Computers & Geosciences* 32.10, pp. 1758–1768. ISSN: 0098-3004. DOI: http://dx.doi.org/10.1016/j.cageo.2006.04.005.

Tombe, B. F. des (2019). *DTS measurements supporting a DTS calibration paper*. Dataset license: GPL-3.0-or-later. DOI: 10.4121/UUID:71B5C3C2-4105-4F4F-BD1E-D7C56732A665.

Tombe, B. F. des (2020). *Data underlying the research of Distributed temperature measurements and results of active heat tracer test*. Dataset license: Creative Commons Attribution 4.0. DOI: 10.4121/uuid:fd7dda20-37e6-4f96-981d-b1073687cacc.

Tombe, B. F. des, M. Bakker, F. Smits, F. Schaars, and K. J. Van der Made (2018a). "Estimation of specific discharge using Distributed Temperature Sensing (DTS) measurements of the heat pulse response along cables inserted with direct push." In: *AGU Fall Meeting Abstracts*. Vol. 2018. 10-14 December 2018 in Washington D.C.

Tombe, B. F. des, M. Bakker, F. Schaars, and K. J. van der Made (2018b). "Estimating Travel Time in Bank Filtration Systems from a Numerical Model Based on DTS Measurements." In: *Groundwater* 56.2, pp. 288–299. DOI: 10.1111/gwat.12581.

Tombe, B. F. des, M. Bakker, F. Schaars, K. J. van der Made, R. Caljé, and L. Borst (2016). "A passive heat tracer experiment to determine the seasonal variation in residence times in a managed aquifer recharge system with DTS." In: *43rd IAH congress*. 25-29 September 2016 in Montpellier, France.

Tombe, B. F. des, M. Bakker, F. Smits, F. Schaars, and K.-J. van der Made (2019a). "Estimation of the Variation in Specific Discharge Over Large Depth Using Distributed Temperature Sensing (DTS) Measurements of the Heat Pulse Response." In: *Water Resources Research* 55.1, pp. 811–826. DOI: 10.1029/2018WR024171.

Tombe, B. F. des, M. Bakker, F. Smits, F. Schaars, and K. J. van der Made (2018c). "Measurement of the specific discharge up to 50 m depth using heat pulses and DTS." In: *Geophysical Research Abstracts* 20. 8–13 April, 2018 in Vienna, Austria. ISSN: 1607-7962.

Tombe, B. F. des and B. Schilperoort (2020). *Dtscalibration Python package for calibrating distributed temperature sensing measurements*. v1.0.0. DOI: 10.5281/zenodo.3733102.

Tombe, B. F. des, B. Schilperoort, and M. Bakker (2020). "Estimation of Temperature and Associated Uncertainty from Fiber-Optic Raman-Spectrum Distributed Temperature Sensing." In: *Sensors* 20.8, p. 2235. ISSN: 1424-8220. DOI: 10.3390/s20082235.

Tombe, B. F. des, B. Schilperoort, Z. Perkó, M. Bakker, N. van de Giesen, and J. Selker (2019b). "Distributed Temperature Sensing (DTS) calibration with confidence intervals." In: *Geophysical Research Abstracts* 21. 7-12 April, 2019 in Vienna, Austria.

Toze, S., E. Bekele, D. Page, J. Sidhu, and M. Shackleton (2010). "Use of static Quantitative Microbial Risk Assessment to determine pathogen risks in an unconfined carbonate aquifer used for Managed Aquifer Recharge." In: *Water Research* 44.4, pp. 1038–1049. ISSN: 0043-1354. DOI: 10.1016/j.watres.2009.08.028.

Trainer, F. W. (1968). "Temperature profiles in water wells as indicators of bedrock fractures." In: *US Geological Survey professional paper*.

Tuller, M. and D. Or (2005). "Water Retention and Characteristic Curve." In: *Encyclopedia of Soils in the Environment*. Ed. by D. Hillel. Oxford: Elsevier, pp. 278–289. ISBN: 978-0-12-348530-4. DOI: http://dx.doi.org/10.1016/B0-12-348530-4/00376-3.

Tyler, S. W., J. S. Selker, M. B. Hausner, C. E. Hatch, T. Torgersen, C. E. Thodal, and S. G. Schladow (2009). "Environmental temperature sensing using Raman spectra DTS fiber-optic methods." In: *Water Resources Research* 45.4. W00D23. ISSN: 1944-7973. DOI: 10.1029/2008WR007052.

Van Der Kamp, G. and S. Bachu (1987). "Use of Dimensional Analysis in the Study of Thermal Effects of Various Hydrogeological Regimes." In: *Hydrogeological Regimes and Their Subsurface Thermal Effects*. Vol. 47. American Geophysical Union, pp. 23–28. ISBN: 9781118666500. DOI: 10.1029/GM047p0023.

Vandenbohede, A., A. Louwyck, and L. Lebbe (2009). "Conservative Solute Versus Heat Transport in Porous Media During Push-pull Tests." In: *Transport in Porous Media* 76.2, pp. 265–287. ISSN: 1573-1634. DOI: 10.1007/s11242-008-9246-4.

Virtanen, P. et al. (2020). "SciPy 1.0: Fundamental Algorithms for Scientific Computing in Python." In: *Nature Methods* 17, pp. 261–272. DOI: https://doi.org/10.1038/s41592-019-0686-2.

Wagner, V., P. Bayer, G. Bisch, M. Kübert, and P. Blum (2014a). "Hydraulic characterization of aquifers by thermal response testing: Validation by large-scale tank and field experiments." In: *Water Resources Research* 50.1, pp. 71–85. ISSN: 00431397. DOI: 10.1002/2013WR013939.

Wagner, V., P. Blum, M. Kübert, and P. Bayer (2013). "Analytical approach to groundwater-influenced thermal response tests of grouted borehole heat exchangers." In: *Geothermics* 46, pp. 22–31. ISSN: 0375-6505. DOI: 10.1016/J.GEOTHERMICS.2012.10.005.

Wagner, V., T. Li, P. Bayer, C. Leven, P. Dietrich, and P. Blum (2014b). "Thermal tracer testing in a sedimentary aquifer: field experiment (Lauswiesen, Germany) and numerical simulation." In: *Hydrogeology Journal* 22.1, pp. 175–187. ISSN: 1435-0157. DOI: 10.1007/s10040-013-1059-z.

Wang, M. and N. Pan (2008). "Predictions of effective physical properties of complex multiphase materials." In: *Materials Science and Engineering R: Reports* 63.1, pp. 1–30. ISSN: 0927796X. DOI: 10.1016/j.mser.2008.07.001.

Westhoff, M. C., H. H. G. Savenije, W. M. J. Luxemburg, G. S. Stelling, N. C. van de Giesen, J. S. Selker, L. Pfister, and S. Uhlenbrook (2007). "A distributed stream temperature model using high resolution temperature observations." In: *Hydrology and Earth System Sciences* 11.4, pp. 1469–1480. DOI: 10.5194/hess-11-1469-2007.

Wielink, I. van (2016). "Karteren en modelleren van het zoet-brak grondwatersysteem in de Horstermeer." MA thesis. Amsterdam: Vrije Universiteit.

Wilson, J. L. and P. J. Miller (1978). "Two-Dimensional Plume in Uniform Ground-Water Flow." In: *Journal of the Hydraulics Division* 104.4, pp. 503–514.

Zheng, C., M. Bianchi, and S. M. Gorelick (2011). "Lessons Learned from 25 Years of Research at the MADE Site." In: *Ground Water* 49.5, pp. 649–662. DOI: 10.1111/j.1745-6584.2010.00753.x.

Zheng, C. and P. P. Wang (1999). *MT3DMS: a modular three-dimensional multispecies transport model for simulation of advection, dispersion, and chemical reactions of contaminants in groundwater systems; documentation and user's guide*. Tech. rep. Alabama University.

Zubair, S. M. and M. A. Chaudhry (1996). "Temperature solutions due to time-dependent moving-line-heat sources." In: *Heat and Mass Transfer* 31.3, pp. 185–189. ISSN: 1432-1181. DOI: 10.1007/BF02333318.

# A Intensity-Dependent Variance of the Noise in the Intensity Measurements

The sources of noise dominating the noise in Stokes and anti-Stokes intensity measurements are discussed in the introductory paragraph of Section 2.4. For larger setups with more attenuation and DTS systems with a larger avalanche photodiode gain, $\sigma^2_{P_+}$ and $\sigma^2_{P_-}$ may be expressed as a linear function of the intensity,

$$\sigma^2_{P_+} = \beta_+ P_+ + \sigma^2_{P_+,\mathrm{bg}} \tag{A.1}$$

$$\sigma^2_{P_-} = \beta_- P_- + \sigma^2_{P_-,\mathrm{bg}} \tag{A.2}$$



where $\sigma^2_{P,\mathrm{bg}}$ is the variance of the background noise from the electrical circuit, and $\beta_+$ and $\beta_-$ are the coefficients that relate the intensity to the variance of the noise from the avalanche photodiode.

An algorithm is proposed to obtain $\beta_+$, $\beta_-$, $\sigma^2_{P_+,\mathrm{bg}}$, and $\sigma^2_{P_-,\mathrm{bg}}$ from the residuals between the fitted product of $G(t)$ and $H(x)$ and the Stokes and anti-Stokes intensity measurements. The residuals must be known for a wide range of intensities to estimate the unknowns, e.g., with a reference section at the beginning and end of the fiber. First, start with an array with the Stokes intensity measurements and an array with the residuals. The arrays share a temporal and a spatial dimension. Second, sort both arrays by the Stokes intensity measurements. Third, bin both sorted arrays, and compute per bin the mean of the Stokes intensity measurements and the variance of the residuals. Finally, fit Equation A.1 to the two computed values per bin to estimate $\beta_+$ and $\sigma^2_{P_+,\mathrm{bg}}$. And repeat the algorithm for the anti-Stokes intensity measurements.

# B Correlation Stokes and Anti-Stokes Residuals

The variance in the Stokes and anti-Stokes intensity measurements is estimated from measurements of the reference sections used for calibration (Table 2.1) with the procedure presented in Section 2.4. The residuals between the Stokes intensity measurements and the fitted curve are plotted against the residuals between the anti-Stokes intensity measurements and the fitted curve in Figure B.1. The Pearson correlation coefficient between the two is 0.02. The fitted Normal distribution of the Stokes and anti-Stokes residuals are shown on the top and right axes, respectively. These residuals are used as proxy for the noise from the detector.

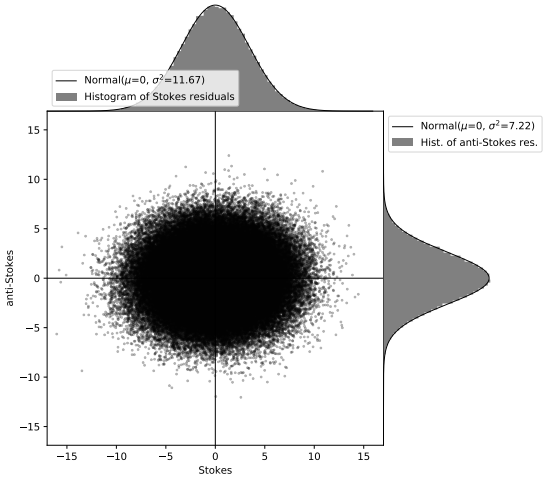


Figure B.1: Stokes residuals plotted against the anti-Stokes residuals. The Stokes and anti-Stokes intensity recorded by the DTS instrument have arbitrary units that are linearly related to the power of the scattered signals.

# C Estimation of advective and conductive heat fluxes

The order of magnitude of the advective heat transport and conductive heat transport are estimated for the 2D-vertical cross-section on a yearly timescale. The advective heat flux $F$ $\left[\mathrm{MLT}^{-3}\right]$ and the conductive heat flux $G$ $\left[\mathrm{MLT}^{-3}\right]$ in the horizontal ($x$) and vertical ($z$) direction are given by,

$$F_x = \rho_w c_w q_x H \frac{\partial T}{\partial x} \quad \text{(C.1)} \qquad G_x = k_b H \frac{\partial T}{\partial x} \quad \text{(C.3)}$$

$$F_z = \rho_w c_w q_z L \frac{\partial T}{\partial z} \quad \text{(C.2)} \qquad G_z = k_b L \frac{\partial T}{\partial z} \quad \text{(C.4)}$$

(C.4)

where $H$ refers to the height of the aquifer [L], $L$ to the distance between the recharge basin and the extraction well [L], and $q$ to the specific discharge $\left[\mathrm{LT}^{-1}\right]$. The temperature gradients are approximated following (e.g., Van Der Kamp and Bachu, 1987; Anderson, 2005),

$$\frac{\partial T}{\partial x} \approx \frac{[\Delta T]_x}{L} \quad \text{(C.5)} \qquad \frac{\partial T}{\partial z} \approx \frac{[\Delta T]_z}{H} \quad \text{(C.6)}$$

(C.6)

where $[\Delta T]_x$ is the temperature difference between the recharge basin and at the extraction well [Θ] and $[\Delta T]_z$ is the temperature difference between the surface and the bottom of the aquifer [Θ].

Representative values for the studied bank filtration system are, $q_x = 0.42\,\mathrm{m\,d^{-1}}$, $q_z = 1\,\mathrm{mm\,d^{-1}}$, $L = 70\,\mathrm{m}$, $k_b = 2.3\,\mathrm{W\,m^{-1}\,°C^{-1}}$, $H = 10\,\mathrm{m}$, $[\Delta T]_x = 4.8\,°\mathrm{C}$, and

$[\Delta T]_z = 10\,°\mathrm{C}$, which results in the following,

$$\begin{aligned} F_x &= 980\,\mathrm{W\,m^{-1}} & G_x &= 1.6\,\mathrm{W\,m^{-1}} \\ F_z &= 34\,\mathrm{W\,m^{-1}} & G_z &= 160\,\mathrm{W\,m^{-1}} \end{aligned} \tag{C.6}$$

The advective heat flux due to areal recharge ($F_z$) is much smaller than the horizontal advective heat flux ($F_x$) and the vertical conductive heat flux ($G_x$). The advective heat flux due to areal recharge can therefore safely be neglected.

# D Alternative formulations of the thermal response

The pulse response of Equation 4.11 is expressed as a function of the steady state temperature ($T_\infty$) of the step response (Equation 4.9). In Section D.1 the pulse response is expressed as a function of the temperature when the heating cable is turned off at $t_0$ ($T(t_0)$). This speeds up the parameter search in the cases that the steady state temperature not is reached before the heating cable is turned off because a good initial estimate of $T(t_0)$ is retrieved directly from the measurements. The formulation without advection presented in Section D.2 speeds up the parameter search for cases where groundwater flow can be neglected.

## D.1 Alternative formulation for little and large flow

This formulation is beneficial for conditions with a smaller specific discharge because it is easier to provide an initial estimate of $T(t_0)$ than of $T_\infty$ (without flow $T_\infty$ goes to infinity). The temperature increase with respect to the background temperature for a heat source that is turned on at $t = 0$ and turned off at $t = t_0$ is obtained from superposition as

$$T(t,t_0) = \begin{cases} \dfrac{T(t_0)}{\mathrm{W}\left(\frac{A}{t_0},\frac{r}{B}\right)}\,\mathrm{W}\left(\dfrac{A}{t},\dfrac{r}{B}\right), & 0 < t \le t_0 \\ \dfrac{T(t_0)}{\mathrm{W}\left(\frac{A}{t_0},\frac{r}{B}\right)}\left[\mathrm{W}\left(\dfrac{A}{t},\dfrac{r}{B}\right) - \mathrm{W}\left(\dfrac{A}{t-t_0},\dfrac{r}{B}\right)\right], & t > t_0 \end{cases} \tag{D.1}$$

with

$$A = \frac{r^2}{4D_x} \tag{D.2}$$

$$\frac{r}{B} = \frac{r\rho_w c_w q}{2\rho c D_x} \tag{D.3}$$

$$\mathrm{W}\left(\frac{A}{t}, \frac{r}{B}\right) = \int_{A/t}^{\infty} \frac{1}{s} \exp\left(-s - \frac{r^2}{4B^2 s}\right) \mathrm{d}s \tag{D.4}$$

where

$$r = \sqrt{x^2 + \frac{D_x}{D_y} y^2} \tag{D.5}$$

$$D_x = \frac{\kappa}{\rho c} + \beta_x q \frac{\rho_w c_w}{\rho c} \tag{D.6}$$

$$D_y = \frac{\kappa}{\rho c} + \beta_y q \frac{\rho_w c_w}{\rho c} \tag{D.7}$$

where $x$ is the horizontal coordinate that aligns with the flow direction and is zero at the heat source, $y$ is the horizontal coordinate perpendicular to the flow direction and is zero at the heat source, W is known in the groundwater literature as the Hantush Well function (Hantush, 1956), $D_x$ and $D_y$ are the thermal dispersion coefficients in the $x$ and $y$ directions, respectively, $q$ is the specific discharge in the $x$-direction, $\rho c$ and $\rho_w c_w$ are the volumetric heat capacity of saturated soil and water, respectively, $\kappa$ is the isotropic bulk thermal conductivity, and $\beta_x$ and $\beta_y$ are the longitudinal and transverse thermal dispersivities, respectively. The specific discharge is estimated from temperature measurements following the steps from Sections 4.3 and 4.4.



## D.2 Formulation for no flow

In the case that the groundwater is stagnant during one of the tests, the thermal response during that test can be formulated with two instead of three parameters, which may be advantageous for the parameter search. When the groundwater is stagnant, the term $r/B$ goes to zero, and the Hantush integral in Equation D.1 reduces to an exponential integral (Abramowitz and Stegun, 1964, Equation 5.1.1).

The solution of the temperature increases with respect to the background temperature for a heat source that is turned on at $t = 0$ and turned off at $t = t_0$ and no flow is given by

$$T(t, t_0) = \begin{cases} \frac{T(t_0)}{\mathrm{E1}\left(\frac{A_1}{t_0}\right)} \mathrm{E1}\left(\frac{A_1}{t}\right), & 0 < t \leq t_0 \\ \frac{T(t_0)}{\mathrm{E1}\left(\frac{A_1}{t_0}\right)} \left[\mathrm{E1}\left(\frac{A_1}{t}\right) - \mathrm{E1}\left(\frac{A_1}{t-t_0}\right)\right], & t > t_0 \end{cases} \tag{D.8}$$

where

$$\mathrm{E1}\left(\frac{A_1}{t}\right) = \int_{A_1/t}^{\infty} \frac{1}{s} \exp(-s)\, \mathrm{d}s, \quad \text{for } \frac{A_1}{t} > 0 \tag{D.9}$$

The function can be numerically evaluated using the `scipy.special.exp1` function in Python (Virtanen et al., 2020).

# E DTS calibration with connectors

Connectors introduce additional integrated differential attenuation, which needs to be accounted for in the calibration procedure to differentiate it from a shift in temperature. It varies over time (Figure 5.7). Extra constraints are needed to estimate its magnitude at every time, such as additional water baths or matching sections (Appendix F). The additional integrated differential attenuation may be different depending on the direction of propagation, complicating the calibration of double-ended setups (Section 5.5.1). The calibration procedure presented in Section 2.3.2 implicitly assumes in Equations 2.15–2.19 that the integrated differential attenuation is nondirectional. The required modifications to the single-ended calibration are discussed in Section E.1 and the required modifications to the double-ended calibration are discussed in Section E.2. The extended calibration procedure is implemented in the Python package dtscalibration version 0.9.0 and up (Section 2.8), and several examples are found in its documentation.

## E.1 Single-ended setups

The temperature given by Equation 2.12 is adapted to account for time-variant differential attenuation

$$T(x,t) = \frac{\gamma}{I(x,t) + C(t) + \Delta\alpha x + \sum_{u=1}^{U} [\Theta(x - x_u) J_u(t)]} \tag{E.1}$$

where $U$ is the number of locations that introduce additional differential attenuation, $J_u$ is the integrated differential attenuation introduced at location $x_u$ and may vary over time, and $\Theta$ is the Heaviside function. The Heaviside function

evaluates to 0 for negative arguments and to 1 for positive arguments. Equation E.1 is reorganized to amend it for linear regression (Section single ended calibration procedure)

$$I_{m,n} = \frac{1}{T_{m,n}}\gamma - C_n - \Delta\alpha x_m - \sum_{u=1}^{U}\left[J_{u,n} \quad \text{if } x_m > x_u\right] \tag{E.2}$$

where the last term in Equation E.5 sums the time-variant integrated differential attenuation ($J_{u,n}$) between the beginning of the fiber and location $m$. The required changes to the least squares procedure introduce the number of time steps times the number of locations that introduce directional integrated differential attenuation, so that the total number of unknown parameters is $N + 2 + NU$.

## E.2 Double-ended setups

The expressions for temperature estimated from forward-channel measurements (Equation 2.16) and backward-channel measurements (Equation 2.17) are given in such case by

$$T_{\mathrm{F}}(x,t) = \frac{\gamma}{I_{\mathrm{F}}(x,t) + D_{\mathrm{F}}(t) + A(x) + \sum_{u=1}^{U}\left[\Theta(x - x_u)J_{\mathrm{F},u}(t)\right]} \tag{E.3}$$

$$T_{\mathrm{B}}(x,t) = \frac{\gamma}{I_{\mathrm{B}}(x,t) + D_{\mathrm{B}}(t) - A(x) + \sum_{u=1}^{U}\left[\Theta(x_u - x)J_{\mathrm{B},u}(t)\right]} \tag{E.4}$$

$J_{\mathrm{F},u}$ and $J_{\mathrm{B},u}$ are the integrated differential attenuation introduced at location $x_u$ in the forward and backward direction. Equations E.3 and E.4 are reorganized to amend them for linear regression as:

$$I_{\mathrm{F},m,n} = \frac{1}{T_{m,n}}\gamma - D_{\mathrm{F},n} - A_m - \sum_{u=1}^{U}\left[J_{\mathrm{F},u,n} \quad \text{if } x_m > x_u\right] \tag{E.5}$$

$$I_{\mathrm{B},m,n} = \frac{1}{T_{m,n}}\gamma - D_{\mathrm{B},n} + A_m - \sum_{u=1}^{U}\left[J_{\mathrm{B},u,n} \quad \text{if } x_m < x_u\right] \tag{E.6}$$

where the last term in Equation E.5 sums the directional integrated differential attenuation in the forward direction ($J_{\mathrm{F},u,n}$) between the beginning of the fiber and location $m$, and the last term in Equation E.6 sums the directional integrated differential attenuation in the backward direction ($J_{\mathrm{B},u,n}$) between location $m$ and the end of the fiber. The required changes to the least squares procedure introduce two times the number of time steps times the number of locations that introduce directional integrated differential attenuation, so that the total number of unknown parameters is $2N + M + 2NU$.

# F DTS calibration with sections with matching temperatures

Consider the schematization shown in Figure 5.6. In the case that two fiber sections have approximately the same temperature, an additional constraint can be formulated that improves the parameter estimation for single-ended setups and double-ended setups. First, the steps for single-ended setups are explained, after which the steps for double-ended setups are explained. The extended calibration procedure is implemented in the Python package dtscalibration version 0.9.0 and up (Section 2.8), and several examples are found in its documentation.

## F.1 Single-ended setups

An additional constraint if formulated by setting the temperature, given by Equation E.1, at location $x_1$ equal to the temperature at $x_2$

$$I(x_1,t) + \Delta\alpha x_1 + \sum_{u=1}^{U} [\Theta(x_1 - x_u) J_u(t)] = I(x_2,t) + \Delta\alpha x_2 + \sum_{u=1}^{U} [\Theta(x_2 - x_u) J_u(t)] \tag{F.1}$$

$$I(x_2,t) - I(x_1,t) = \Delta\alpha\,(x_1 - x_2) + \sum_{u=1}^{U} [(\Theta(x_1 - x_u) - \Theta(x_2 - x_u))\, J_u(t)] \tag{F.2}$$

Note that the last term is a subtraction of the additional integrated differential attenuation introduced by the connectors ($J_u(t)$) summed between $x_1$ and $x_2$.

## F.2 Double-ended setups

Setting the temperature that is given by Equation E.3 and estimated from forward Stokes and anti-Stokes intensity measurements at $x_1$ and $x_2$ equal:

$$I_{\mathrm{F}}(x_1,t)+A(x_1)+\sum_{u=1}^{U}\left[\Theta(x_1-x_u)J_{\mathrm{F},u}(t)\right]=I_{\mathrm{F}}(x_2,t)+A(x_2)+\sum_{u=1}^{U}\left[\Theta(x_2-x_u)J_{\mathrm{F},u}(t)\right] \tag{F.3}$$

$$I_{\mathrm{F}}(x_2,t)-I_{\mathrm{F}}(x_1,t)=A(x_1)-A(x_2)+\sum_{u=1}^{U}\left[\left(\Theta(x_1-x_u)-\Theta(x_2-x_u)\right)J_{\mathrm{F},u}(t)\right] \tag{F.4}$$

Note that the last term is a subtraction of the directional integrated differential attenuation in the forward direction ($J_{\mathrm{F},u}(t)$) summed between $x_1$ and $x_2$. Setting the temperature that is given by Equation E.4 and estimated from backward Stokes and anti-Stokes intensity measurements at $x_1$ and $x_2$ equal:

$$I_{\mathrm{B}}(x_1,t)-A(x_1)+\sum_{u=1}^{U}\left[\Theta(x_u-x_1)J_{\mathrm{B},u}(t)\right]=I_{\mathrm{B}}(x_2,t)-A(x_2)+\sum_{u=1}^{U}\left[\Theta(x_u-x_2)J_{\mathrm{B},u}(t)\right] \tag{F.5}$$

$$I_{\mathrm{B}}(x_2,t)-I_{\mathrm{B}}(x_1,t)=-A(x_1)+A(x_2)+\sum_{u=1}^{U}\left[\left(\Theta(x_u-x_1)-\Theta(x_u-x_2)\right)J_{\mathrm{B},u}(t)\right] \tag{F.6}$$

Note that the last term is a subtraction of the directional integrated differential attenuation in the backward direction ($J_{\mathrm{B},u}(t)$) summed between $x_1$ and $x_2$.

# Curriculum Vitæ

Bas François des Tombe

| | |
|---|---|
| 15-08-1989 | Born in Amsterdam, the Netherlands. |

## Education

| | |
|---|---|
| 2016–2020 | Ph.D. in Civil Engineering, Watermanagement<br>Technical University of Delft, the Netherlands.<br>*Thesis:* Measuring horizontal groundwater flow with distributed temperature sensing along cables installed with direct-push equipment<br>*Promotor:* Prof. dr. M. Bakker |
| 2013–2016 | Master of Science in Civil Engineering, Watermanagement<br>Technical University of Delft, the Netherlands. |
| 2008–2013 | Bachelor of Science in Civil Engineering<br>Technical University of Delft, the Netherlands. |
| 2001–2007 | University preparatory education (VWO)<br>Hervormd Lyceum Zuid, Amsterdam, The Netherlands. |

## Awards

| | |
|---|---|
| 2015 | Best International Student Poster Presentation at the MODFLOW and More 2015 conference, with *The effect of seasonal temperature variations on residence times in a managed aquifer recharge system*. |
| 2013 | Two-year scholarship awarded by Rijkswaterstaat and the Minitry of Infrastructure and Environment within the framework of Topsector Water. |
| 2013 | Cees Boeter Award 2013 for the best bachelor thesis of the Watermanagement department at the TU Delft in 2013, with *Finding a feasible solution to prevent salinization of an irrigation well, Vietnam*. |
| 2012 | Second price at the Dow Sustainability Innovation Student Challenge Award (SISCA 2012), with *Aquifer storage and recovery, the storage thank method*. |

# List of Publications

## Articles

3. B. F. des Tombe, B. Schilperoort, and M. Bakker (2020). "Estimation of Temperature and Associated Uncertainty from Fiber-Optic Raman-Spectrum Distributed Temperature Sensing." In: *Sensors* 20.8, p. 2235. ISSN: 1424-8220. DOI: 10.3390/s20082235.

2. B. F. des Tombe, M. Bakker, F. Smits, F. Schaars, and K.-J. van der Made (2019a). "Estimation of the Variation in Specific Discharge Over Large Depth Using Distributed Temperature Sensing (DTS) Measurements of the Heat Pulse Response." In: *Water Resources Research* 55.1, pp. 811–826. DOI: 10.1029/2018WR024171.

1. B. F. des Tombe, M. Bakker, F. Schaars, and K. J. van der Made (2018b). "Estimating Travel Time in Bank Filtration Systems from a Numerical Model Based on DTS Measurements." In: *Groundwater* 56.2, pp. 288–299. DOI: 10.1111/gwat.12581.

## Presentations

5. B. Schilperoort, K. Lapo, A. Freundorfer, and B. F. des Tombe (2020). "Untangling fiber optic Distributed Temperature Sensing: Getting the right temperature and getting there smoothly." In: *EGU General Assembly 2020*. Online, 4-8 May 2020. DOI: 10.5194/egusphere-egu2020-7821.

4. B. F. des Tombe, B. Schilperoort, Z. Perkó, M. Bakker, N. van de Giesen, and J. Selker (2019b). "Distributed Temperature Sensing (DTS) calibration with confidence intervals." In: *Geophysical Research Abstracts* 21. 7-12 April, 2019 in Vienna, Austria.

3. B. F. des Tombe, M. Bakker, F. Smits, F. Schaars, and K. J. Van der Made (2018a). "Estimation of specific discharge using Distributed Temperature Sensing (DTS) measurements of the heat pulse response along cables inserted with direct push." In: *AGU Fall Meeting Abstracts*. Vol. 2018. 10-14 December 2018 in Washington D.C.

2. B. F. des Tombe, M. Bakker, F. Smits, F. Schaars, and K. J. van der Made (2018c). "Measurement of the specific discharge up to 50 m depth using heat pulses and DTS." in: *Geophysical Research Abstracts* 20. 8–13 April, 2018 in Vienna, Austria. ISSN: 1607-7962.

1. B. F. des Tombe, M. Bakker, F. Schaars, K. J. van der Made, R. Caljé, and L. Borst (2016). "A passive heat tracer experiment to determine the seasonal variation in residence times in a managed aquifer recharge system with DTS." in: *43rd IAH congress*. 25-29 September 2016 in Montpellier, France.

## Software

1. B. F. des Tombe and B. Schilperoort (2020). *Dtscalibration Python package for calibrating distributed temperature sensing measurements*. v1.0.0. DOI: 10.5281/zenodo.3733102

## Datasets

2. B. F. des Tombe (2020). *Data underlying the research of Distributed temperature measurements and results of active heat tracer test*. Dataset license: Creative Commons Attribution 4.0. DOI: 10.4121/uuid:fd7dda20-37e6-4f96-981d-b1073687cacc

1. B. F. des Tombe (2019). *DTS measurements supporting a DTS calibration paper*. Dataset license: GPL-3.0-or-later. DOI: 10.4121/UUID:71B5C3C2-4105-4F4F-BD1E-D7C56732A665